Vibroacoustic Modeling and Control for Launch Vehicle Shrouds

by

Koji Asari

Submitted to the Department of Aeronautics and Astronautics in partial fulfillment of the requirements for the degree of

Master of Science

at the

MASSACHUSETTS INSTITUTE OF TECHNOLOGY

June 1998

Author .....
Aeronautics and Astronautics
May 13, 1998

Certified by .....
Professor David W. Miller
Aeronautics and Astronautics
Thesis Supervisor

Accepted by .....
Jaime Peraire
Associate Professor
Chairman, Department of Graduate Committee

Vibroacoustic Modeling and Control for Launch Vehicle Shrouds

by

Koji Asari

Submitted to the Department of Aeronautics and Astronautics in partial fulfillment of the requirements for the degree of Master of Science at the Massachusetts Institute of Technology

Abstract

Structural-acoustic control with application to launch vehicle shrouds is investigated. Several issues introduce difficulties into the problem which make current acoustic control methods ineffective or impossible to implement. The broadband and diffuse source nature of the acoustic disturbances make a measurement of the incoming disturbance impossible, eliminating the possibility of feedforward methods as a solution. Also, global attenuation of the acoustics is required while the placement of performance microphones near the payload is prohibited because of the possibility of damage to the payload.

The control was implemented in two parts. The first part involved the control of acoustic transmission from the outside environment into the payload fairing enclosure by controlling the vibration of the structure. This was done using a sensitivity weighted Linear Quadratic Gaussian control design targeting the first two structural modes, which are the most efficient in transmitting sound. The second part controlled the reverberation of sound within the enclosure by decreasing the reflection coefficient of one end of the enclosure. This was done using two methods. The first was a sensitivity weighted LQG design in which the first three acoustic cavity modes were targeted. The second was a state space formulation of the acoustic impedance matching control methodology. The transmission and reflection controllers were implemented in succession, allowing for the use of two single input, single output controllers.

Significant reduction in the transmission of sound at the frequencies of the structural modes was achieved using the transmission control. Because the acoustic cavity modes are weakly coupled with the structural modes, control of the structure did not lead to significant damping of the acoustic cavity modes. However, the implementation of the SWLQG reflection control led to appreciable damping on the first three acoustic modes leading to an overall acoustic performance improvement of nearly 6 dB in the broadband metric measured from 10Hz to 1 kHz and modal performance improvements of over 17 dB at the structural modes and up to 12 dB in the first three acoustic modes.

Thesis Supervisor: David W. Miller
Title: Assistant Professor

Acknowledgements

This work was supported by the AFOSR Grant No. F49620-96-1-0290 for the purpose of Active Acoustic Launch Load Alleviation with Capt. Brian Sanders as the AFOSR contract monitor, Charlotte Morse as the MIT contract monitor, Sharon-Leah Brown as the MIT contract administrator, and Karen Buck as the AFOSR contract administrator.

This work would not have been possible without Prof. David Miller whose advice and guidance were invaluable in the course of the research. Previous research by Dr. Roger Glaese provided a foundation upon which this work was based, and his advice was sought on numerous occasions. Dr. Carl Blaurock and Robert Pascal also added significantly to the research effort and are appreciated for their contributions.

Contents

List of Figures

List of Tables

Chapter 1

Introduction

1.1 Motivation

Space bound payloads are subjected to large amplitude vibro-acoustic loads during launch. These loads are the cause of 40% of first day spacecraft failures. Also, launch loads are a major consideration in the structural design of spacecraft. The reduction of acoustic launch loads can lead to the use of more lightweight and off the shelf components, which would lead to lower costs for the spacecraft manufacturer as well as improved performance of the launch vehicle.

There are two major sources of acoustic disturbances during launch. The first is the rocket main engines [1]. During lift off, noise from the rocket main engines reflects off the ground and impinges upon the launch vehicle shroud. The second is due to aerodynamic buffeting during transonic and maximum dynamic pressure flight. The structure of the payload fairing transmits a significant amount of these acoustic disturbances, causing a reverberant acoustic environment inside the payload fairing. In addition, the mechanical vibration of the vehicle is transmitted to the payload fairing, which causes excitation of the enclosed acoustic field.

The problem is worsened by the current trend in the aerospace industry is to use more composite materials in structures, including launch vehicle shrouds. Composite materials are favored because of their high strength and low mass, a good combination for structural design. However, a structure with less mass has less resistance to acoustic disturbances. Low structural mass leads to higher susceptibility to structural acceleration, which is the primary method in which sound is transmitted through the fairing. Since composite fairings designed for the same structural loads as aluminum fairings will have significantly less mass, composite shrouds will transmit sound more readily into the payload fairing enclosure.

1.2 Passive Techniques

The current state of the practice is the use of passive acoustic blankets. Layers of these acoustic blankets are attached to the interior of the launch vehicle shroud [2] and provide a damping mechanism without which acoustic waves would just reflect off the interior walls with little dissipation. The blankets dissipate acoustic waves by transforming the acoustic energy into heat. However, in order for the blankets to be effective, their thickness needs to be a significant fraction of the acoustic wavelength. Therefore, higher frequency acoustic waves are more easily dissipated by the acoustic blankets, while lower frequency acoustic waves pass through the blankets with little dissipation. To complicate matters, the current trend is towards larger rockets with larger payload fairing diameters, and thus lower frequency fundamental acoustic modes. This would require even thicker and heavier layers of acoustic blankets. Currently, the blankets are effective in dissipating acoustic energy at frequencies above 500 Hz.

Another possible passive technique is the replacement of the enclosed air with helium [3,4]. The acoustics is coupled to the vibration of the structure through the density of the

acoustic medium. By using helium which has a lower density than air, the structural-acoustic coupling is reduced. However the use of helium may cause electrical problems with the payload and structural vibrations of the payload may be amplified due to the decreased aerodynamic damping. Evacuation of the enclosed air has also been suggested so as to eliminate all of the acoustics inside the payload fairing, but this would require a large, heavy vacuum pump, which is impractical. Also, the necessary increase in the structural strength of the fairing to prevent collapse will add significant mass to the structure.

1.3 Active Techniques

Active acoustic control is an alternative to the passive techniques discussed in the previous section. These active methods are not intended to replace currently used passive techniques, but to complement them. Since passive acoustic blankets are effective in attenuating higher frequency acoustic disturbances, the active techniques will target lower frequency acoustic disturbances.

There are two main types of active acoustic control. They are Active Noise Control and Active Structural Acoustic Control. Active Noise Control (ANC) [5,6,7,8,9] employs secondary acoustic sources to destructively interfere with the disturbances. Generally, the acoustic disturbances are monitored, and the secondary acoustic sources emit sounds so as to cancel the disturbances at discrete performance points. ANC is most often used when the disturbance has a strong tonal component such as propeller passage frequency or engine RPM and the disturbance source is easily identifiable and compact such as an automobile muffler. However, in the case of the acoustic launch load, the disturbances are broadband and diffuse source, so that a measurement of the disturbance is impossible, making ANC techniques unfeasible. In addition, ANC techniques are usually only successful in achieving attenuation at specific points at which performance microphones have

been placed. In fact ANC techniques may significantly amplify noise at points other than these performance points. This is not satisfactory for the acoustic launch load alleviation problem in which global attenuation is required. Also the need to place performance microphones near the payload should be avoided as this may lead to payload damage.

Active Structural Acoustic Control (ASAC) [10,11,12,13,14,15] on the other hand, uses structural actuators to control the enclosing structure, thus affecting the acoustic field within the enclosure. Since ASAC controls the structural vibrations which lead to the enclosed acoustics, it can control the enclosed acoustic field in a global manner. Although ASAC allows global attenuation of the enclosed acoustics using only structural actuators, it has one problem. This is that it can only control the acoustic modes which are closely coupled with the structural modes.

The impedance matching control technique is a specific type of ASAC. It uses a dereverberated model of the system's local behavior to derive a controller which achieves global acoustic attenuation without the need for performance microphones distributed throughout the enclosure. One main advantage to the impedance matching controller is the lack of need for a complex high order model of the structural-acoustic system. The assumption made for impedance matching control is that the local behavior can be modeled accurately using wave modes and that these are sufficient to obtain an effective controller. Impedance matching control designs generally attempt to eliminate the reflection or transmission of energy through some junction or to maximize the energy dissipated by the controller.

Although impedance matching control has its origins in structural control, it has been applied to structural-acoustic control to a limited degree. In Guicking's work [16], the acoustic reflection coefficient of a single degree of freedom structure in a one-dimensional waveguide was controlled. The sensors were a pair of microphones which were weighted

to give a measure of the incoming acoustic pressure. The feedback gain from the microphone sensors to the single degree of freedom structure was varied manually so that the acoustic reflection coefficient was minimized. Significant reduction in the reflection coefficient was achieved in the frequency range between 100Hz and 800Hz. This was also extended to three dimensional acoustics in which an array of speakers was set up and each speaker was controlled individually using a one dimensional impedance match for reflection. Although reflection coefficients of less than 0.1 were achieved, Guicking's work had one major drawback. Since the control gains were varied manually until a desirable result was obtained, no systematic design methodology was followed to determine the optimal impedance matching compensator.

In Glaese's work [17] a hybrid global/dereverberated model of the structural-acoustic system, in which the structural part of the model is fully reverberant, but the acoustic part is dereverberant, was used. Using an LQG state space formulation, an optimal compensator was obtained which achieved significant attenuation of the first and second acoustic modes. Thus a systematic approach to obtaining an optimal compensator for global acoustic attenuation was provided which used only structural and acoustic sensing at the surface of the enclosing structure.

Much of the past research into active acoustic control is based on feedforward techniques in which a measure of the disturbance is available. Feedforward control using ASAC methods have been used to control acoustic transmission through thin structures into an enclosure, as was done by Balachandran [18]. PZT piezoelectric actuators located on the flexible structure were used with condenser microphone sensors to control the transmission of acoustics generated by a speaker located outside the enclosure. However, the disturbances generated were simply harmonic in nature allowing for the use of a feedforward control.

Since such a measure of the disturbance is not possible in the case of the launch vehicle shroud, feedback methods are required. In Denoyer's work [19], positive position feedback (PPF) using a hybrid structural/acoustic control was done with two actuators and two sensors. The actuators were a piezoceramic actuator and an internal speaker, and the sensors were a piezoelectric strain sensor and a microphone. Significant reductions in the interior acoustics were achieved at frequencies related to both the structural modes as well as the acoustic modes of the enclosure. However, the PPF control design method has a few drawbacks in that it cannot control many modes and it cannot control coupled modes.

There has been much work done in the past in the field of structural-acoustic control. However, much of this research has focused on feedforward control techniques which are not a viable option in the case of the launch vehicle shroud. Therefore feedback control must be used. Much of the past research utilizing feedback methods used either reflection control or transmission control to attenuate the enclosed acoustics. Although Denoyer's work described earlier controls both the transmission of sound into the enclosure as well as the acoustic cavity modes, it doesn't use a systematic control design such as linear optimal control. Therefore the work presented here uses a linear optimal control design to simultaneously control the transmission and reflection of sound to attenuate the acoustic levels within an enclosure.

1.4 Thesis Outline

- Experimental Setup
- Structural-Acoustic Modeling
- Linear Quadratic Gaussian Control Design Techniques
- Control Design Process
- Experimental Results

Chapter 2

Experimental Setup

Since this thesis focuses in experimental implementation of existing modeling and control design methods, the experimental setup for the problem will be discussed first in order to familiarize the reader with the available hardware.

2.1 Approach

The problem of the rocket payload fairing and its enclosed acoustics consists of three dimensional acoustics enclosed by a curvilinear two dimensional structure. In solving a complex problem, it is often insightful to explore a simpler problem while capturing all of the relevant physics. This allows for the validation of methodologies without the difficulties posed by a large order, multi-dimensional problem.

Thus the problem considered consists of one dimensional acoustics in a waveguide with a two dimensional structure whose dynamic properties are well understood. The waveguide is a five foot long closed cylinder, and the structure is a thin, circular aluminum plate which is clamped on all edges. The plate effectively separates the waveguide into an upper chamber and a lower chamber. The plate represents the structure of the launch vehi-

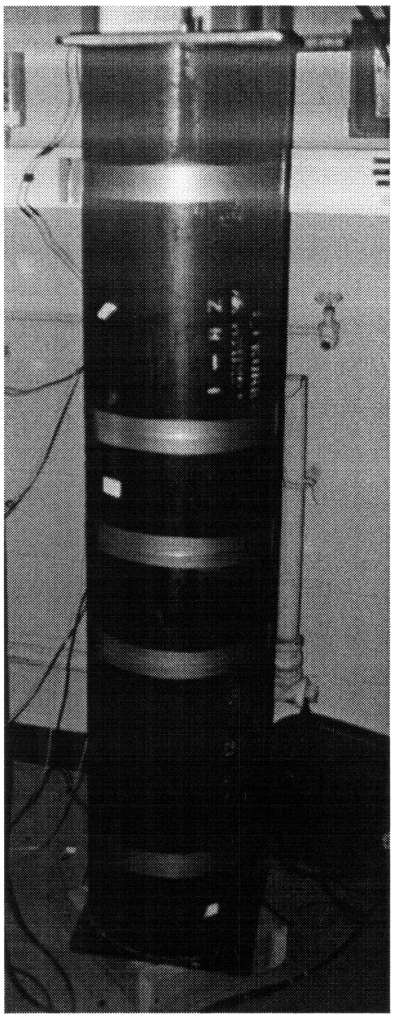

Figure 2.1: Exterior view of structural acoustic test chamber

cle shroud, the lower chamber represents the interior of the payload fairing and the upper chamber represents the outside environment. Using this setup, the problem of attenuating the acoustic environment in the lower chamber is investigated.

2.2 Test Chamber

A photograph of the test chamber is shown in Figure 2.1. The test chamber is a five foot long cylindrical waveguide and is constructed from a 12 inch diameter steel pipe with a three quarter inch wall thickness. The chamber is closed off at the top and bottom with flat

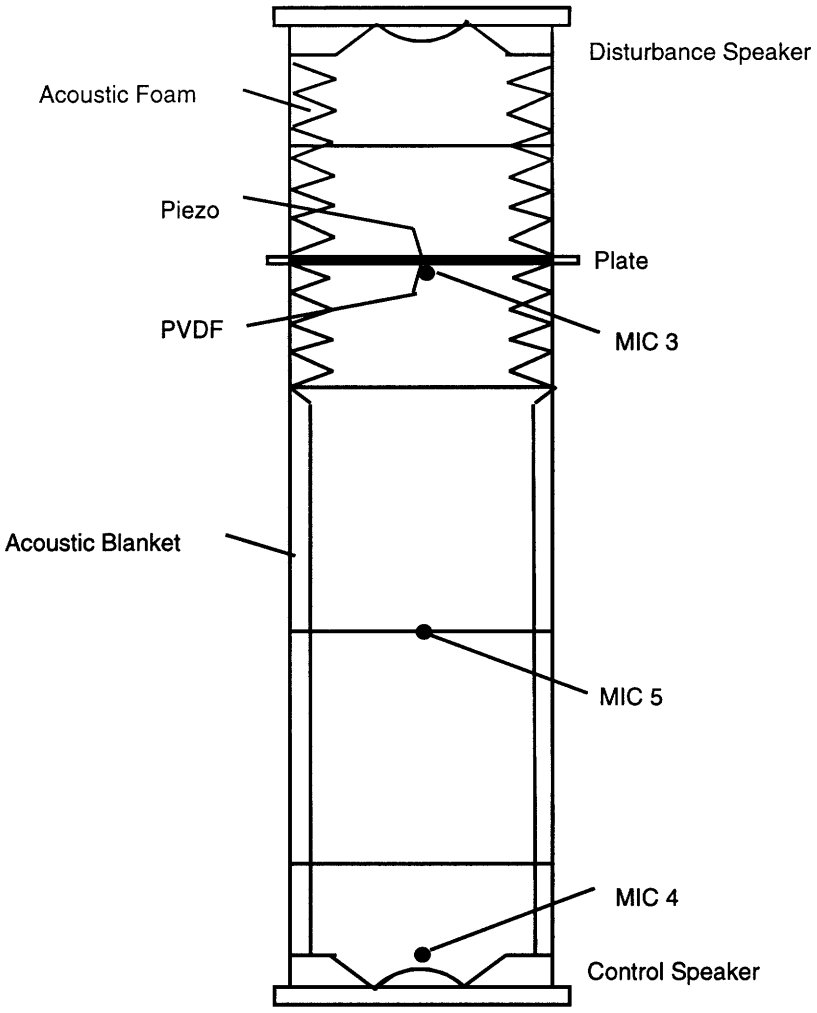

Figure 2.2: Schematic diagram of the structural-acoustic test chamber

half inch thick steel plates. These end caps are attached to the ends of the waveguide with RTV silicone adhesive. The reason for the choice of wall material and thickness is that the high mass and stiffness cause the chamber walls to essentially be acoustically rigid. Creating an acoustically isolated environment is of great importance to prevent stray acoustic disturbances from entering the chamber.

Figure 2.2 shows a schematic diagram of the test chamber. The chamber is segmented into six sections, four sections of length 7.5 inches and two sections of length 15 inches. The chamber is segmented for a variety of reasons. The first is so that the chamber can be

disassembled or relocated by one person. The second is to allow wires for sensors and actuators to exit the chamber as well as to allow the aluminum plate to be placed at various points along the chamber. The third is to allow different length configurations of the test chamber itself by eliminating one or more sections. During the experiments, the joints between the sections are sealed tightly with a ring of hardened RTV silicone as well as electrical tape and duct tape to maintain acoustic isolation of the chamber interior.

There are two ten inch dual voice coil subwoofer speakers with one located at each end of the chamber. They are mounted on the end plate with an aluminum baffle ring which is attached to the chamber wall. There are also five electret condenser microphones located along the length of the chamber, with two in the upper chamber and three in the lower chamber. The two microphones in the upper chamber are used to monitor the disturbance, while the three microphones in the lower chamber are used to determine the performance. All of the microphones are suspended along the centerline of the chamber using a stiff wire and are inserted between the chamber sections. It should be noted that since the acoustic waves of interest have wavelengths which are significantly longer than the size of the microphones or their supports, these structures do not affect the acoustic field in any significant manner.

Lining the walls of the bottom chamber is a fiberglass blanket and a ring of acoustic foam as shown in Figure 2.3. The blanket and foam act as a passive acoustic damper simulating the acoustic blankets which are currently being used in actual payload fairings. Acoustics above approximately 500 Hz are very well damped whereas the lower frequency acoustic modes are not. Figure 2.4 shows transfer functions from the disturbance speaker to the root sum square of the performance microphones (microphones 3, 4, and 5) with and without the fiberglass blanket and foam. The effect of the passive dampers is clear in the acoustic modes above 500 Hz.

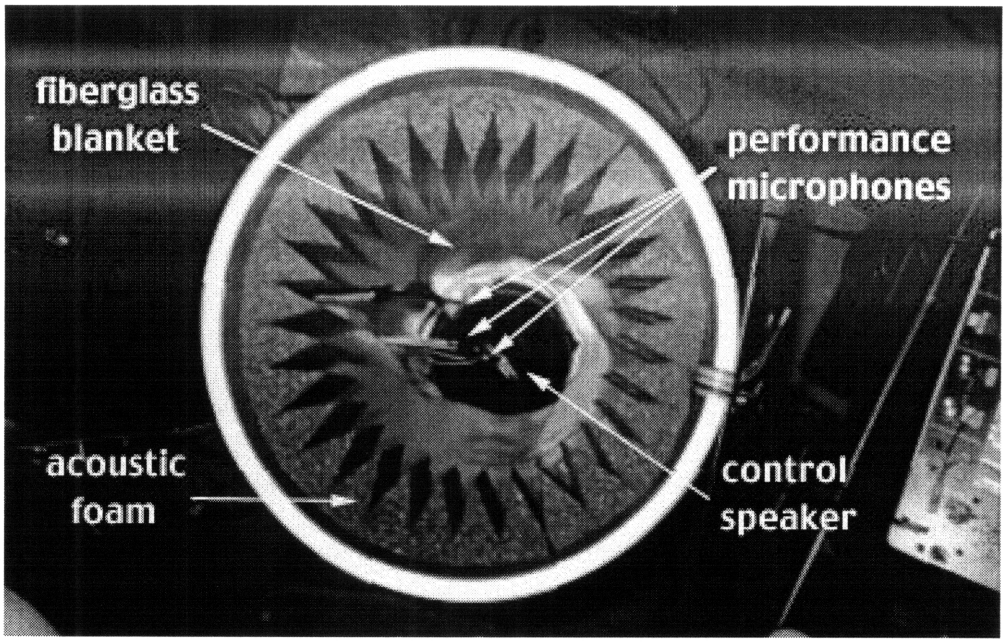

Figure 2.3: Photograph of chamber interior looking down the length of the waveguide, showing the acoustic foam, fiberglass blanket, performance microphones, and control speaker

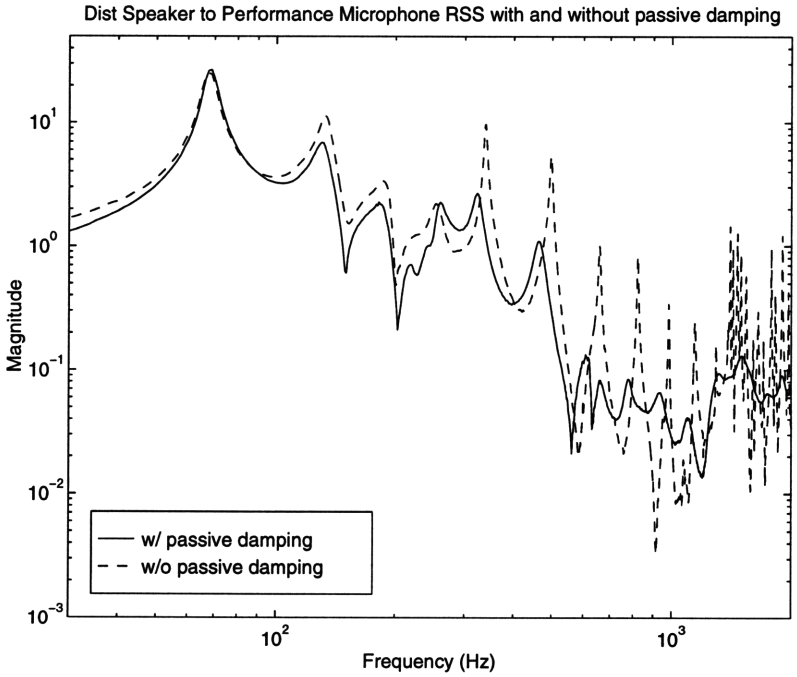

Figure 2.4: Disturbance speaker to performance microphones with and without the fiberglass blanket and acoustic foam linings

The aluminum plate is inserted between the second and third sections down from the top. The plate effectively separates the chamber into two separate enclosures. The plate represents the structure of the launch vehicle shroud. The smaller top enclosure represents the acoustic environment outside of the fairing, while the lower enclosure represents the inside of the payload fairing. The speaker at the top of the chamber is used as the acoustic disturbance source. The acoustic disturbance impinging upon the plate should be a direct field, non-reverberant acoustic field consisting of band limited white noise. Therefore an effort was made to reduce the reverberant acoustics in the top chamber by placing acoustic foam around the inner circumference of the top enclosure. Also the length of the top enclosure is kept short to increase the frequencies of the longitudinal acoustic modes, so that reverberant acoustics of the top chamber have frequencies which are significantly higher than the frequency range on interest.

Two different plates, both constructed of 0.032 inch thick aluminum are instrumented with various sensors and actuators. These plates can be used interchangeably in the chamber to allow for the use of different sensors and actuators. Both plates have a rectangular piezoelectric patch for structural actuation which is bonded to the center of the plate. The first plate, shown in Figure 2.5, has three strain gages and an accelerometer for structural sensing, and a microphone for acoustic sensing. The accelerometer and microphone are mounted at the center of the plate, so that they are collocated with the piezoelectric actuator, which is mounted on the other side of the plate. Also, the microphone is mounted with its face perpendicular to the plate because its diaphragm is sensitive to acceleration. If the microphone were mounted with its face parallel to the plate, then structural acceleration of the plate would cause the diaphragm of the microphone to accelerate as well, causing the microphone to measure structural acceleration in addition to acoustic pressure. By placing the microphone with its face perpendicular to the plate, its sensitivity to acceleration is

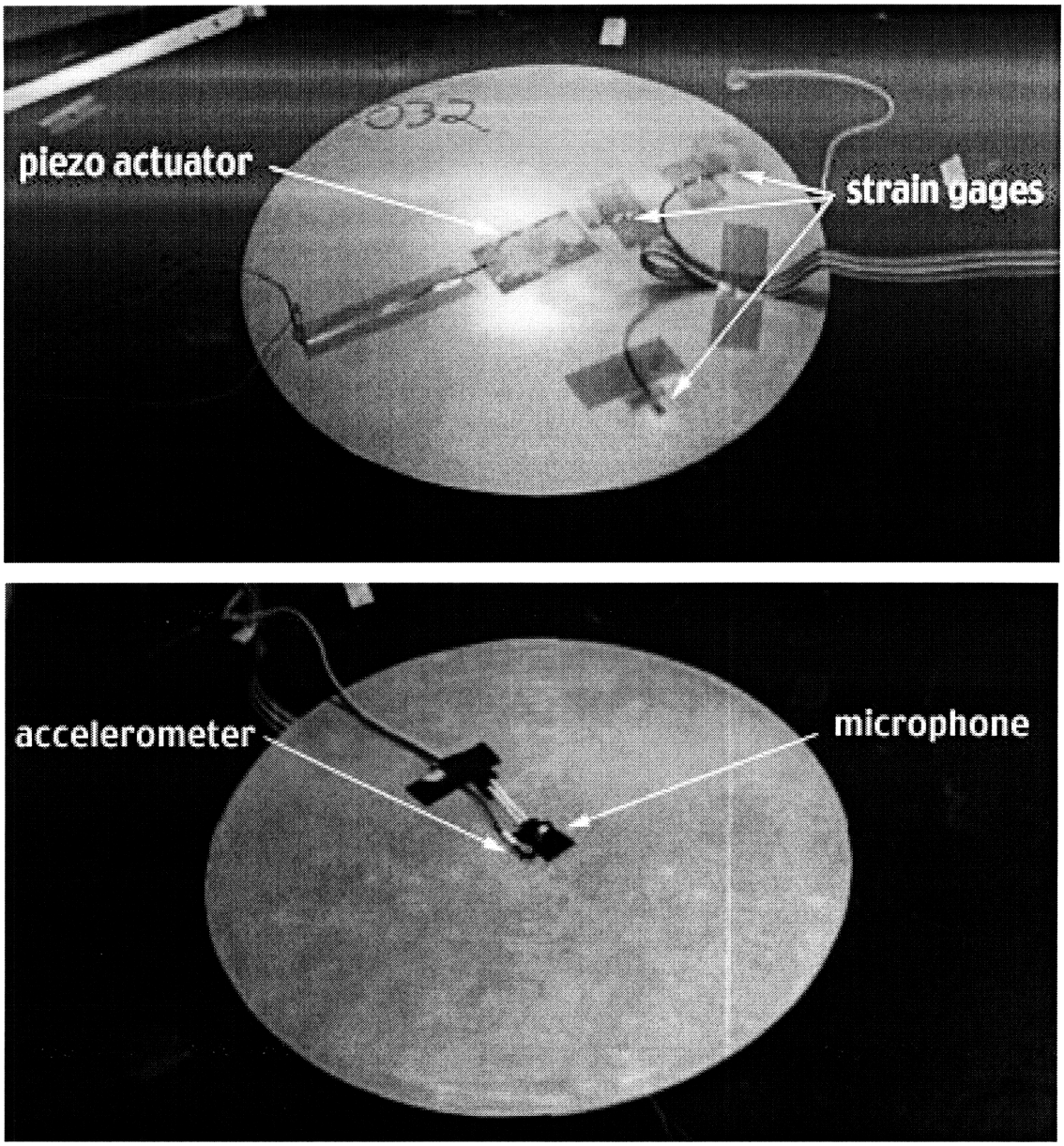

Figure 2.5: Photograph of aluminum plate number 1, instrumented with strain gages and an accelerometer for structural sensing, a microphone for acoustic sensing and a piezoceramic patch for structural actuation

orthogonal to the motion of the plate, causing the acceleration component of the microphone measurement to become negligible.

The second plate, shown in Figure 2.6, has two strain gages and an area averaging piezoelectric strain sensor. The accelerometer and strain gages are located at the center of the plate, so that they are collocated with the piezo actuator. The area averaging strain sen-

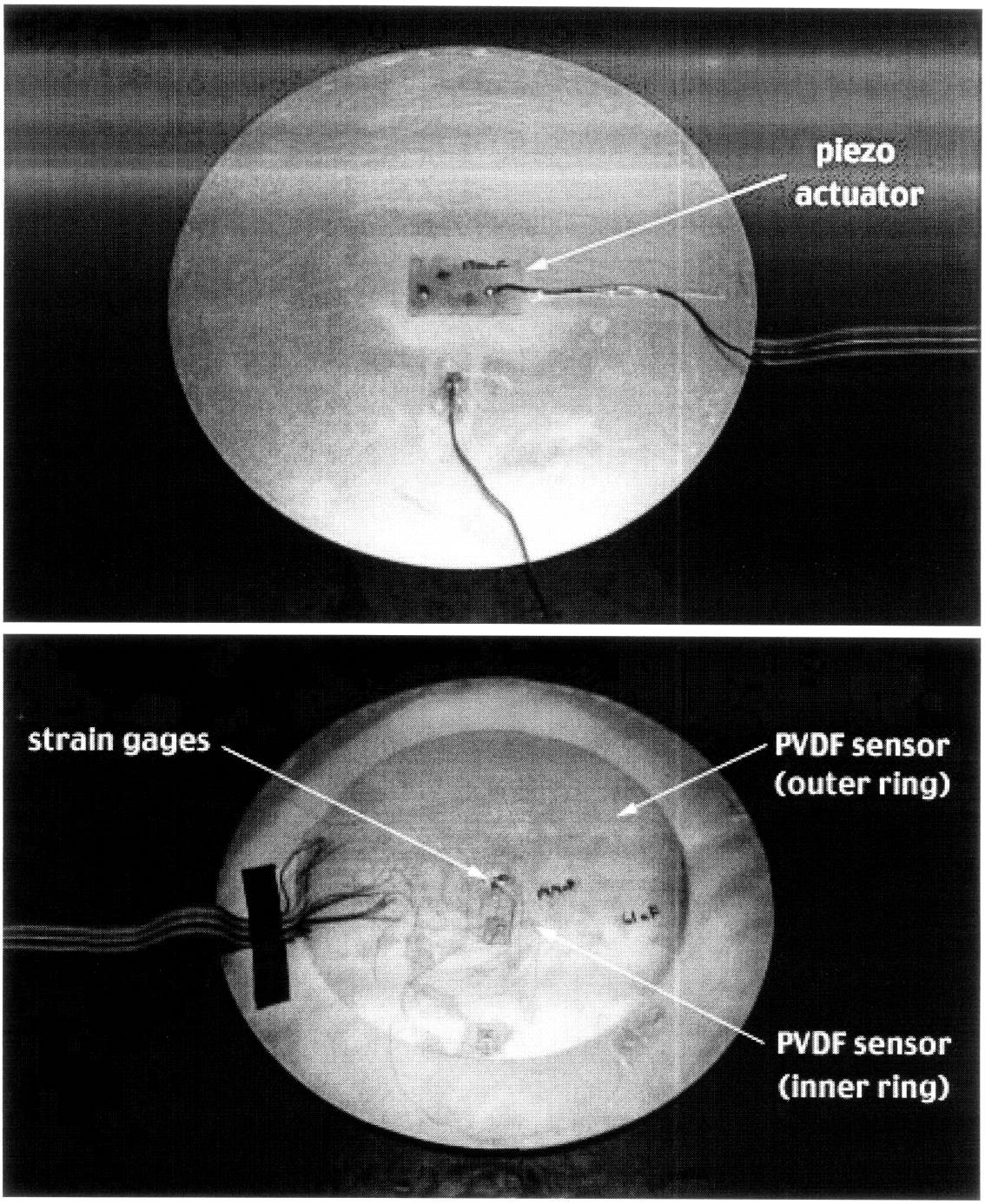

Figure 2.6: Photograph of aluminum plate number 2, instrumented with strain gages and PVDF for structural sensing and a piezoceramic patch for structural actuation

sor is made of polyvinylidene flouride (PVDF) film formed into two concentric annuli and bonded to the plate using epoxy. The methodology used for the design of the PVDF sensor will be discussed in chapter 5.

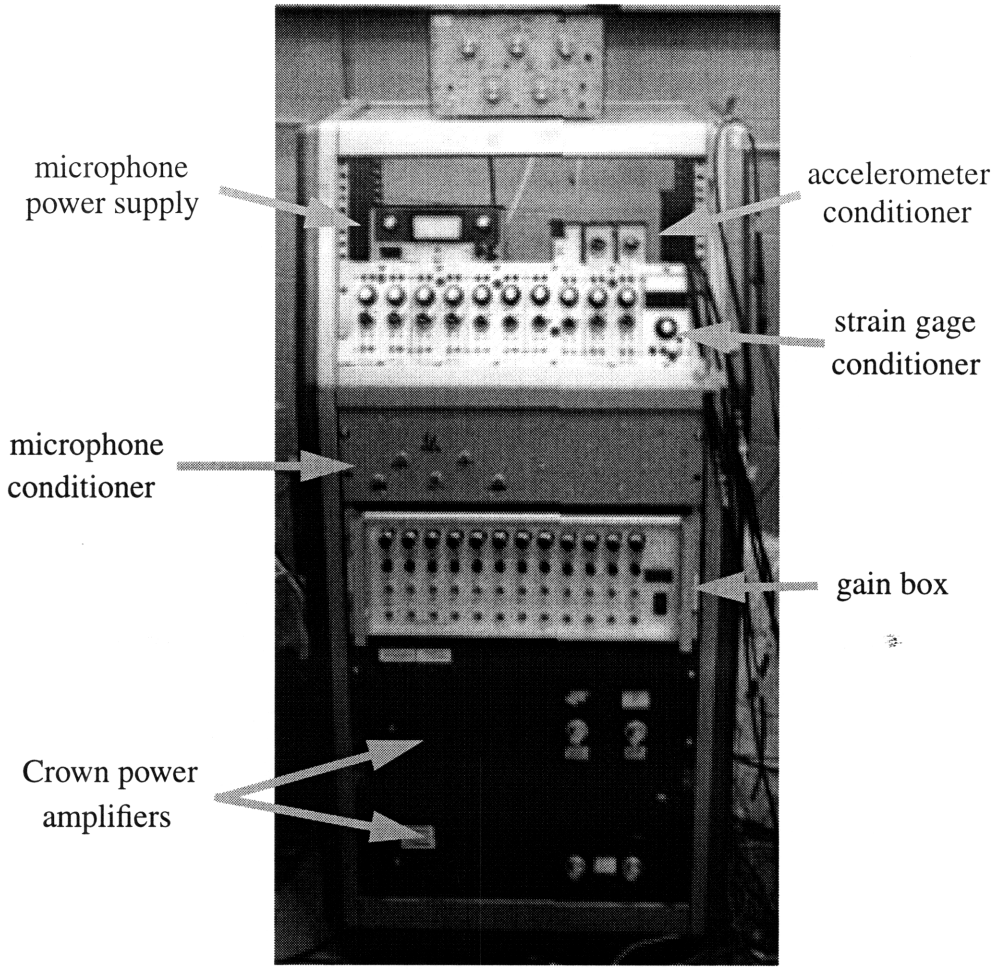

Figure 2.7: Photograph of electronics rack for signal conditioning and amplification

2.3 Electronics

Since the actuators are driven by electronic signals and the sensors provide electronic signals, power supplies and signal conditioning amplifiers are required. Figure 2.7 shows a photograph of the main electronics rack. The piezoceramic patch, disturbance speaker, and control speaker are driven using three channels of a Crown DC-300A Series II power amplifier, shown at the bottom. An ENDEVCO charge amplifier (top right) is used as the signal conditioner for the accelerometer, and a 3-10 VDC power supply (top left) is used as a power source for the electret condenser microphones. Just below the accelerometer

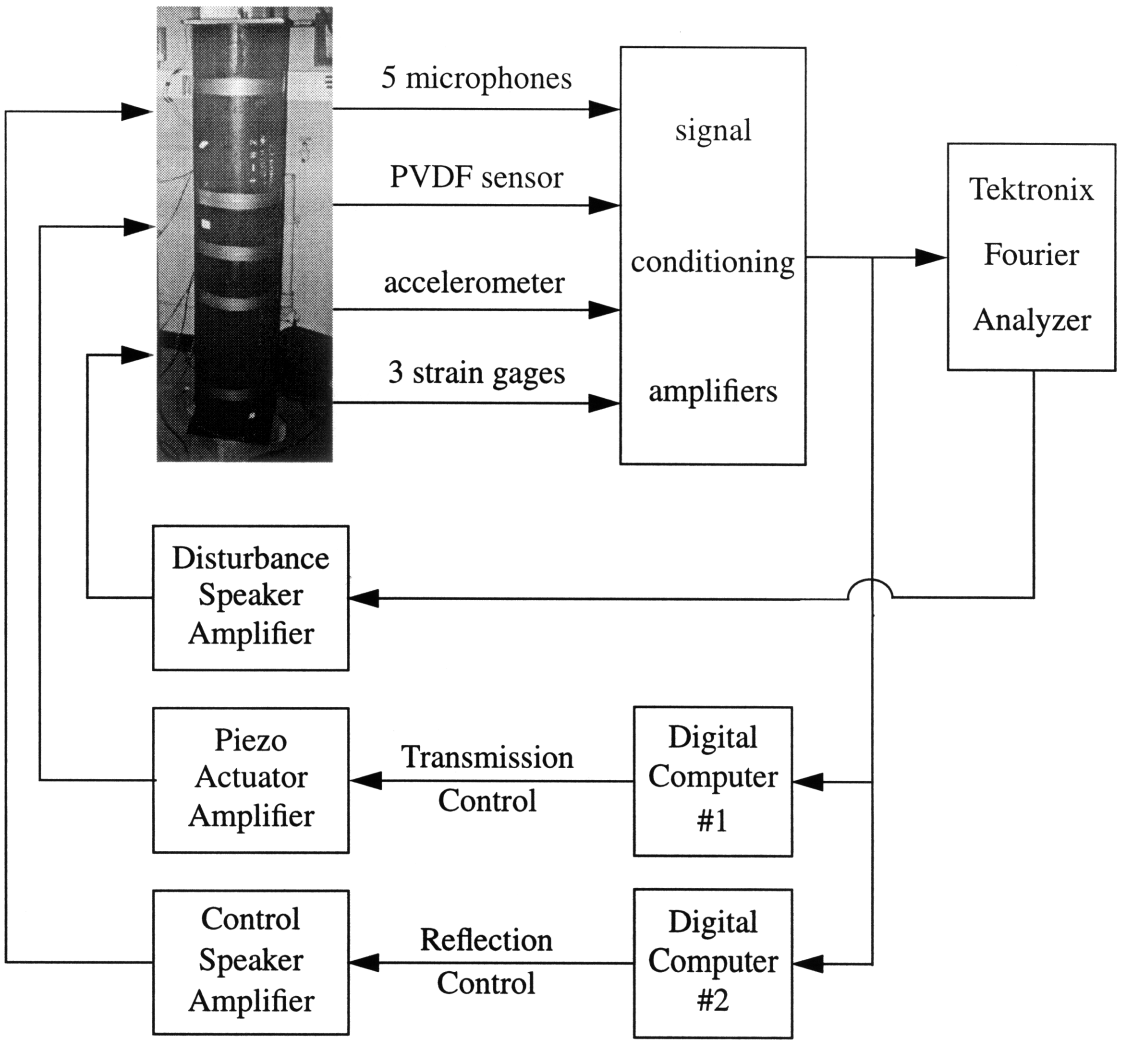

Figure 2.8: Block diagram of experimental setup

conditioner and microphone power supply is the bank of strain gage conditioners, and below that are the conditioning electronics for the microphone signals, capable of handling six microphones. Below the microphone conditioners and just above the Crown power amplifiers is a gain box, used for changing the gain on various sensor signals.

Not pictured in Figure 2.7 is the signal conditioner for the PVDF strain sensor. Initially, the PVDF sensor signal was conditioned using the gain box which has an input impedance of 100 kΩ. This was found to be too low, causing an apparent roll up in the phase at low frequencies leading to unbounded phase behavior. In order to fix this prob-

lem, a signal conditioning circuit was built using a protoboard and an operational amplifier to increase the input impedance to 10MΩ .

All of the data was taken using a Tektronix 2630 Fourier Analyzer. It is capable of recording time domain as well as frequency domain data simultaneously on four channels, as well as acting as a function generator to create the disturbance functions. Figure 2.8 shows a block diagram of the experimental setup used.

Chapter 3

Structural-Acoustic Modeling

Structural modeling for control involves modeling all of the components which affect the input-output nature of the system. There are three main components to the structural plant model. The first is the modeling of the structure itself, which includes its modal frequencies, modal damping ratios, and inertial properties. The second is the modeling of all actuator and sensor dynamics as well as appropriate gains for amplifiers or signal conditioners which are "in the loop." The third component includes any other systems to which the structure is coupled. This may include electrical, magnetic, acoustic, or fluid fields. The effects of these couplings on the structural modes, frequencies, and damping, as well as any new dynamics that these systems introduce must also be included in the structural plant model.

There are numerous ways in which a mathematical model of a physical system can be obtained. Two of the more well known methods of structural modeling for control are the finite element method and the measurement based technique.

3.1 Finite Element Model

To obtain a structural model using the finite element method, the structure is first discretized into a finite number of nodes at which forces and moments can be applied and displacements and rotations can be measured. The nodal displacements alone offer a very crude description of the structural displacements, so the nodes are connected by structural elements which model different structural behaviors, such as rods, beams, shafts, plates, and 3D solids. The displacements within these structural elements are described by interpolation functions. Given these interpolation functions and the nodal coordinates along with the material and cross sectional properties of the structure, it is possible to derive matrix equations which relate the element displacements, velocities, and accelerations to applied forces and moments. By applying the proper type of force or moment at the nodes corresponding to the actuator locations, and reading off the displacement, velocity, or acceleration at the sensor locations, it is possible to construct an inputoutput model of the structure compatible with modern state space control techniques.

Although less well known, the finite element method can also be used to obtain a model of an acoustic field. In this application, the acoustic field is discretized into a finite number of nodes connected by acoustic elements. The measurements at the nodes consist of pressures and pressure gradients, and the interpolation functions represent the variation of pressure within an acoustic element rather than the structural deformations within an element. By using the appropriate finite elements to represent the structure and the surrounding acoustic field, and coupling the structure and acoustics, a combined field structural-acoustic finite element model can be developed.

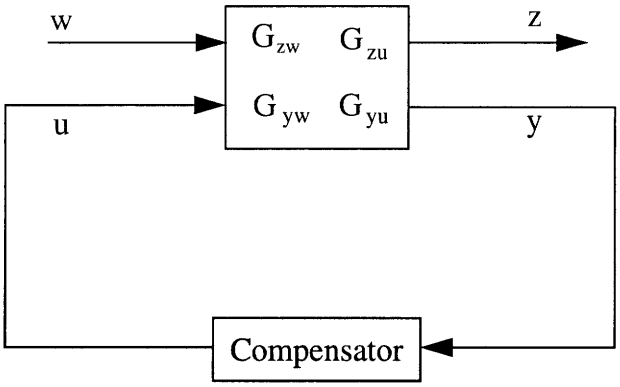

Figure 3.1: The four block problem

3.2 Measurement Model

The measurement based technique relies on open loop measurements of the structure's frequency response to excitations. Band limited white noise is used to excite all input channels (actuators and disturbance sources) and measurements are taken at all output channels (sensors and performance measurements). This provides the open loop transfer functions of the four block problem shown in Figure 3.1. They are the transfer function from control actuator to feedback sensor (G_{yu}), control actuator to performance sensor (G_{zu}), disturbance actuator to feedback sensor (G_{yw}), and disturbance actuator to performance sensor (G_{zw}).

Then, the Frequency Domain Observability Range Space Extraction (FORSE) technique developed by Jacques [20] is used to fit a model to the open loop frequency response data of the system. The FORSE algorithm is based on Liu's Observability Range Space Extraction (ORSE) algorithm [21] but is extended from arbitrary real signals to complex signals.

In order to capture all of the important dynamics of the system, it is necessary to over parameterize the model, resulting in a very large number of states. Since it is preferable in

terms of computation time to perform the control design with a minimal order model, the model must be reduced. This is done using a balancing realization in which the system is transformed so that the observability and controllability grammians are identically equal to the diagonal matrix of the Hankel singular values. For a non-minimal model, the last few states will have singular values which are much smaller than the others. These states can then be safely removed using standard model reduction techniques. The model must then be tuned to readjust any parameters which may need to be altered as a result of the model reduction. The model tuning consists of non-linear optimization algorithms applied to system identification. The Levenberg-Marquardt algorithm [22] designed to solve the non-linear least squares problem is used to minimize a cost function which is the sum of quadratic errors. This reduction and tuning process is repeated until a minimal, yet accurate model is obtained.

The advantages provided by the measurement based method are that it often produces an accurate model of the system which already includes all external influences such as coupling with other fields, any dynamics of the actuators and sensors, as well as any gains introduced by the amplifiers and signal conditioners. However, this method also has numerous drawbacks. First, it is sometimes not possible to obtain a model at all since the method relies on performance variables and disturbance sources which can be physically measured. A second drawback to this technique is that although the frequency, damping, and amplitude of the system poles can be specified readily, it is not possible to specify any information on the zeroes of the system. Subsequently, non-minimum phase zeros can occur in the model at various frequencies depending on the specific order in which modes were eliminated from the model or at what point in the reduction process the model was tuned. These non-minimum phase zeros do not manifest themselves in any visible manner when the model transfer function is plotted, but do limit the bandwidth of the controller.

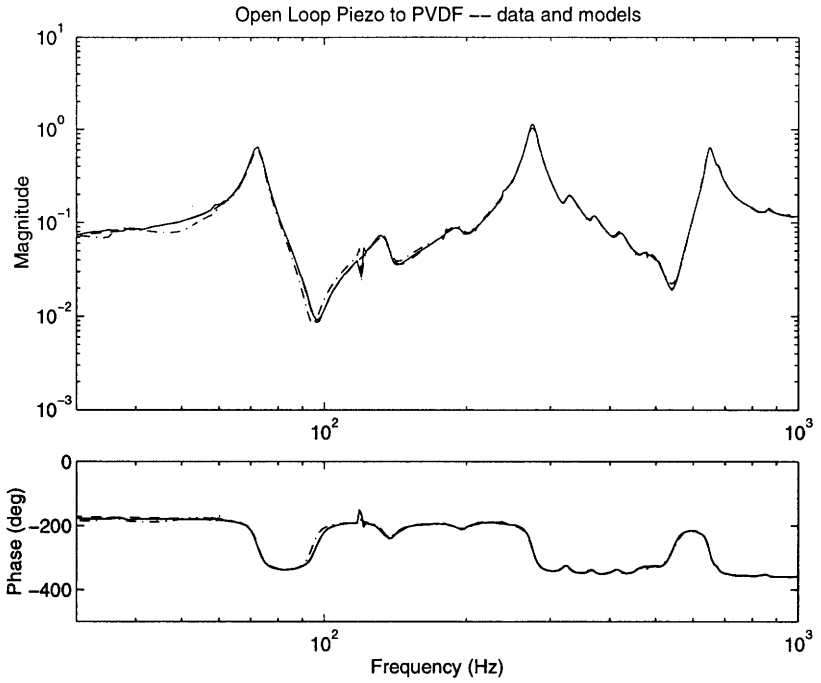

Figure 3.2: Open loop piezoceramic actuator to PVDF strain sensor transfer function (solid: data, dash: 44 state reduced model, dash-dot: 130 state model)

Therefore it is necessary to examine the pole-zero plot of the model after reduction and to redo the model reduction and tuning if necessary. The FEM can be used to complement the measurement model by helping to determine whether the non-minimum phase zeroes occur due to the physics or are artifacts of the model reduction. The final drawback to the measurement based model is that since the model obtained is simply a curve fit, all physical intuition into the dynamics of the system is lost.

In Figure 3.2 the piezoceramic actuator to PVDF strain sensor transfer function is shown, with the solid line showing the experimental data. The dash-dot line shows the initial model obtained using the FORSE algorithm which has 130 states. Clearly 130 states are not needed to accurately represent the dynamics of this system, and indeed many of the states represent modes which have very near pole-zero cancellations. Through the iterative process of model reduction and model tuning, the final design plant model of 44 states is

obtained. This model is shown in the plot as the dashed line. As can be seen from the very close overlay of the three transfer function plots, the initial 130 state model achieves very good accuracy and the reduction of the model to 44 states has very little effect on model accuracy. However, further reduction of the model does lead to a noticeably poorer fit with missing and mismodeled dynamics

3.3 Summary

Both a finite element model and a measurement based model were developed. The finite element model was developed by Robert Pascal using the ANSYS commercial finite element software. The FEM was useful in offering insight into the physical behavior of the plate and its coupling with the acoustics as it allowed the identification of the physical significance of the modes of the system. However, it was not possible to obtain a model with high enough accuracy for control design using the finite element method.

The measurement based technique offered an accurate model which incorporated all of the effects of the acoustics, the structural-acoustic coupling, the dynamics of the speakers, as well as all sensor and actuator dynamics. This modeling method was ultimately used in the control design.

Figure 3.3 shows a schematic diagram of the procedure used to obtain a measurement based model of the open loop system. First, the open loop transfer functions are measured and the FORSE algorithm is used to obtain an initial model. This initial model is balanced, reduced, and tuned to a obtain a reduced order model. This reduced model is compared with the open loop data and the finite element model to ensure that critical dynamics were not eliminated. Then, the balance, reduce, and tune steps are reiterated until a minimal order model which retains sufficient accuracy is obtained.

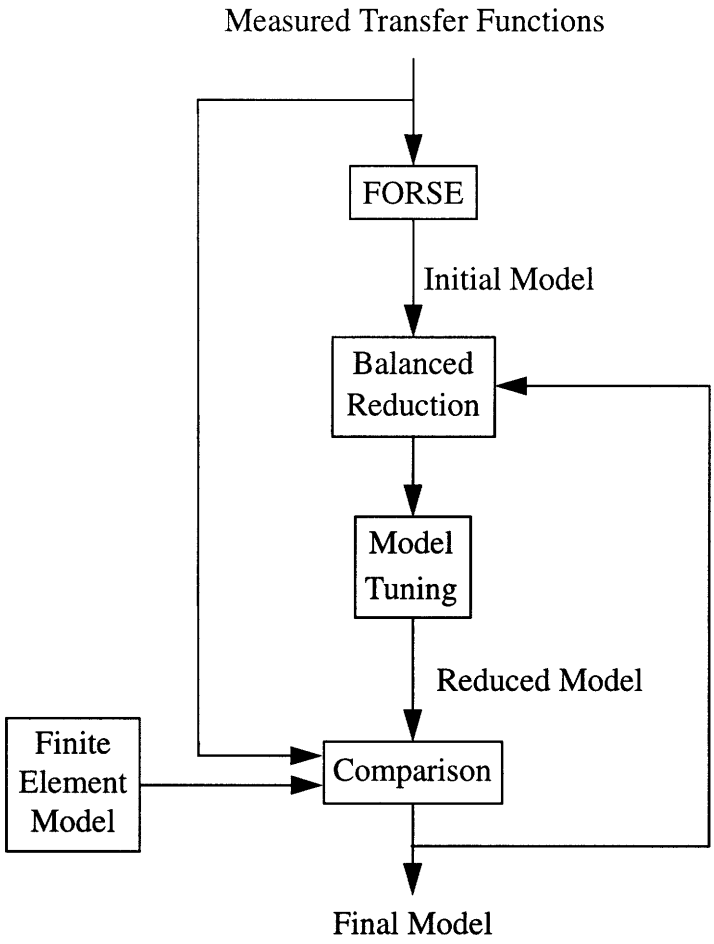

Figure 3.3: Block diagram of measurement modeling process

Chapter 4

Linear Quadratic Gaussian Control Design Techniques

The Linear Quadratic Gaussian (LQG) control design method is based on a linear model of the system, Gaussian noise, and a quadratic cost function. It can be viewed as having two separate components, the regulator and the estimator. The estimator employs Kalman filtering techniques to estimate the state vector from the output signals of the feedback sensors. The regulator then uses this estimated state vector to derive the control gains.

Given a standard state space representation of a stable open loop system

$$\begin{aligned} \dot{x} &= Ax + B_u u + B_w w \\ y &= C_y x + D_{yu} u + D_{yw} w \\ z &= C_z x + D_{zu} u + D_{zw} w \end{aligned} \tag{4.1}$$

the quadratic cost to be minimized for a standard LQG control design is given by

$$J_{LQG} = \int_0^\infty (x^T R_{xx} x + u^T R_{uu} u + 2u^T R_{xu} x) dt \tag{4.2}$$

where R_{xx} is the state penalty matrix, R_{uu} is the control penalty matrix, and R_{xu} is the cross-coupled penalty matrix. The control gain, G, and filter gain, H, can be derived inde-

pendently by solving the two algebraic Riccati equations

$$0 = SA + A^T S + R_{xx} - SB_u R_{uu}^{-1} B^T \text{ and } G = R_{uu}^{-1} B_u^T S \tag{4.3}$$

$$0 = A\Sigma + \Sigma A^T + B_w \Xi B_w - \Sigma C_y^T \Theta^{-1} C_y \Sigma \text{ and } H = \Sigma C_y^T \Theta^{-1} \tag{4.4}$$

where Ξ and Θ are the process and sensor noise intensities respectively. Then the equations for the compensator are given by

$$\dot{\hat{x}} = (A - B_u G - HC_y)\hat{x} + Hy$$

$$u = -G\hat{x} \tag{4.5}$$

where u is the control signal that is fed to the actuator.

4.1 Sensitivity Weighted LQG

Model based controllers such as LQG require an accurate model of the system. The control gains and Kalman filter gains are derived from the state space matrices provided by the system model. However, an accurate model is difficult to obtain because it is often impossible to know the exact properties of the physical system and the variations of these properties caused by environmental changes such as temperature and pressure. Inaccurate models may lead to poor performance or in the worst case, unstable closed loop systems.

Sensitivity weighting [23] is a method of designing LQG controllers which are robust to parametric errors in the model. Although these modeling errors may range from simple linear functions to complex non-linear functions of the system state space matrices, most errors in the model can be categorized into fundamental quantities such as frequency and damping of the system poles. In order to desensitize the standard LQG controller to certain parametric errors, a quadratic penalty on the sensitivity of the states to each of the uncertain variables is added to the standard LQG problem.

Let α denote the vector of uncertain parameters to which the control design is to be desensitized, and define the sensitivity state weighting matrix $R_{\alpha\alpha_i}$ with real entries such that it is symmetric and positive semi-definite. Then the state, control, and cross-coupled penalty matrices become

$$\Re_{xx} = R_{xx} + \sum_{i=1}^{n} \frac{\partial A}{\partial \alpha_i}^T A^{-T} R_{\alpha\alpha_i} A^{-1} \frac{\partial A}{\partial \alpha_i} \tag{4.6}$$

$$\Re_{uu} = R_{uu} + \sum_{i=1}^{n} \frac{\partial B_u}{\partial \alpha_i}^T A^{-T} R_{\alpha\alpha_i} A^{-1} \frac{\partial B_u}{\partial \alpha_i} \tag{4.7}$$

$$\Re_{xu} = R_{xu} + \sum_{i=1}^{n} \frac{\partial A}{\partial \alpha_i}^T A^{-T} R_{\alpha\alpha_i} A^{-1} \frac{\partial B}{\partial \alpha_i} \tag{4.8}$$

and the quadratic cost to be minimized becomes

$$J_{SWLQG} = \int_0^\infty (x^T \Re_{xx} x + u^T \Re_{uu} u + 2u^T \Re_{xu} x) dt \tag{4.9}$$

When desensitizing the design to errors in modal parameters such as frequency and damping of the poles, the effect of the sensitivity weighting is to reduce the control effort in the frequency region near that particular mode. Therefore, sensitivity weighting is not only useful in regaining performance or stabilizing a closed loop system, but it can also be used to shape the frequency domain characteristics of the compensator. By desensitizing the design to parameters of a mode near an unstable compensator pole, the unstable compensator can be stabilized, easing its implementation.

4.2 Frequency Weighted LQG

Often there is a gap between what the LQG controller achieves and the desired control system performance. This is due in large part to the discrepancy between the frequency

domain specifications of the control system performance and the time domain optimization method used by LQG. One method of overcoming this discrepancy is to use frequency weighted cost functionals [24] in which it is possible to specify different control and state penalties as a function of frequency.

Using Parseval's theorem, the time domain LQG cost functional is converted into the frequency domain

$$J = \int_{-\infty}^{\infty} (x^T(t)R_{xx}x(t) + u^T(t)R_{uu}u(t))dt$$

$$= \frac{1}{2\pi}\int_{-\infty}^{\infty} (x^H(j\omega)R_{xx}x(j\omega) + u^H(j\omega)R_{uu}u(j\omega))d\omega \tag{4.10}$$

Notice that both R_{xx} and R_{uu} are constant in the frequency domain. Therefore the standard LQG cost functional weights the states and controls equally at all frequencies. To add frequency domain specifications on the control system, frequency weights are added, giving the new quadratic cost functional.

$$J = \frac{1}{2\pi}\int_{-\infty}^{\infty} ((x^H(j\omega))W_1^H(j\omega)W_1(j\omega)x(j\omega) + u^H(j\omega)W_2^H(j\omega)W_w(j\omega)u(j\omega))d\omega \tag{4.11}$$

where both $W_1(jw)$ and $W_2(jw)$ are user specified frequency weights.

Minimization of the frequency weighted cost functional using LQG methods requires the transformation of the cost functional back into the time domain. This requires the state space realization of the frequency weights.

$$z_1(s) = W_1(s)x(s) \text{ with } W_1(s) = C_1(sI - A_1)^{-1}B_1 + D_1 \tag{4.12}$$

$$z_2(s) = W_2(s)u(s) \text{ with } W_2(s) = C_2(sI - A_2)^{-1}B_2 + D_2 \tag{4.13}$$

This allows the quadratic penalty given by equation 4.11 to be rewritten as

$$J = \int_{-\infty}^{\infty} (z_1^T(t)z_1(t) + z_2^T(t)z_2(t))dt \tag{4.14}$$

Minimizing this cost functional is equivalent to solving the LQG problem of the open loop

system given by augmenting the dynamics of the frequency dependent weights onto the original state space matrices. Thus the new open loop system is given by

$$\begin{bmatrix} \dot{x} \\ \dot{x}_1 \\ \dot{x}_2 \end{bmatrix} = \begin{bmatrix} A & 0 & 0 \\ B_1 C_y & A_1 & 0 \\ 0 & 0 & A_2 \end{bmatrix} \begin{bmatrix} x \\ x_1 \\ x_2 \end{bmatrix} + \begin{bmatrix} B_u \\ B_1 D_u \\ B_2 \end{bmatrix} u + \begin{bmatrix} B_w \\ B_1 D_w \\ 0 \end{bmatrix} w$$

$$\begin{bmatrix} z_1 \\ z_2 \end{bmatrix} = \begin{bmatrix} D_1 C_y & C_1 & 0 \\ 0 & 0 & C_2 \end{bmatrix} \begin{bmatrix} x \\ x_1 \\ x_2 \end{bmatrix} + \begin{bmatrix} D_1 D_u \\ D_2 \end{bmatrix} u + \begin{bmatrix} D_1 D_w \\ 0 \end{bmatrix} w \tag{4.15}$$

and thus the frequency weighted cost becomes

$$J_{FWLQG} = \int_{-\infty}^{\infty} (X^T C_{aug}^T C_{aug} X + 2 C_{aug}^T D_{aug} u + u^T D_{aug}^T D_{aug} u) dt \tag{4.16}$$

This revised weighting function is used to derive the frequency weighted LQG controller. Note that due to the augmented dynamics of the frequency weighting, a FWLQG controller will have more states than a standard LQG controller designed using the same plant model.

4.3 Summary

Techniques of the Linear Quadratic Gaussian control design have been presented including two variations: sensitivity weighted LQG and frequency weighted LQG. The design of the compensators using these methods will be discussed in Chapter 5. The sensitivity weighting will be used primarily to stabilize the compensator, although it will also be used to reduce amplification at certain frequencies. The frequency weighting will be used to force compensator roll off at high frequencies to stabilize the closed loop system.

Chapter 5

Control Design Process

There are two fundamental control problems in the attenuation of acoustics inside the launch vehicle shroud. Since most of the acoustic disturbances originate from outside the shroud, the acoustic environment within the enclosure can be attenuated by reducing the transmission of sound through the structure. However, a reverberant acoustic environment within the enclosure is inevitable since it is unfeasible to totally eliminate acoustic transmission and also since acoustic disturbances can originate from within the enclosure. The reverberation within the chamber is caused by the reflection of sound waves at the ends of the waveguide. Therefore by placing an actuator at one end of the waveguide and controlling its reflection coefficient, attenuation of the acoustic cavity modes can be achieved.

This chapter presents the chronology of the attempts at implementation of a control design to effectively attenuate the acoustics. The use of various sensors for the transmission control are investigated and the problems with each setup are discussed. Upon obtaining a satisfactory transmission control, the subsequent problems with the implementation of the reflection control are discussed.

5.1 Transmission Control

A significant portion of the acoustic disturbances enter the payload fairing via transmission through the structure of the shroud. Therefore reducing the acoustic transmission through the structure will lead to attenuation of the interior acoustic environment.

The physics of acoustic transmission through a thin plate are as follows. Sound waves are pressure waves, and pressure is simply a distributed force. So as the sound waves impinge upon the structure, the structure vibrates in response to the distributed force. This structural vibration in turn creates differential pressure on the other side of the structure, and radiates sound waves. Therefore, by preventing the structure from vibrating in response to incoming acoustic disturbances, acoustic transmission can be attenuated.

However, in order to totally eliminate acoustic transmission through the plate, there must be no vibration of the plate. The plate must be made to act as a rigid wall, reflecting back all of the incoming acoustic energy. This would require careful placement of a large number of sensors and actuators to effectively control all of the modes of the plate. In effect this is not possible without adding significant mass to the plate which must be avoided. The other option is to control the plate in order to absorb all of the incoming acoustic energy and to dissipate it as another form of energy such as heat. This would require a similarly prohibitive number of sensors and actuators as well as being a more difficult control problem. In addition, the problem becomes far more difficult when the simple circular plate is replaced by the complex three dimensional structure of the actual launch vehicle shroud. Therefore, the best compromise is to identify the frequency range which contains a few of the structural modes which are important in the transmission of acoustics and to concentrate the control efforts in that range.

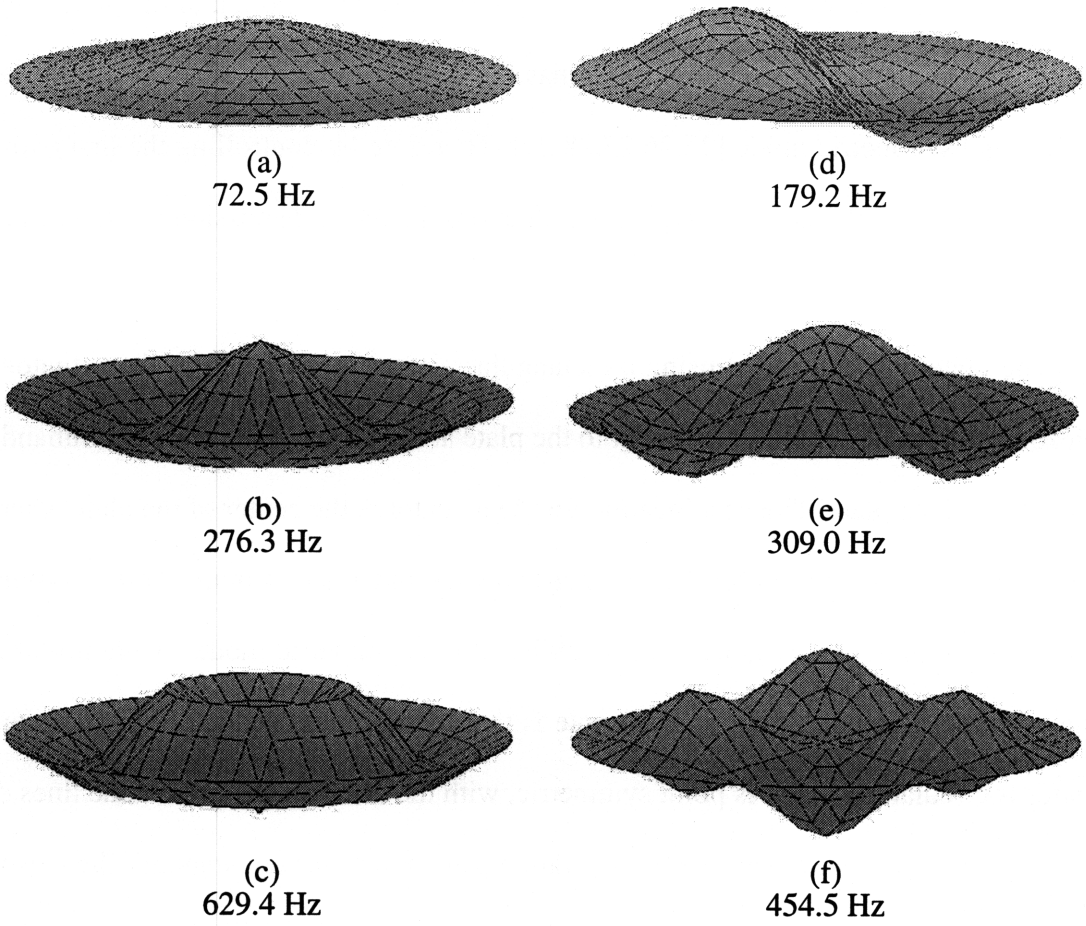

Figure 5.1: First six mode shapes of a circular plate with clamped boundary conditions

5.1.1 Plate Dynamics

The mode shapes and natural frequencies of a circular plate with clamped boundary conditions are well known. The mode shapes of the first six structural modes of the plate are shown in Figure 5.1. The structural mode shapes of the plate consist of two types: symmetric and asymmetric modes. Symmetric modes are circumferentially symmetric and have circular node lines. Modes (a), (b), and (c) are the first three symmetric modes of the plate. Asymmetric modes on the other hand have node lines which are diameters of the circle. Modes (d), (e), and (f) are the first three asymmetric modes of the plate.

Symmetric modes are more efficient in radiating sound than are asymmetric modes, particularly the lower order modes since they have the largest motion of the plate center of mass. The fundamental structural mode has the highest radiation efficiency, followed by the second symmetric mode [25,26,27,28,29]. Therefore by controlling the first two symmetric modes of the plate, significant reductions in the transmission of sound can be achieved.

The plate was controlled using a rectangular piezoceramic patch as the actuator. The piezoceramic wafer applies a moment to the plate at the edges of the wafer, commanding a curvature to the plate. The best location for the actuator is the center of the plate where the curvature is at a maximum for the symmetric modes and at a minimum for the asymmetric modes, thus allowing for good controllability of the symmetric modes while not exciting the asymmetric modes. One point to note is that the optimum shape of the piezoceramic wafer is circular, so that it is point symmetric, with the same shape as the node lines of the symmetric modes. However, the piezoceramic patch used was rectangular. The reason for this is that cutting piezoceramic wafers into circles is quite difficult, and was deemed unnecessary as the rectangular piezo performed well enough.

5.1.2 Acceleration Feedback

Initially, only the first plate, shown in figure 2.5, was available. It was instrumented with a piezoceramic actuator as well as three strain gages, an accelerometer, and a microphone as sensors. The accelerometer and microphone were placed at the center of the plate to collocate the sensors and the actuator. Two of the three strain gages were placed 1.5 inches from the center of the plate while the third strain gage was placed 2.5 inches from the edge of the plate. All three strain gages were placed with their sensitive axis along the radius of the plate.

There are two main problems with using a strain gage as a sensor in conjunction with a piezoceramic actuator. First, if the strain gage is not collocated with the piezoceramic actuator, then the actuator to sensor transfer function will have missing zeros and a phase rolloff, limiting the controller bandwidth. If the strain gages are collocated with the actuator, a new problem arises. Since the piezoceramic wafer commands curvature, and the strain gage senses strain, another form of curvature, the actuator to sensor transfer function becomes a series of pole zero cancellations, resulting in a simple feedthrough. Such a transfer function would provide no information on the dynamics of the plate, making control designs impossible. Therefore, use of the strain gages as feedback sensors is not feasible.

The accelerometer was chosen as the sensor over the microphone because of the nature of the control problem. The goal is to attenuate the transmission of acoustics into the lower chamber by controlling the structural modes of the plate. Therefore, it would make sense to use a structural sensor.

The piezoceramic actuator to accelerometer transfer function is shown in figure 5.2. This combination provides good observability of the first and second symmetric plate modes, at 73 Hz and 276 Hz respectively, with a collocated transfer function. However, it also has very high observability of the higher order symmetric modes and a dereverberated transfer function which rolls up, causing the higher order modes to have a higher amplitude than the modes of interest, posing some difficulties for the control design.

5.1.3 Position Feedback

In order to bring the slope of the dereverberated transfer function down, the sensor signal from the accelerometer is integrated twice, essentially providing a measure of the position. To avoid the infinite energy at low frequencies which results from the integration, the dou-

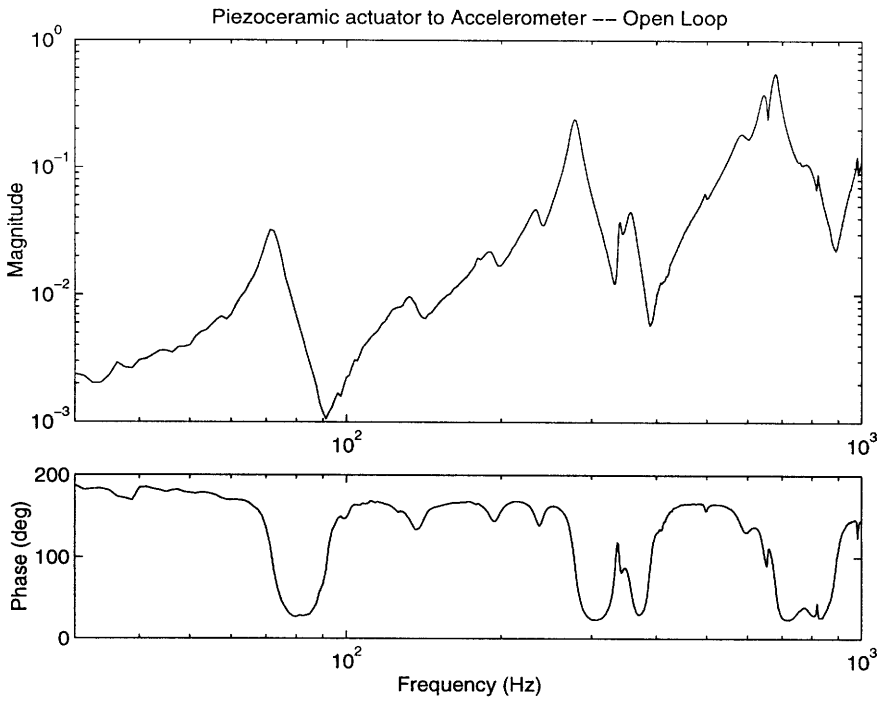

Figure 5.2: Open loop transfer function from piezoceramic actuator to accelerometer

ble integration is actually done with a second order low pass filter with a corner frequency at 10 Hz. The low pass filter was implemented using a HEURIKON digital computer operating at 8.6 kHz. The open loop transfer function from the piezoceramic actuator to the position sensor is shown in figure 5.3. Notice that the dereverberated transfer function is now sloped down, while maintaining the high observability of the relevant modes. Also, note the slow phase rolloff which results from the digital implementation of the filter.

A measurement model of the piezoceramic actuator to position sensor transfer function was obtained. A sensitivity weighted LQG control design was attempted, with the goal of adding damping to the first and second symmetric modes of the plate. Only minimal performance improvements were possible before an unstable compensator would result. The difficulties encountered are due at least in part to the phase rolloff resulting from the digital implementation of the low pass filter.

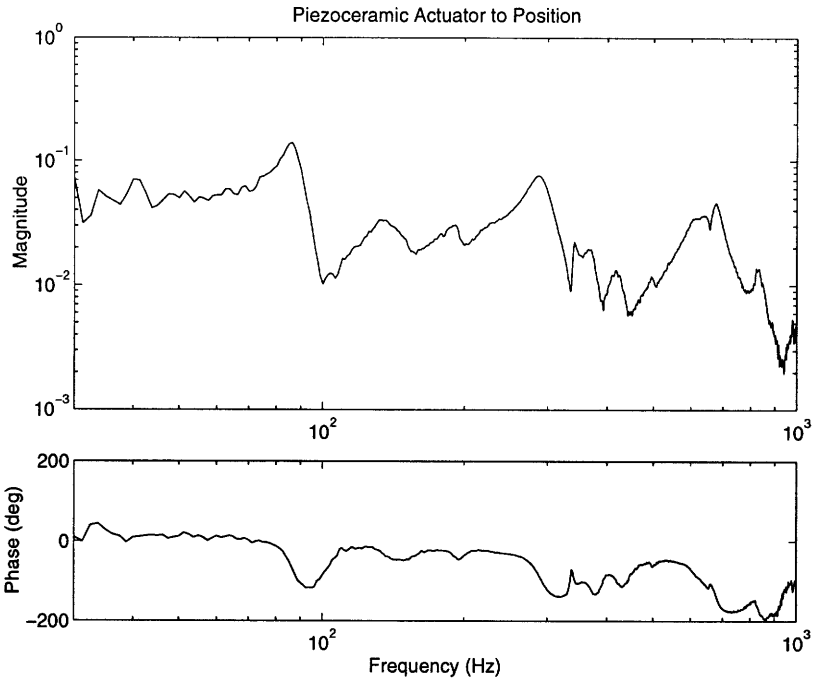

Figure 5.3: Open loop transfer function from piezoceramic actuator to position

A reasonable solution to this problem is to implement an analog low pass filter in order to eliminate the time delay imposed by the digital computer. This scheme was never implemented because of the development of a new structural sensor designed specifically for the plate which would eliminate the need for filters while possessing better characteristics in terms of observability of the relevant modes.

5.1.4 Strain Feedback

Polyvinylidene flouride (PVDF) piezoelectric film is a long chain polymer plastic which produces an output voltage when strained. Its main advantage is its ability to be shaped very easily to alter its frequency domain characteristics. The film which is manufactured in large sheets can either be cut to the desired shape or electroded only over the desired area to form a specific shape for the sensor. The sensor shaping can be used to cause sensor rolloff at high frequencies to allow for easier controller rolloff, vary the observabilities of certain modes to allow for better closed loop performance, and also to tailor the phase

characteristics of the actuator to sensor transfer function [30].

The design of the PVDF sensor is based on an extension of one-dimensional beam theory and on modal analysis of the plate. The strain on the surface of a beam undergoing transverse bending is given by

$$\varepsilon(x) = \frac{h}{2} w''(x, t) \tag{5.1}$$

where h is the thickness of the beam and $w(x,t)$ is the displacement. The output voltage supplied by the PVDF is given by the area integral of the surface strain multiplied by the piezo strain constant of the material, D_{31}. Therefore, the output voltage for a rectangular sensor of unit width extending from $x=a$ to $x=b$ will have an output voltage of

$$y(t) = \int_a^b \frac{h}{2} D_{31} w''(x, t) dx = \frac{h}{2} D_{31} (w'(a, t) - w'(b, t))) \tag{5.2}$$

The determination of the parameters a and b is dependent on a modal representation of the beam displacement given by

$$w(x, t) = \sum_{i=0}^{\infty} \phi_i(x) q_i(t) \tag{5.3}$$

where $\phi_i(x)$ are the mode shapes of the beam. Therefore, in order for the sensor to have high observability of a specific mode, a and b should be chosen so that the difference of $\phi'_i(a)$ and $\phi'_i(b)$ is near maximum. Similarly, in order for the sensor to have low observability of a specific mode, a and b should be chosen so that the difference of $\phi'_i(a)$ and $\phi'_i(b)$ is very small. This is useful in control design problems in which specific modes are targeted for closed loop performance. It allows the sensor to have high observability of specific modes allowing for higher control authority while having low observability of the other modes allowing for easier rolloff of the compensator.

In addition, if the location of the actuator is known, the phase characteristics of the actuator to sensor transfer function can be specified. The sign of the modal residue can be

found by multiplying the modal slope evaluated at the actuator by the modal slope evaluated at the sensor. If the modal residues of adjacent modes have the same sign, then there will be a zero between the modes, with phase recovery between the modes. However, if they have opposite signs, then there will be no zero between the modes leading to a phase loss of 180°. Phase loss in the actuator to sensor transfer function should to be avoided since it limits the allowable compensator gain and decreases the compensator's robustness to modeling errors.

The sensor design techniques described above can be extended to the circular plate by taking a slice of the plate through the center. For a circular sensor of radius r centered on the plate, the strain averaging results in the line integral of the rotation around the circle of radius r. So the output voltage is given by

$$y(t) = \oint_0^{2\pi} \frac{h}{2} D_{31} w'(r, \theta, t) d\theta \tag{5.4}$$

where C is the circle of radius r, centered on the plate. One important and useful side effect of the circular sensor is that asymmetric modes become unobservable due to the integration of the rotation around the circle.

Two PVDF sensors were designed by Carl Blaurock of Midé Technologies. The first is designed to have high observability of the first two symmetric modes of the plate while having low observability of the third symmetric mode to facilitate compensator roll off. No attempt is made to specify the phase behavior of the actuator to sensor transfer function. The sensor is shaped so that its circumference lies on the rotation nodeline of the third symmetric mode, at a radius of 4.6 inches. The finite element model of the plate was used to determine the location of the nodeline.

The second sensor was also designed to have high observability of the first and second symmetric modes and low observability of the third mode, but it was also designed to

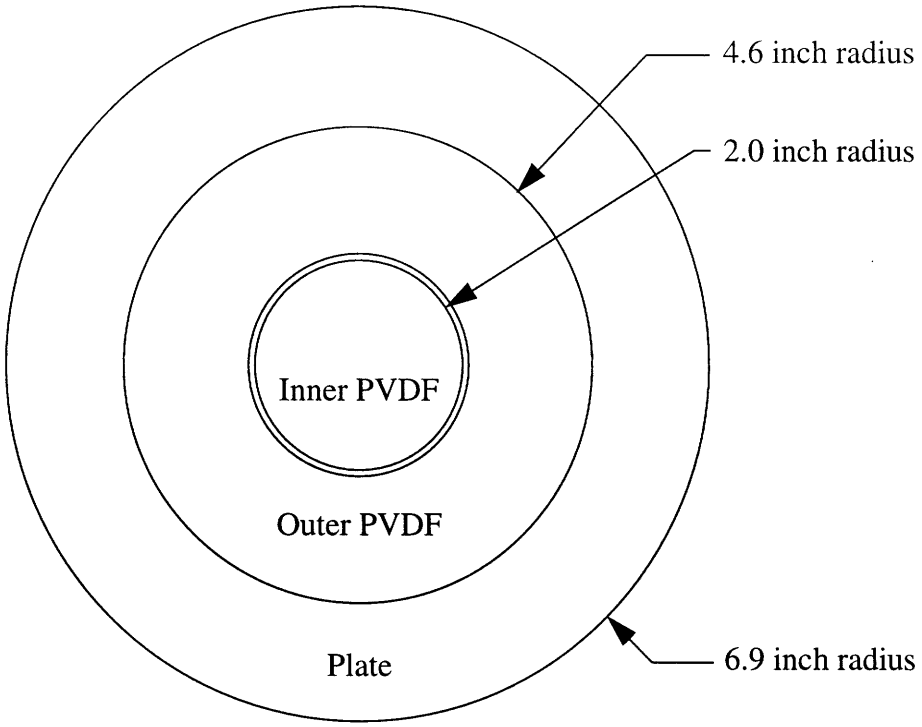

Figure 5.4: Schematic diagram of PVDF strain sensor

maintain bounded phase to at least the third mode. The sensor in this case is shaped so that its circumference is within the first nodelines of all three modes with a radius of 2.0 inches.

The two strain sensors were formed by cutting a circle with a 4.6 inch radius from the PVDF sheet and bonding it to the center of the plate. The second sensor was formed by removing the PVDF electrode in a circle with a 2 inch radius, thus electrically isolating the inner circle from the outer annulus. Lead lines were then attached to both the inner circle and the outer annulus along with a common ground line attached to the plate. Measurements with the 4.6 inch radius sensor can be made by tying the two signal leads together, thus summing the signals from the inner circle and the outer annulus. Measurements with the 2 inch radius sensor can be made by using the signal from the inner circle alone. Fig-

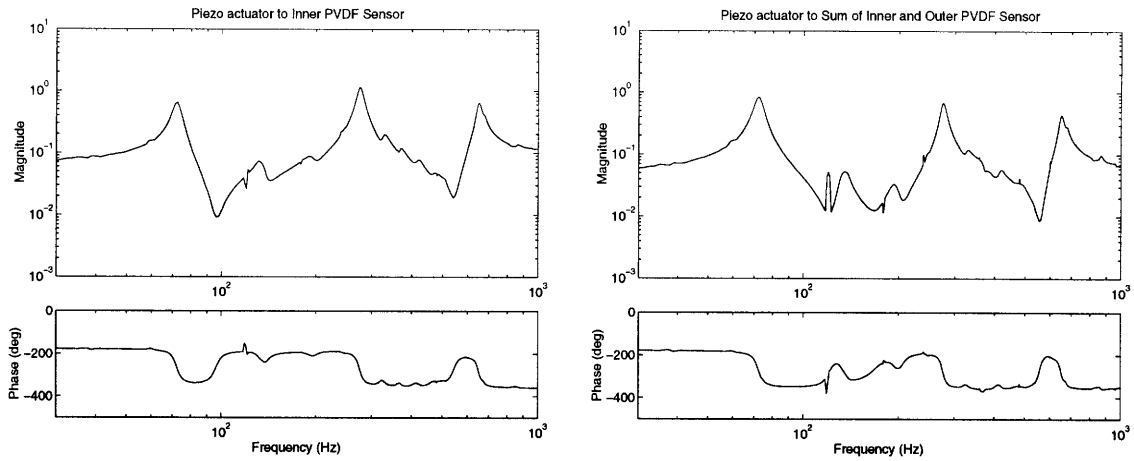

Figure 5.5: Piezoceramic actuator to inner ring PVDF sensor and full PVDF sensor transfer functions

ure 5.4 shows a schematic diagram of the PVDF strain sensor bonded to the aluminum plate.

Figure 5.5 shows the transfer functions from the piezoceramic actuator to the inner PVDF sensor and to the full PVDF sensor. Notice that both transfer functions show high observability of the first two symmetric modes at 73 Hz and 276 Hz respectively. However, the third symmetric mode near 630 Hz also has a high residue for both transfer functions. This is most likely due to the fact that the nodelines were predicted using a finite element model of a plate that was similar to but not identical to the plate to which the PVDF sensors were bonded. Both plates were made from the same aluminum material with a 32 mil thickness, but the plate onto which the PVDF was bonded had a slight warp which caused the two plates to have different dynamic behavior. For example, the fundamental mode for the plate with the PVDF is 73 Hz, while the same mode for the plate on which the FEM was based is 81 Hz. Therefore it is probable that the location of the nodeline predicted by the FEM does not match the actual nodeline on the plate, leading to the unexpectedly high observability of the third mode.

Both transfer functions show bounded phase behavior, making both sensors good candidates for use as feedback sensors. The choice was almost arbitrary but the inner PVDF sensor was chosen because of its cleaner transfer function in the region between the first two modes.

Using the inner ring of the PVDF film as the strain sensor, a measurement model of the open loop system was obtained. The system also included the disturbance speaker and the piezoceramic actuator. A sensitivity weighted LQG controller was designed using the modal velocities of the first two symmetrical structural modes as the state penalty. Significant damping of the structural modes was achieved leading to the addition of significant damping to the acoustics of the lower chamber at frequencies corresponding to those modes.

However, the acoustic cavity modes cannot be controlled with structural damping because of the weak coupling between the acoustic modes and the structural modes. Therefore, there is a fundamental limit to the possible performance improvement in a control scheme which only the adds structural damping. Therefore, alternate control schemes which can augment the transmission control to attenuate the acoustic cavity modes were examined.

5.2 Combined Transmission-Reflection Control

The control of acoustic reflection within the enclosure can be accomplished by altering the boundary condition at one end of the waveguide so as to reduce the acoustic reflection coefficient at that boundary. To accomplish this, a ten inch dual voice coil subwoofer speaker was placed at one end of the waveguide as the actuator at the controlled boundary. The lowest performance microphone was moved slightly to a position less than one centi-

meter above the speaker cone to form the collocated actuator-sensor pair. This microphone will act as the feedback sensor as well as the third performance microphone. To achieve better collocation of the sensor and actuator, the microphone should actually be bonded to the speaker cone. However, the microphone diaphragm is sensitive to acceleration. Therefore, if it were attached to the speaker cone, the microphone would sense the structural acceleration of the speaker in addition to the acoustic pressure, leading to a feedthrough term in the actuator to sensor transfer function. This problem can be alleviated by turning the microphone sideways so that the sensitive axis of the microphone diaphragm is orthogonal to the acceleration of the speaker cone. However, since a non-collocation of one centimeter leads to a time delay of merely $3x10^{-5}$ seconds and thus a missing zero at a frequency of 34 kHz, it was deemed unnecessary to place the microphone on the speaker cone.

One important distinction to be made is that although the actuator is a speaker, it will not be used as a secondary acoustic source to create cancelling waves as in Active Noise Control. Instead, the speaker will be used as a single degree of freedom structural actuator which controls the reflection of sound at the boundary and is therefore an Active Structural Acoustic Control method.

5.2.1 Multi-Input Multi-Output LQG Design

The use of two actuators and two sensors calls for a multi-input, multi-output control design. As with any LQG control design, a model of the open loop plant is required. For this problem, the disturbance actuator is the top speaker, the control actuators are the controlled speaker and the piezoceramic patch, the feedback sensors are microphone 4 and the PVDF strain sensor, and the performance sensors are the three microphones in the lower chamber. The signals from the three performance microphones are combined using the

root sum square method to arrive at a spatial average of the acoustic intensity in the lower chamber and to provide a single performance variable. Open loop transfer functions from all actuators to all sensors are taken and a measurement model of the open loop plant is derived. Because the model is attempting to fit nine transfer functions, the initial model is necessarily of very high order. The same iterative method of model reduction followed by model tuning is utilized, but the model quickly loses accuracy to such a degree as to render is useless as a design plant model. In order to maintain the model accuracy necessary to perform an LQG control design, the model requires more than 300 states, which is prohibitively large. Therefore, an alternate method is required.

5.2.2 Successive Loop Closure with LQG

The modeling problem encountered by the multi-input, multi-output control design can be avoided if the number of inputs and outputs of the system can be kept smaller. Fortunately, since the control actuators and feedback sensors used by the transmission control and the reflection control are mutually exclusive, the two control loops can be closed independently. This allows two single-input, single-output compensators to be designed using separate models, and be implemented in succession. Since the transmission control has already been designed and implemented, all that is required is to design a compensator to control the acoustic reflection. Because the reflection control is implemented after the transmission control, the transmission control closed loop system is the open loop system upon which the reflection control will be designed.

Figure 5.6 shows the transfer function from the controlled speaker to the feedback microphone with the transmission control implemented. Notice the missing zero between the first acoustic mode at 134 Hz and the speaker mode at 186 Hz. This results not from the physical non-collocation of the actuator and sensor but because of the nature of the

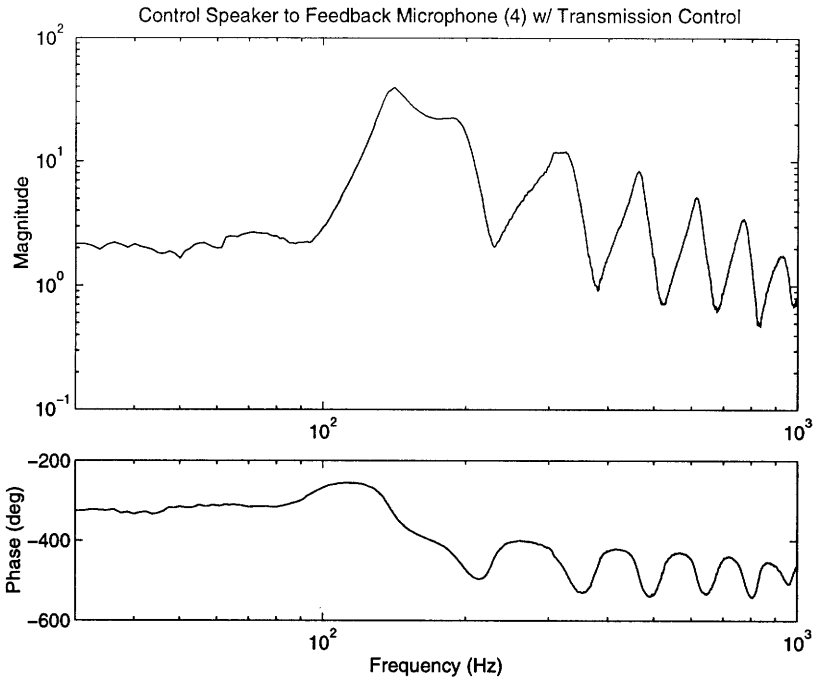

Figure 5.6: Controlled speaker to feedback microphone transfer function for reflection control

sensor and actuator. The actuator is driven by a current through the voice coil and is in effect a commanded force. The sensor is a microphone and thus senses pressure. Since the pressure sensor and the force actuator are not power duals, the physical collocation of the sensor actuator pair does not necessarily guarantee a collocated transfer function. The effect of this missing zero is to limit the control effort the compensator can exert in the frequency range near the missing zero, since a stable control loop requires gain stability of the loop transfer function at the frequency of the missing zero.

A measurement model was fitted to the open loop data using the FORSE algorithm and a sensitivity weighted LQG controller was designed using the modal velocities of the first three acoustic modes as the state penalty. Significant damping of these acoustic modes was achieved using the SWLQG method.

5.2.3 Successive Loop Closure with Impedance Matching

Another approach to the acoustic reflection problem is the acoustic impedance matching methodology developed by Glaese. The impedance matching design also uses the speaker as the actuator and the lowest microphone as the feedback sensor. However, instead of basing the control design on a measurement based model of the entire structural acoustic system, the impedance matching design is based on a model of the control actuator and its local coupling with the acoustic field.

The first step in the impedance matching control design is to obtain a model of the speaker. The speaker is a coupled electro-mechanical device. The mechanical dynamics of the speaker is that of a single degree of freedom mass-spring-dashpot system if the high frequency flexible dynamics of the speaker cone are ignored. The force which moves the speaker cone is provided by the interaction of a current carrying voice coil with a static magnetic field. The coupling factor Bl is a function of the strength of the static magnetic field, the number of turns in the voice coil, and the length and area of the voice coil. The voice coil also has an electrical resistance and an inductance which combine to form a real pole at a frequency of R_e/L_e. The coupled electro-mechanical behavior of the speaker is given by

$$\frac{d}{dt}\begin{bmatrix} u \\ \dot{u} \\ i \end{bmatrix} = \begin{bmatrix} 0 & 1 & 0 \\ -\frac{k}{m} & -\frac{c}{m} & \frac{Bl}{mL_e} \\ 0 & -Bl & -\frac{R_e}{L_e} \end{bmatrix} \begin{bmatrix} u \\ \dot{u} \\ i \end{bmatrix} + \begin{bmatrix} 0 \\ 0 \\ v_{drive} \end{bmatrix} \tag{5.5}$$

where u is the displacement of the speaker voice coil, i is the current in the voice coil, and v_{drive} is the driving voltage on the speaker. Note that the model also includes the back emf produced by the motion of the voice coil.

The actual parameters for the speaker were obtained from the specification sheet for the speaker as well as from actual measurements. In addition to the structural stiffness of the speaker cone, the speaker dynamics are acoustically stiffened by both the front and back enclosures. Therefore the stiffness used in the above equation is the effective stiffness of the speaker with both front and back enclosures. The physical parameters of the speaker are shown in Table 5.1. These values lead to a mechanical resonance at 186 Hz and an electrical resonance at 842 Hz.

In order to design a compensator using the LQG method, the performance variables must be determined, and the sensors, actuators, and disturbance source must be modeled. Since the problem consists of controlling the acoustic reflection coefficient of the speaker, the most natural choice for the disturbance is the incoming acoustic pressure amplitude, and for the performance variables, the incoming and outgoing acoustic pressures. However, the only possible acoustic measurement is the total acoustic pressure. The following equations can be used to relate the total surface acoustic pressure to the incoming and outgoing acoustic pressures.

$$P_o = P_i + \rho_o c_o \dot{u} \tag{5.6}$$

$$P = 2P_i + \rho_o c_o \dot{u} \tag{5.7}$$

where P_o, P_i, and P are the outgoing, incoming, and total acoustic pressures, ρ_o is the ambient density of air, c_o is the speed of sound in air, and u is the displacement of the speaker cone.

The final step in the LQG design is to determine the state and control weighting matrices. The state weighting matrix is chosen to be the acoustic power flow matrix given by

$$P_m = \begin{bmatrix} P_{ii} & P_{io} \\ P_{oi} & P_{oo} \end{bmatrix} = \frac{2}{\rho_o c_o} \begin{bmatrix} -A & 0 \\ 0 & A \end{bmatrix} \tag{5.8}$$

Table 5.1: Speaker Parameters

Parameter	Symbol	Value
moving mass	m	33.2 g
effective stiffness	k	4.79×10^4 N/m
damping	c	7.32 Ns/m
coil resistance	R_e	11.9 Ω
coil inductance	L_e	2.25 mH
effective area	A	0.0330 m^2
electro-mechanical coupling factor	Bl	9.83 N/A

since the performance variables are simply the incoming and outgoing acoustic pressure amplitudes. The control weighting matrix is simply the scalar value ρ, since there in only one actuator.

5.3 Summary

The vibro-acoustic loads inside the payload fairing arise from the transmission of acoustic disturbances from the outside environment as well as from the acoustic reverberation within the enclosure. Attenuation of acoustic transmission through the structure was achieved using a PVDF strain sensor and a piezoceramic actuator to add damping to the first two symmetric modes of the plate. However, due to the weak coupling between the structural modes and the acoustic cavity modes, the structural sensing and actuation alone did not add appreciable damping to the acoustic cavity modes. Therefore, a second actuator sensor pair was added to the control design to control the reflection of sound within the enclosure. Due to modeling difficulties posed by a multi-input, multi-output control design, the method of successive loop closure was used. First, the transmission of sound

into the fairing enclosure was controlled using an SWLQG controller using strain feedback. Then the reflection of sound within the fairing enclosure was controlled using two types of controllers: an SWLQG controller using pressure feedback and an acoustic impedance matching controller.

Chapter 6

Experimental Results

The final control design discussed in Chapter 5 employs successive loop closure to first attenuate acoustic transmission through the plate, and then attenuate acoustic reflection within the enclosure. To verify this approach, the compensators were implemented on the test chamber in the laboratory. The experimental data obtained from the experiments are presented in this chapter.

6.1 Open Loop

The structural-acoustic test chamber has three actuators and six sensors. The three actuators are the top and bottom speakers and piezoceramic patch. The six sensors are the five microphones and the PVDF area averaging strain sensor. The actuators can be divided into two categories, the control actuators (u) and the disturbance actuators (w), and the sensors can also be divided into two categories, the feedback sensors (y) and the performance sensors (z). The individual actuators and sensors can fall into the two categories depending on the requirements of the specific control scheme. For instance, in the case of transmission control, the top speaker provides the disturbance and the piezoceramic patch is the control

actuator. The feedback sensor is the PVDF strain sensor and microphones 3, 4, and 5 are the performance microphones. In the case of reflection control, the disturbance is again the top speaker, but the control actuator is now the bottom speaker and the feedback sensor is now the microphone which is collocated with the control speaker (microphone 4). The performance sensors are still microphones 3, 4, and 5. The performance microphones are located throughout the length of the lower chamber to observe the global behavior of the acoustics within the lower chamber. A combined performance of the global acoustic levels in the lower chamber can be obtained using the root sum square (RSS) of the three performance microphones to obtain a form of the spatial average of the three measurements.

Since the control design was based on successive loop closure with the structural control loop being closed first, the open loop transfer functions discussed here are based on the control topology of the structural control. So the disturbance is supplied by the top speaker, the control is the piezoceramic patch, the feedback sensor is the PVDF, and the performance sensors are the three microphones in the lower chamber. The "open loop" transfer functions for the acoustic control will be discussed later.

The G_{yu} transfer function shows the response of the feedback sensor to an excitation of the control actuator. Figure 6.1 shows the transfer function from the piezoceramic patch to the inner ring of the PVDF strain sensor. The highly observable and controllable poles near 73 Hz and 276 Hz are the first and second symmetric modes of the plate, respectively. The poles with low observability and controllability which show up in the transfer functions as near pole-zero cancellations are asymmetric modes of the plate, acoustic modes of the lower chamber, and dynamic modes of the speaker. Another important characteristic of this transfer function is the bounded phase behavior in the low frequency region below 1 kHz. This is due to the collocation of the sensor and actuator which results in an alternating pole-zero pattern. However, at higher frequencies, the alternating pole-zero pattern

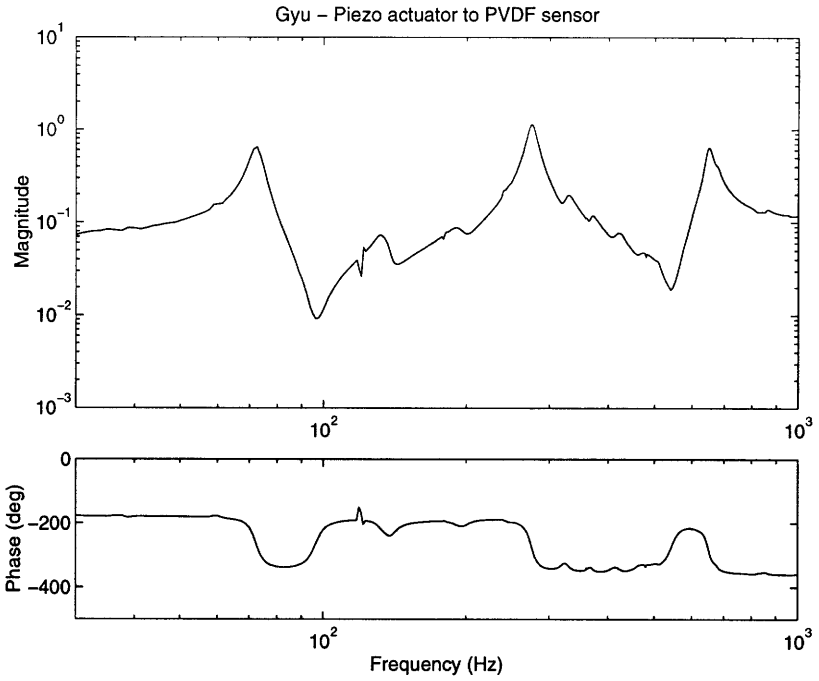

Figure 6.1: Open loop *Gyu* transfer function for transmission control

stops, leading to a rolloff in the phase. This is due to the fact that the actuator and sensor are not purely collocated and also to the dynamics of three dimensional acoustic modes at higher frequencies. Since this occurs at a high enough frequency, it does not affect the stability of the closed loop system. The compensator has the opportunity to roll off before the non-collocation becomes apparent, resulting in gain stability of the closed loop system.

The G_{zu} transfer functions show the responses of the performance sensors to an excitation of the control actuator. Figure 6.2 shows the transfer functions from the piezoceramic patch to the three performance microphones. Since none of these microphones are collocated with the plate, these transfer functions do not exhibit the alternating pole-zero pattern and bounded phase characteristic of collocated transfer functions. The non-collocation causes a propagation delay between the actuator and sensor which equals the ratio of the distance between actuator and sensor and the speed of sound. This propagation

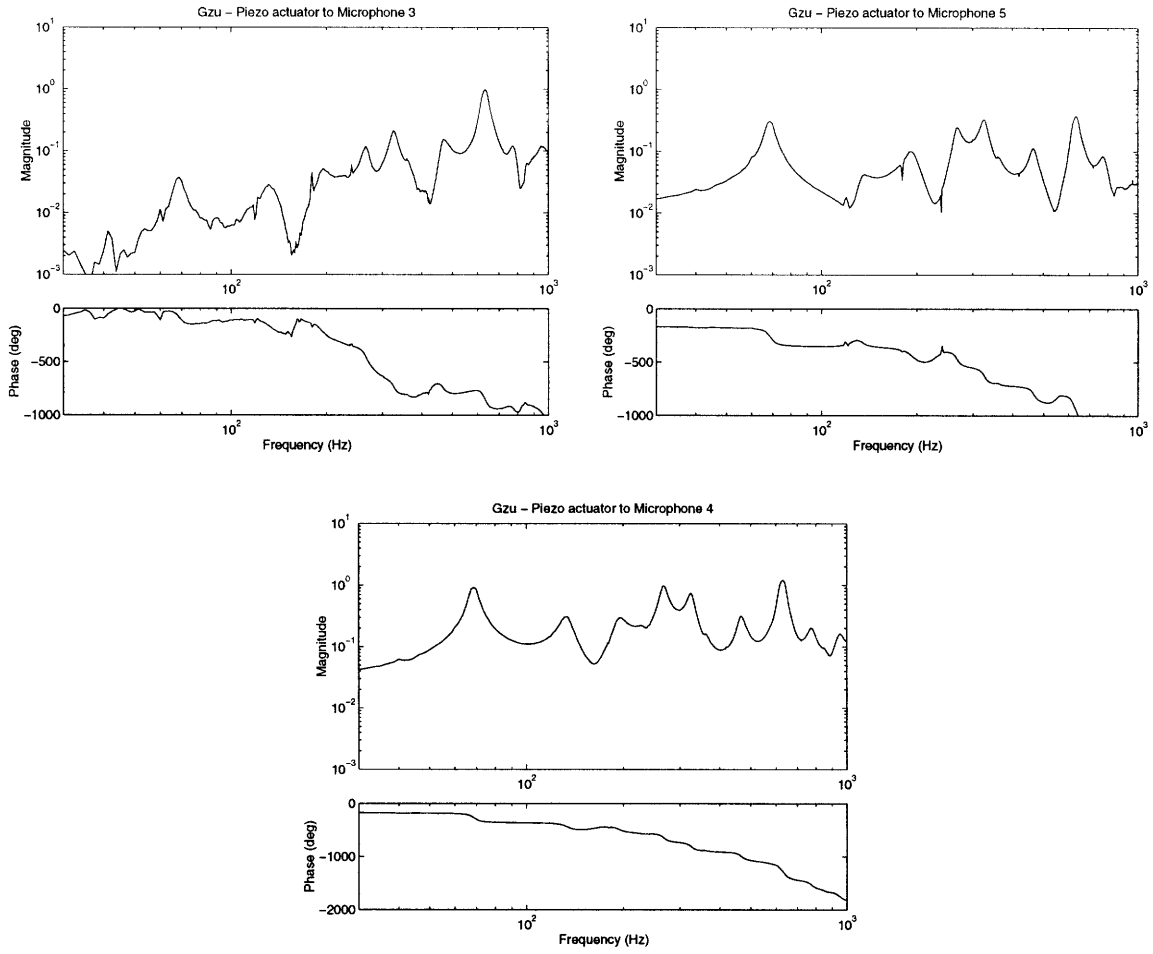

Figure 6.2: Open loop *Gzu* transfer functions

delay results in missing zeros between poles, with the number of missing zeros directly corresponding to the distance between the actuator and sensor.

The G_{yw} transfer function shows the response of the feedback sensor to an excitation of the disturbance actuator. Figure 6.3 shows the transfer function from the disturbance speaker to the inner ring of the PVDF strain sensor. Again, the actuator and the sensor are not collocated, so there are missing zeros in the transfer function as well as a significant roll off in the phase. This transfer function shows significant peaks at the frequencies of the first and second symmetric structural modes of the plate, as expected since the sensor used is the PVDF strain sensor which is sensitive to those modes.

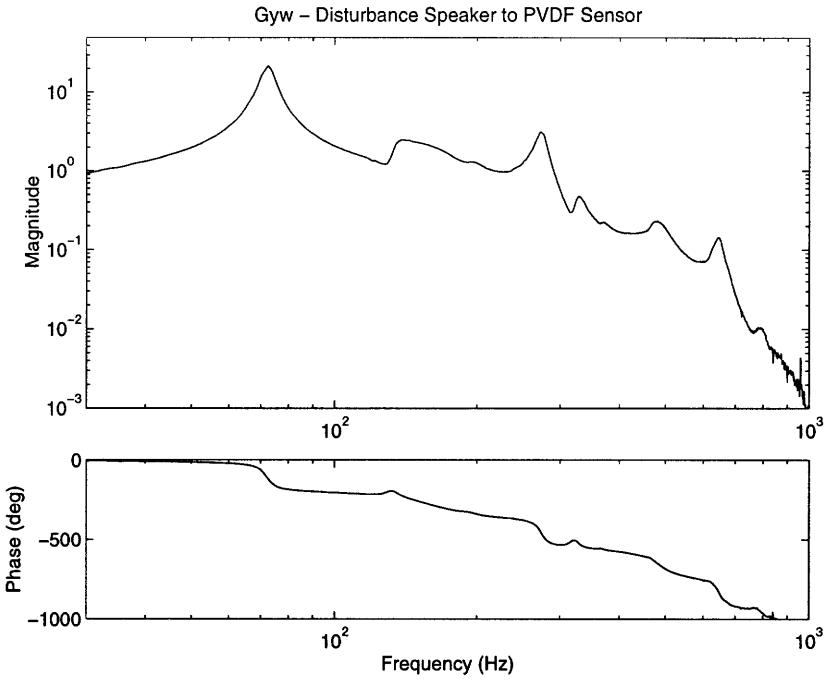

Figure 6.3: Open loop *Gyw* transfer function

The G_{zw} transfer functions show the responses of the performance sensors to an excitation of the disturbance actuator. Figure 6.4 shows the transfer functions from the disturbance speaker to the three performance microphones in the bottom chamber as well as to the RSS of the three performance microphones. The modes with the largest amplitudes in the disturbance to microphone RSS transfer function contribute the most to the transmission of sound from the outside environment into the fairing enclosure. Therefore, adding damping to these modes will result in the most significant overall performance improvement. These modes include the first and second structural modes at 73 Hz and 276 Hz, respectively, and the first and second acoustic modes of the lower chamber at 134 Hz and 325 Hz, respectively. Notice that the frequency of the second acoustic mode is not double the frequency of the fundamental mode. This is due to the coupling of the acoustics with the dynamics of the speaker. The frequency of the fundamental acoustic mode is pushed down from 166 Hz to 134 Hz and the speaker mode is pushed up from 171 Hz to 186 Hz.

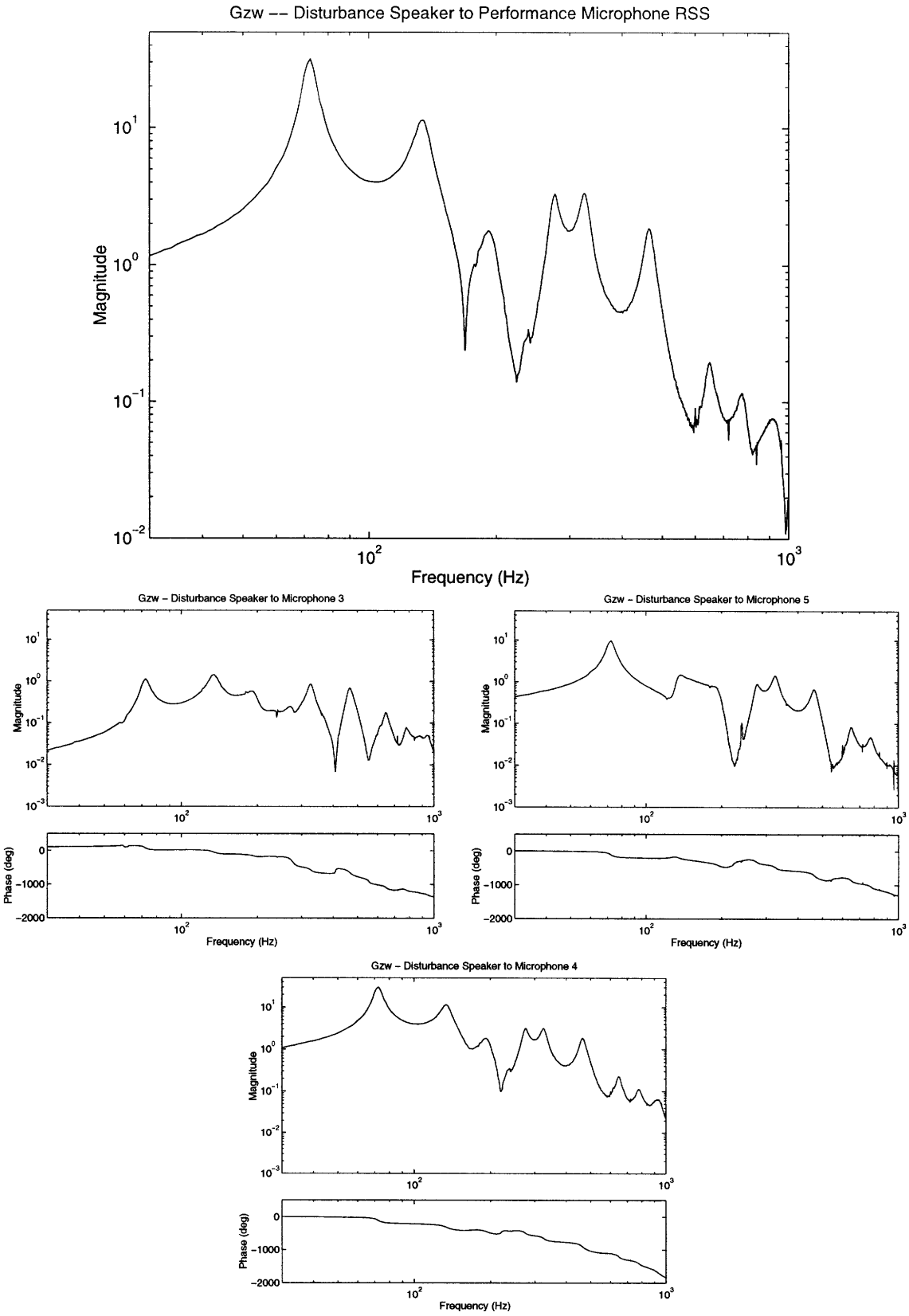

Figure 6.4: Open loop *Gzw* transfer functions

6.2 Transmission Control

The compensator used for structural control of the aluminum plate was designed using the SWLQG method described in Chapter 5, and was implemented using a HEURIKON digital computer operating at a sampling frequency of 8.6 kHz. The digital implementation of the compensator results in an introduction of a time delay equal to one and a half sample periods which results in a phase lag in the compensator transfer function. This phase lag essentially limits the bandwidth of the compensator as the loop must be gain stable as it crosses over -180°. However, by incorporating the time delay into the design plant model using a padé approximation, the LQG algorithm can be made aware of the time delay and the control design done so as to maintain closed loop stability. For the transmission control, the targeted modes are the first and second symmetric modes of the plate. Therefore the necessary controller bandwidth is relatively small, so the limitations imposed by the time delay should not cause a problem.

Figure 6.5 shows the compensator transfer function and the Nichols plot derived from the loop transfer function formed by wrapping the compensator around the open loop G_{yu} data augmented with the padé approximation of the time delay. The design goal of the structural compensator was to add damping to the first and second symmetric modes of the plate. As such, there are two separate instances in which the loop gain is greater than unity, as seen in the Nichols plot, with each instance corresponding to one of the structural modes. The minimum phase margin supplied by this loop is 37° and the minimum gain margin is approximately 2 dB.

Figure 6.6 shows the closed loop transfer function from the disturbance speaker to the feedback sensor, the PVDF strain sensor. As was the goal of the control design, the first symmetric plate mode at 73 Hz and the second symmetric plate mode at 276 Hz are very

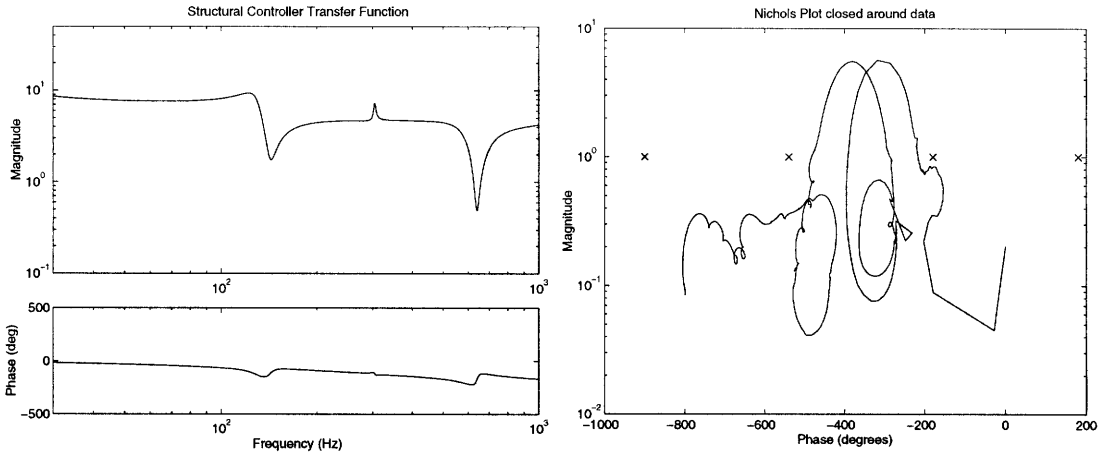

Figure 6.5: Transmission compensator transfer function and Nichols Plot based on the compensator wrapped around the open loop data

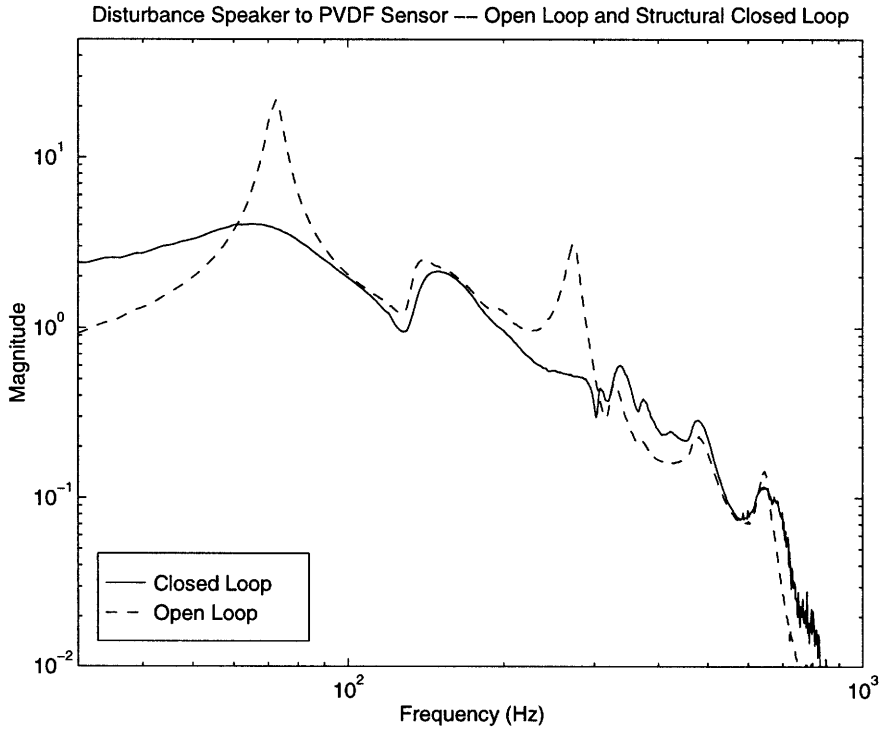

Figure 6.6: Transmission control closed loop and open loop disturbance speaker to PVDF sensor transfer functions

well damped, with performance improvements of 17.4 dB and 16.2 dB respectively. The broadband performance improvement measured between 10 Hz and 1 kHz is 4.6 dB.

However, the performance that is of greater interest is the acoustic attenuation in the lower chamber provided by the damping of the structural modes. Figure 6.7 shows the closed loop transfer functions from the disturbance speaker to the performance sensors. The top plot combines the three performance microphones using the root sum square method to obtain a measure of the spatially averaged performance. The remaining plots show the transfer functions for the three individual microphones. The combined performance transfer function shows that there is significant damping of the acoustics at the frequencies of the first two symmetric modes, with performance improvements of 17.8 dB and 17.3 dB respectively at those modes. The broadband performance improvement computed between 10 Hz and 1 kHz is 4.9 dB. Notice that the performance improvements shown in the closed loop disturbance to performance microphone plots closely reflect the improvements shown in the closed loop disturbance to feedback sensor plot.

Also, note that there is a slight amplification of the acoustics in the low frequency region below 50 Hz. Numerous attempts were made to eliminate this amplification using such techniques as frequency weighting, sensitivity weighting, and adding state penalties at low frequencies, but all attempts were unsuccessful.

The important point here is that using Active Structural Acoustic Control, global attenuation of the acoustics has been attained. Moreover, using only structural sensors and actuators, and with no knowledge of the acoustic modes of the enclosure, significant attenuation of the interior acoustic environment was attained. Although there is some amplification at certain frequency ranges, the achieved acoustic damping is observed at all locations within the lower chamber. This is in contrast to many other forms of acoustic

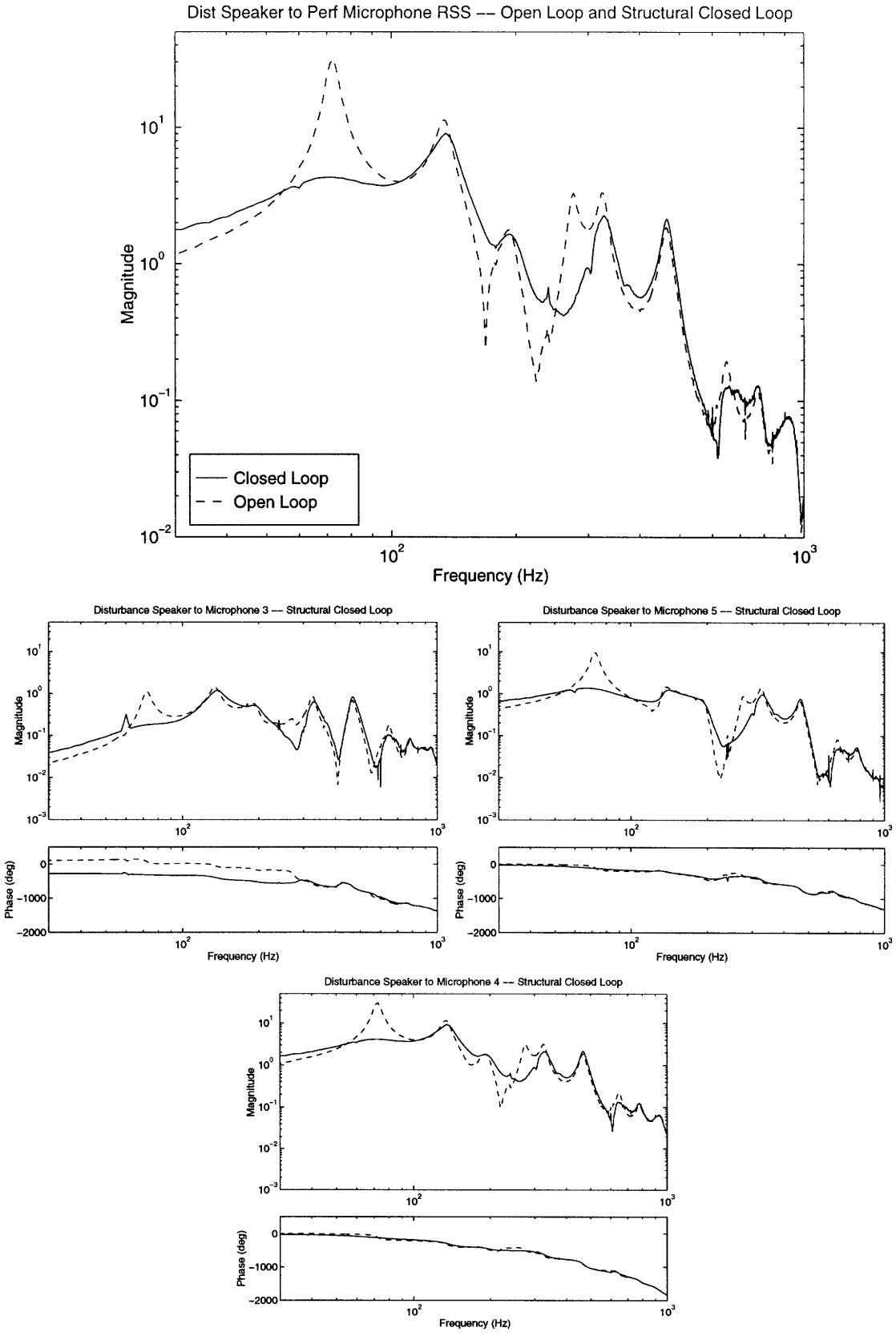

Figure 6.7: Structural closed loop and open loop disturbance speaker to performance microphone transfer functions

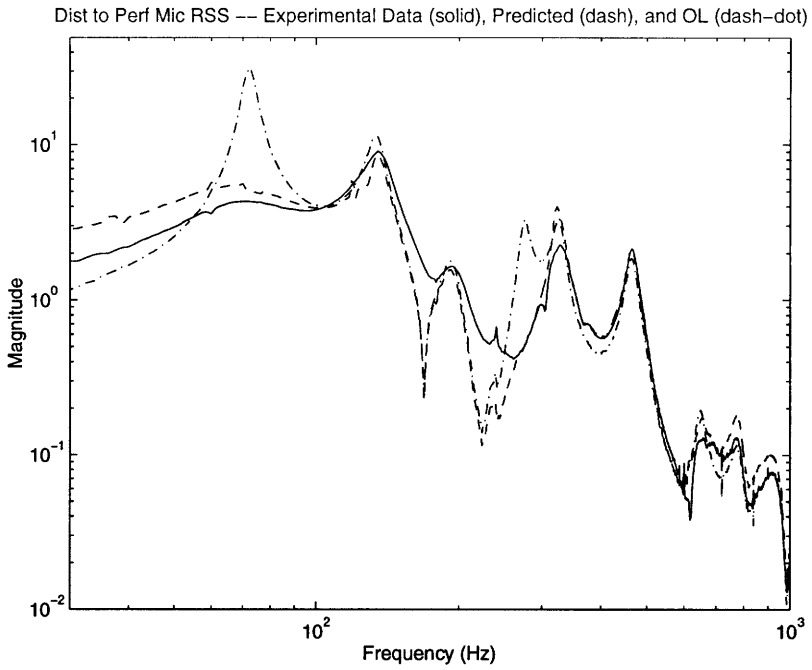

Figure 6.8: Disturbance speaker to performance microphone RSS transfer functions with the transmission control closed -- experimental closed loop data (—), predicted closed loop (--), and open loop data (-·)

control in which attenuation is achieved at certain points at the cost of amplification at all other points.

Another important point to emphasize is that while the goal of the transmission control was to reduce the spatially averaged sound levels within the lower chamber, the control only had information on the vibration of the plate. Therefore, the addition of damping to or the stiffening of the plate were the only available control options. During the control design process, the predicted closed loop performance, obtained by wrapping the compensator around the open loop data augmented by the padé time delay was plotted. The predicted closed loop performance is given by

$$G_{zw(cl)} = \frac{G_{zw(ol)}}{1 + KG_{yu(ol)}} \tag{6.1}$$

where K is the compensator. Figure 6.8 shows the predicted closed loop acoustic perfor-

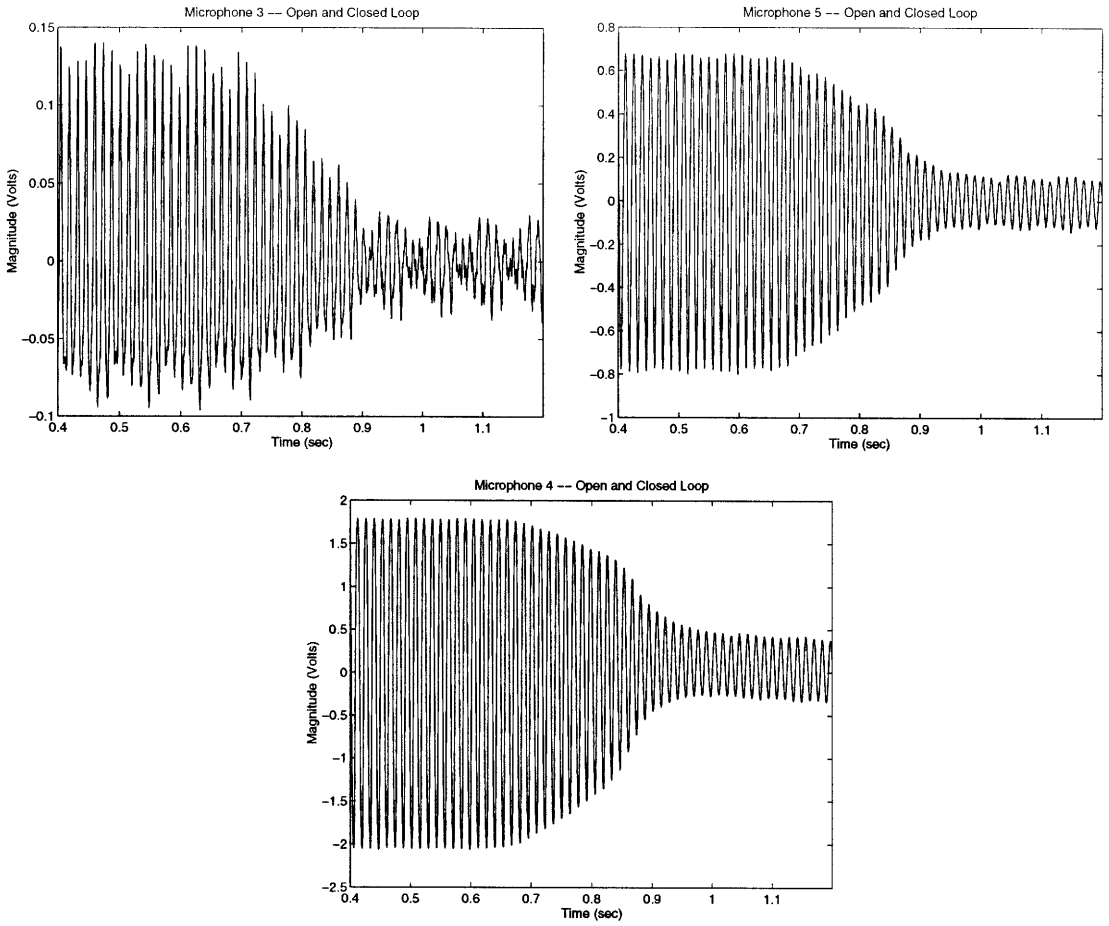

Figure 6.9: Time traces of the performance microphones in response to a sinusoidal disturbance at the frequency of the first structural mode

mance, compared with the experimentally obtained closed loop transfer function from the disturbance speaker to the root sum square of the performance microphones. Note that the predicted closed loop transfer function and the experimental closed loop transfer function match fairly well at the frequencies of the targeted structural modes, with the experimental data achieving better performance at the fundamental structural mode, but the experimental data shows amplification at some frequencies between the 100 Hz and 230 Hz.

The plots in figure 6.9 show the time traces of the three performance microphones in response to a sinusoidal disturbance at the frequency of the first structural mode, 73 Hz. Notice the significant decrease in the acoustic amplitude resulting at that frequency.

In addition to the narrowband compensator in which two specific modes of the plate were targeted for control, an attempt was made to design a broadband compensator in which attenuation at all frequencies below 300 Hz was achieved. An LQG control design, similar in structure to the narrowband compensator was used. This time, however, the state penalty matrix had more than just the two components corresponding to first two modes.

The initial problem which was encountered was that the controller did not roll off fast enough leading to gain destabilization at high frequencies. A frequency weighting on the control penalty was adopted, with a high penalty at high frequencies and a low penalty at low frequencies. The goal of the control frequency weighting was to maintain the closed loop performance improvements at low frequencies while forcing the controller to roll off at higher frequencies allowing for a stable closed loop system.

The ideal control frequency weight would be a step function which would have one value at low frequencies and then step up instantaneously to a higher value for higher frequencies. This would allow the control penalty to be constant for the low frequency range in which performance improvement is desired, and then immediately raise the control penalty to force the rolloff. However, such a function cannot be put into the state space format which is necessary for implementation of the frequency weighted LQG control. Therefore, a fourth order approximation to the step function given by

$$R_4(\omega) = \frac{\omega^4 + 1 \times 10^4 \omega^2 + 6 \times 10^9}{\omega^4 + 1 \times 10^4 \omega^2 + 6 \times 10^{14}} \tag{6.2}$$

was used as the frequency dependent control penalty. Figure 6.10 shows a plot of $R_4(\omega)$ as the dotted line. Notice that the transition between the regions of low and high control penalties is very slow. The problems that this causes are two fold. First, by pushing the control penalty lower at low frequencies in an attempt to gain more performance in that region, the transition zone is also pushed down. This leads to too much control effort exerted in the

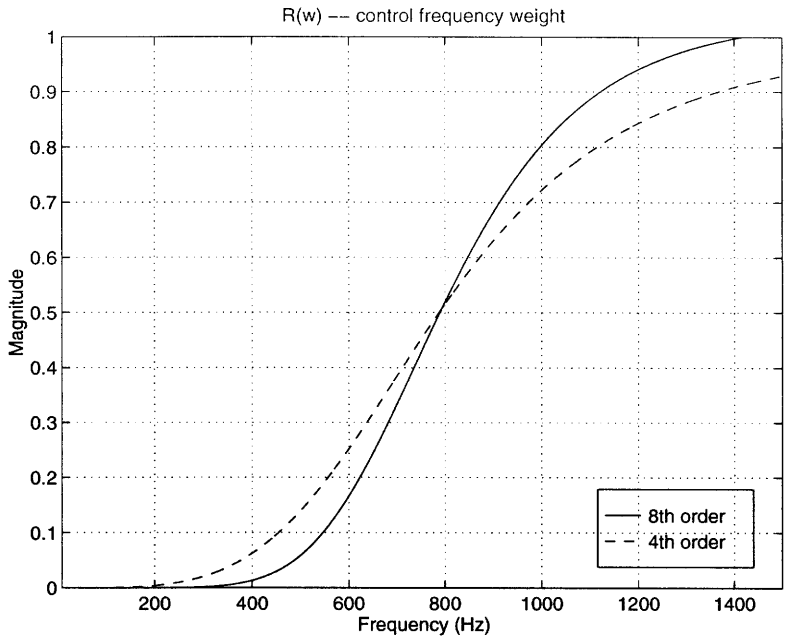

Figure 6.10: Frequency dependent control penalties

frequency range between 400 Hz and 1 kHz and gain instability results. Second, in order to have a high enough control penalty at the higher frequencies to avoid gain instability, the roll up of the weighting function must start at frequencies so low as to limit the bandwidth of the controller to below 200 Hz. Due to these limitations on the control gain, it was not possible to gain any significant performance in regions outside of the first symmetric mode, which is no better than the narrowband approach.

In an effort to shorten this transition, an eighth order approximation to the step function given by

$$R_8(\omega) = K\frac{\omega^8 - 3\times 10^3\omega^6 + 4\times 10^{12}\omega^4 - 4\times 10^{17}\omega^2 + 4\times 10^{24}}{\omega^8 - 6\times 10^5\omega^6 + 1\times 10^{15}\omega^4 + 54\omega^2 + 4\times 10^{29}} \tag{6.3}$$

was used, where K is some scaling factor. A plot of $R_8(\omega)$ with K=1 is shown in Figure 6.10 as the solid line. As can be seen, this weighting function has better transient behavior than the fourth order weighting function. Unfortunately, even with an eighth order fre-

quency weight, the transition is still too slow, resulting in the same problems. Although it is not evident in the figure, there is an order of magnitude difference in the weighting function between 70 Hz and 270 Hz, resulting in significantly less performance at the second symmetric mode than at the first. A frequency weighting function which has a rapid enough transition to allow for appreciable performance improvements in the low frequency range while maintaining gain stability will be of extremely large order.

As a result of these problems, an effective broadband controller was not able to be implemented. The broadband technique only managed to achieve performance improvements at the two symmetric modes which the narrowband controller was able to do in a much simpler control design.

6.3 Combined Transmission and Reflection Control

After the transmission controller is implemented, the behavior of the system is altered. It is upon this transmission control closed loop system that the reflection controller will be implemented. For the reflection control, the disturbance is still provided by the top speaker and the performance sensors are still microphones 3, 4, and 5. However, the control actuator is now the bottom speaker and the feedback sensor is microphone 4. So in this case, microphone 4 acts as both a feedback sensor and also as one of the performance sensors. Figure 6.11 shows the "open loop" G_{zu} transfer functions. The bottom plot is the transfer function from the control speaker to the feedback sensor, G_{yu}. All are measured with the transmission control closed.

Also, note that the open loop G_{zw} transfer functions are simply the closed loop G_{zw} transfer functions for the transmission control, shown in figure 6.7, since the disturbance in both cases is the top speaker and the performance sensors in both cases are microphones

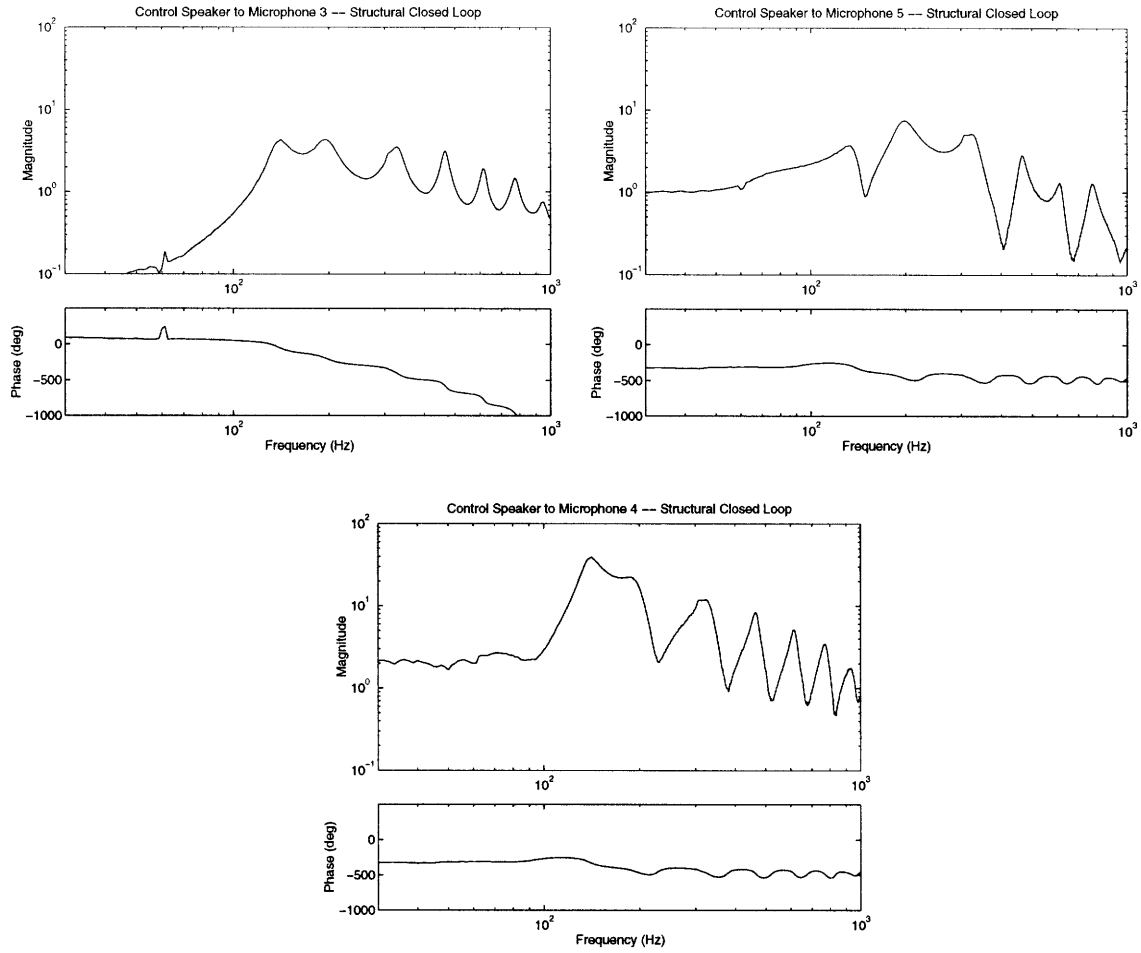

Figure 6.11: "Acoustic open loop" G_{yu} and G_{zu} transfer functions

3, 4, and 5. Also, since the feedback sensor for the acoustic control is microphone 4, the open loop G_{yw} transfer function is also included in the transmission control closed loop disturbance to performance transfer functions.

6.3.1 Acoustic Impedance Matching Controller

Two types of reflection controllers were designed, an SWLQG controller and an acoustic impedance matching controller. The impedance matching controller was designed using the methodology described in Chapter 5 and was implemented using a second HEURIKON digital computer operating at a sampling frequency of 9.6 kHz.

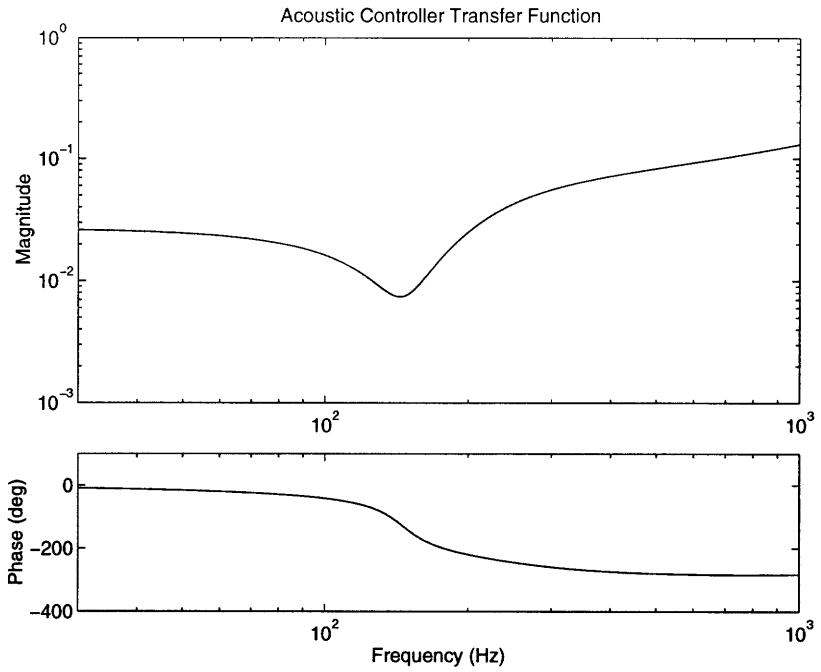

Figure 6.12: Impedance matching acoustic controller transfer function

Figure 6.12 shows the compensator transfer function, G_{uy}, for the acoustic impedance matching controller. This compensator was designed to attenuate the first few acoustic modes by employing a broadband penalty. This was done by shaping the disturbance frequency weighting to have a relatively high value up to about 400 Hz after which it rolls off. The effect of this frequency weighting is to make the control algorithm think there are higher amplitude disturbances at lower frequencies and therefore increase the control effort in that frequency range.

Figure 6.13 shows the experimental effects of the reflection control by comparing the result of implementing both the transmission and reflection control with the result of implementing just the transmission control. Note that the acoustic controller achieves attenuation in the first, second, and third acoustic modes which are at 134 Hz, 325 Hz, and 464 Hz, respectively. In addition, there is damping of the acoustics at the frequency of the speaker mode at 186 Hz.

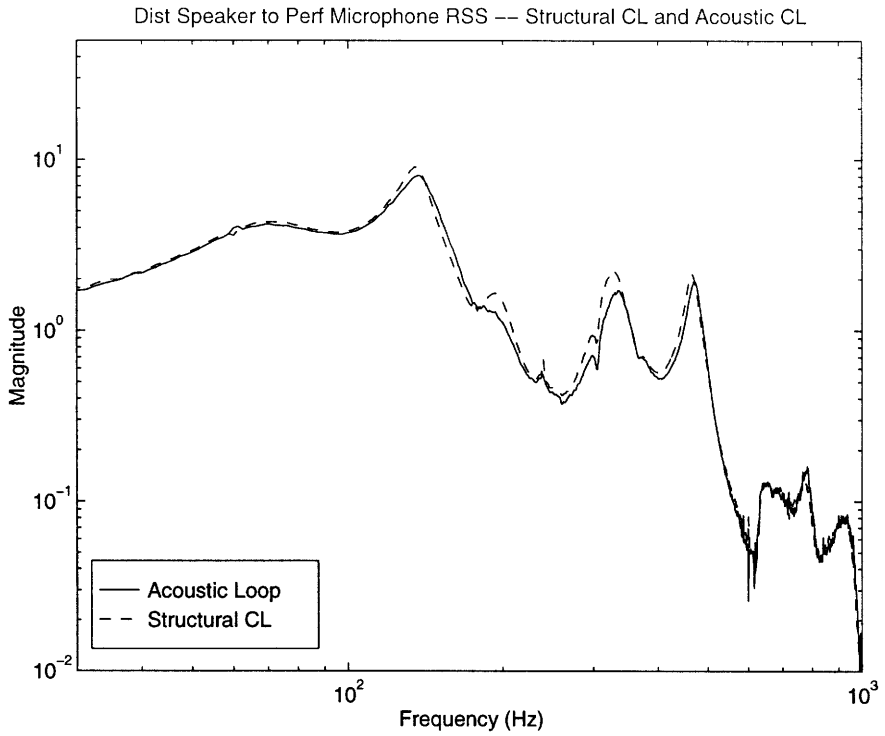

Figure 6.13: Disturbance speaker to performance microphone RSS transfer functions: impedance matching reflection and transmission closed loop (—) compared with the transmission closed loop only (--)

Figure 6.14 shows the experimental data of the transmission and reflection control closed loop system compared with the open loop data. Examination of the combined performance transfer function shows significant damping of the first and second structural modes with performance improvements of 17.8 dB and 17.3 dB, respectively. Also the first four acoustic modes show performance improvements of 3.3 dB, 6.7 dB, 0.8 dB, and 3.8 dB, which lead to a broadband performance improvement of 4.9 dB between 10 Hz and 1 kHz.

6.3.2 Sensitivity Weighted LQG Controller

The primary advantage provided by the impedance matching control design is the lack of need for a high order, reverberant model of the system. It reduces the acoustic reverbera-

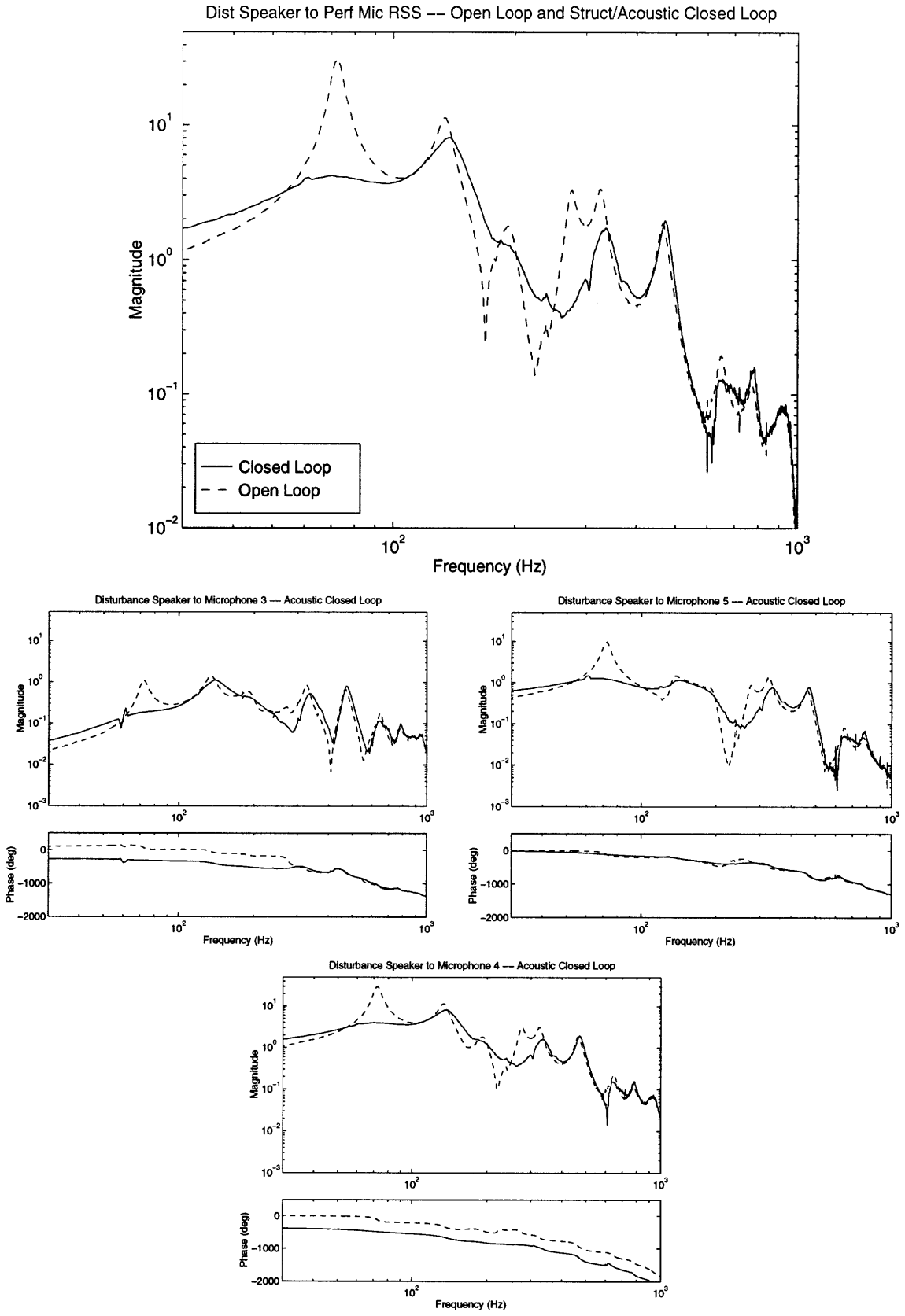

Figure 6.14: Disturbance speaker to performance microphones for impedance matching reflection control and transmission control compared with open loop

tion inside the fairing enclosure with a model of the fairing structure and its local acoustic coupling, without knowledge of the acoustic cavity modes. This allows for the reconfiguration of the payload inside the fairing, which alters the acoustic modes of the enclosure, without the need to remodel the entire system. However, this convenience comes at the price of reduced closed loop performance. It is intuitive that if information on the entire system including its structural modes, acoustic modes, and the coupling between the structure and acoustics is provided, as opposed to just the structural modes and its local acoustic coupling, the controller will be better able to control the acoustic behavior of the enclosure.

The SWLQG controller was designed based on a 42 state model, but the digital computer is only capable or running a 42 state compensator at a prohibitively slow sampling rate. Recalling that the phase loss associated with the digital implementation of the controller is worsened by slower sampling rates, it is imperative that the computer be run with as high a sampling rate as possible. A sampling rate of 8.6 kHz was found to be fast enough so that the subsequent phase loss does not limit the bandwidth of the controller to below the highest frequency of interest. However, this requires that the controller must be reduced from 42 states to 16 states. This reduction leads to a loss of important compensator dynamics near the frequency of the fundamental acoustic mode, leading to a reduction in the closed loop performance at that mode. Since the fundamental acoustic mode has the highest magnitude of any of the acoustic modes, its reduction is the most important in the overall closed loop performance. Therefore, an attempt was made to reduce the compensator while maintaining its dynamics at that mode. The problem is that the mode in question has low amplitude and observability compared to the other modes of the controller, and therefore a reduction by balanced realization promptly eliminates that mode. Using the balanced reduction, the compensator can only be reduced to 38 states before the mode is

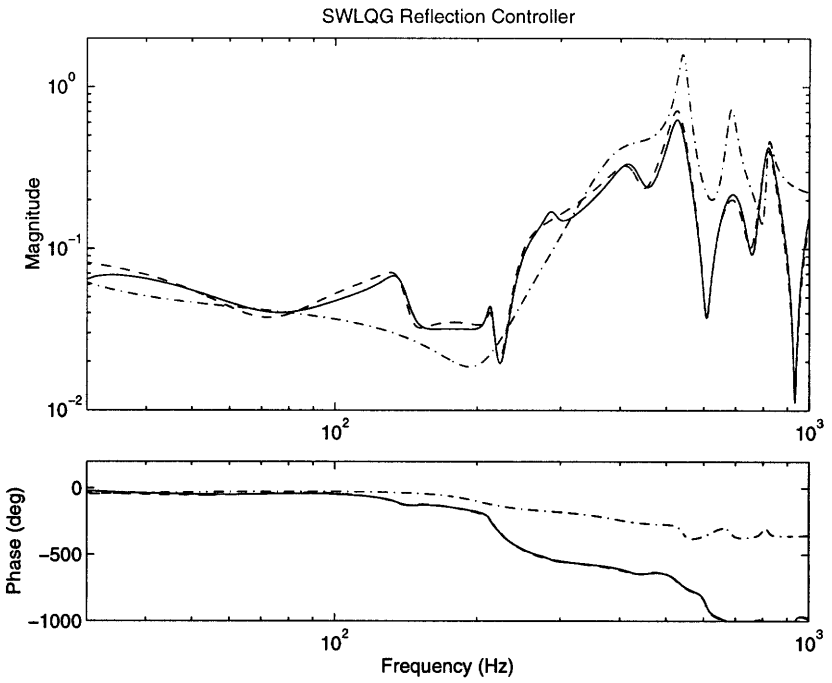

Figure 6.15: SWLQG reflection controllers: full 42 state compensator (—), 22 state reduced compensator (- -), and 16 state reduced compensator (-·)

eliminated. Thus, a reduction method in which specified modes can be kept while others are eliminated is needed. One such method is to identify the compensator using the FORSE algorithm that was used to obtain measurement models, and then to eliminate unnecessary dynamics using the "Remove poles from model" option. This was done and the compensator was reduced to 22 states. Further reduction led to a poor match between the reduced and full compensators which would result in poor closed loop performance. The problem now is that the digital computer must be slowed down to a sampling rate of 7.8 kHz to account for the increase in number of compensator states. An analysis was performed to ensure the closed loop stability of the system after the change in sampling rate. Figure 6.15 shows the full compensator, the 22 state reduced compensator and the 16 state reduced compensator. Notice that in the 16 state controller, the pole near 130 Hz has been

reduced out, whereas the 22 state controller retains that mode. There is also a mismatch of the amplitude at higher frequencies for the 16 state compensator.

Figure 6.16 shows the closed loop transfer function from the disturbance speaker to the three performance microphones for the 16 state controller. The top plot shows the RSS of the three microphones, and the remaining plots show the responses of the individual microphones. The dashed line is the "open loop" transfer function in which only the transmission control is implemented and the solid line shows the closed loop transfer function with both the transmission and reflection controls implemented, thus showing the effects of the reflection control. Notice that damping is added to the first three acoustic modes at 134 Hz, 325 Hz, and 464 Hz, with a slight amplification of the speaker mode at 186 Hz. The performance gain resulting from the addition of the reflection control compared with the transmission control only is 4.44 dB, 9.57 dB, and 10.88 dB at the first three acoustic modes respectively. The reason for the relatively small performance improvement in the fundamental acoustic mode is due to the elimination of the critical compensator mode responsible for the attenuation of that mode.

Figure 6.17 shows the closed loop transfer function from the disturbance speaker to the three performance microphones for the combined reflection and transmission control compared to the open loop transfer functions. The top plot shows the RSS of the three microphones and the remaining three plots show the individual microphones. Significant damping has been added to the first five modes of the system by the combination of the transmission and reflection controls. The broadband performance improvement measured from 10Hz to 1 kHz is 5.47 dB. The performance gains in the first two structural modes are 16.03 dB and 14.17 dB, respectively, and in the first three acoustic modes are 5.37 dB, 11.88 dB, and 11.32 dB respectively. Although there is amplification in the region of the speaker mode (near 200 Hz) caused primarily by the transmission control, the achieved

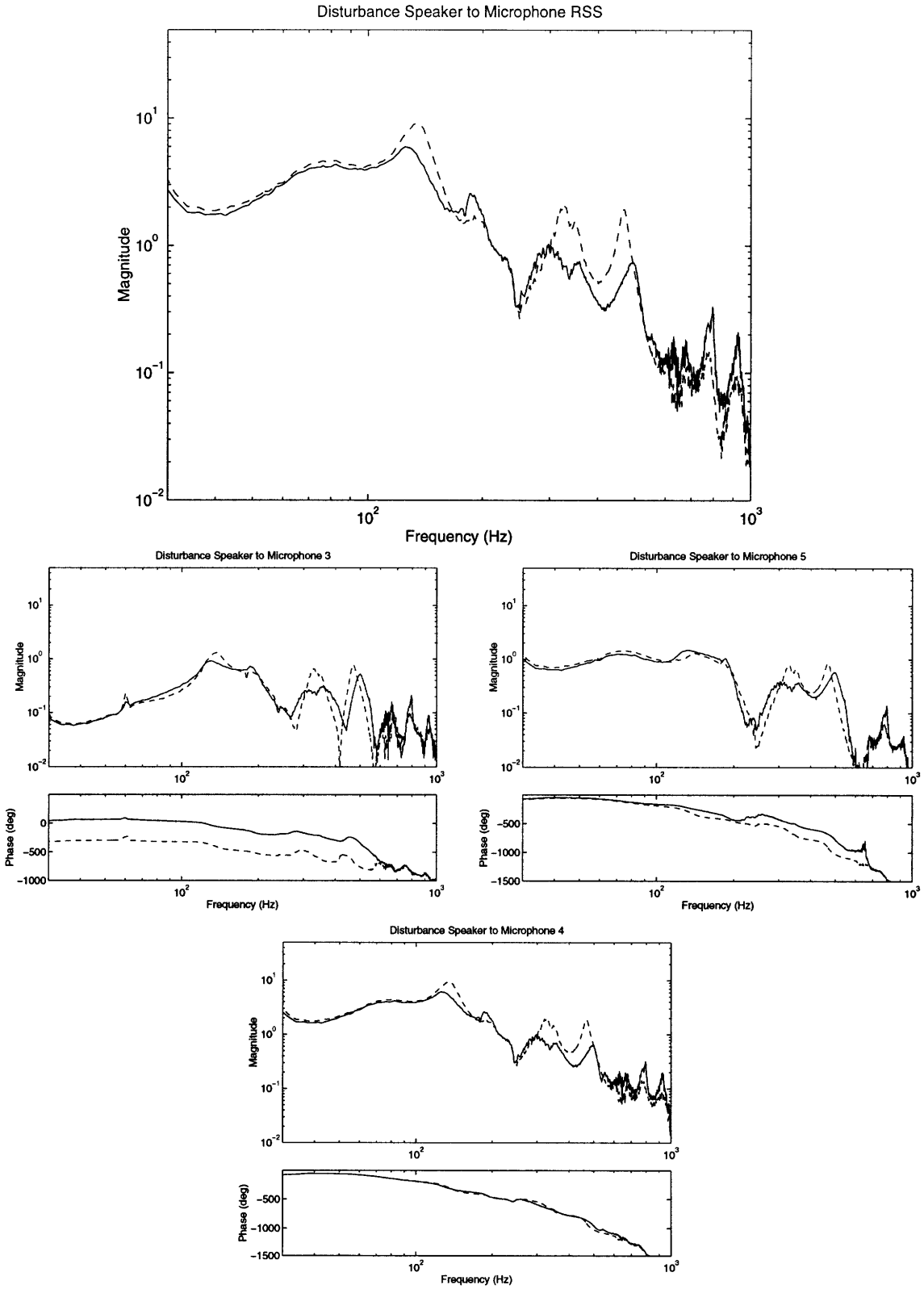

Figure 6.16: Disturbance to performance microphone transfer functions for the 16 state SWLQG reflection control with transmission control (—) compared with transmission control only (--)

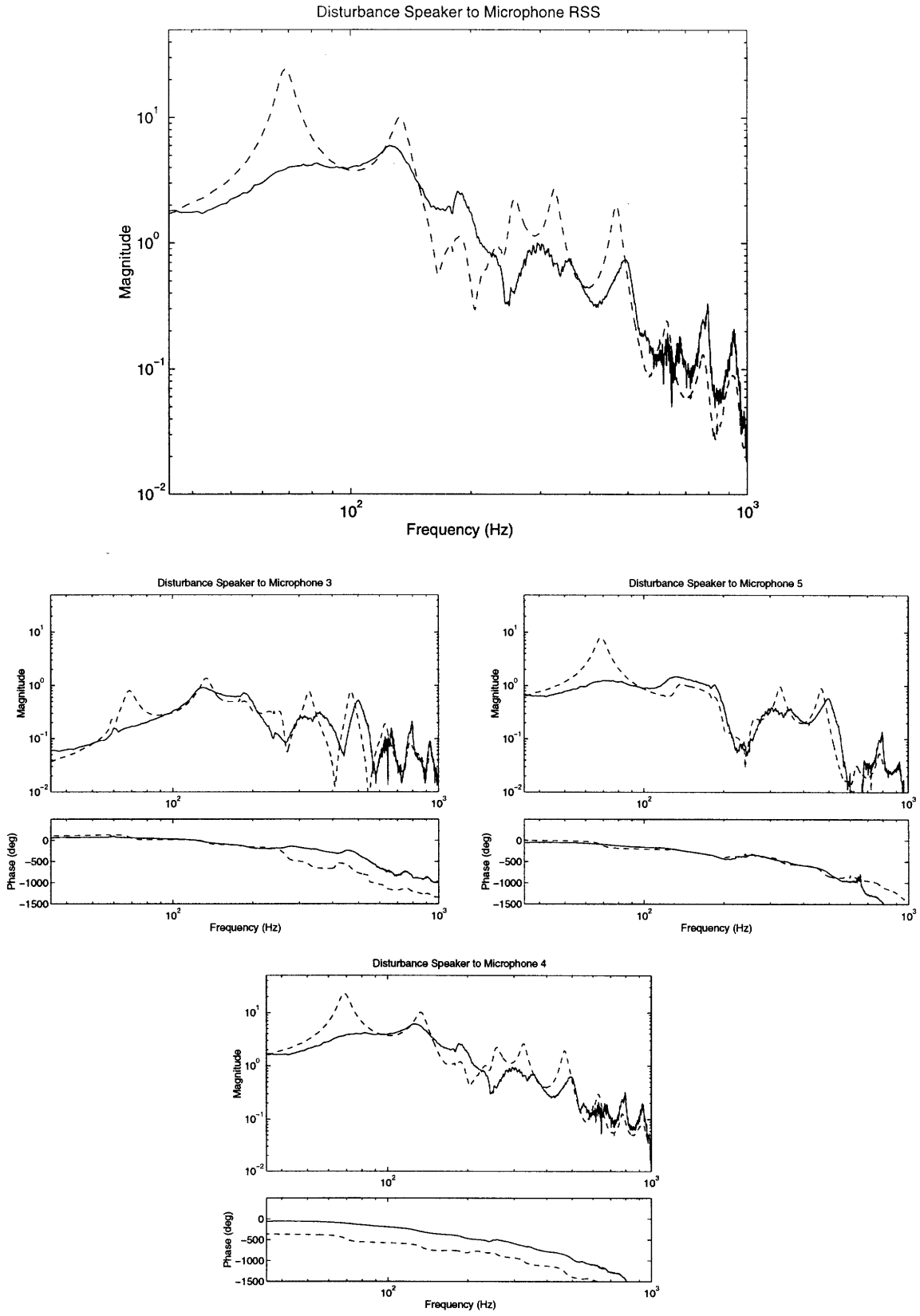

Figure 6.17: Disturbance to performance microphone transfer functions for the 16 state SWLQG reflection control with transmission control (—) compared with open loop (--)

acoustic attenuation is global in nature as can be seen from the reductions in each of the three performance microphones. One point to note is that since microphone 5 is located at the midpoint of the lower chamber where the fundamental acoustic mode has a node, it is not observable in the transfer function from the disturbance to microphone 5.

While the 16 state controller achieved very good performance, the 22 state controller should be able to achieve even better results since it retains more of the dynamics of the full compensator. Figure 6.18 shows the closed loop disturbance speaker to performance microphone transfer functions for the 22 state controller. The top plot shows the microphone RSS transfer function and the remaining plots show the individual microphones. The solid line shows the closed loop system with both the transmission and reflection compensators implemented, and the dashed line shows the system with just the transmission control implemented. Again, acoustic attenuation is achieved in the first three acoustic modes, and is global in nature. Notice that the damping at the first acoustic mode is better with the 22 state compensator compared to the 16 state compensator, although there is amplification just above the fundamental acoustic mode. This amplification also appeared in the predicted closed loop transfer function with the full 42 state compensator, although to a slightly lesser degree. Figure 6.19 shows the closed loop experimental data of the disturbance speaker to performance microphone RSS transfer functions for the 22 state and 16 state compensators compared to the predicted closed loop RSS performance transfer function for the full 42 state compensator. The reason the amplification does not occur with the 16 state compensator is probably due to the considerably lower magnitude of the 16 state compensator transfer function near 200 Hz when compared with the full and 22 state compensators. This lower magnitude results in no amplification near 200 Hz, but also leads to less performance at the fundamental acoustic mode. This is consistent with the slightly higher amplification caused by the 22 state compensator compared with

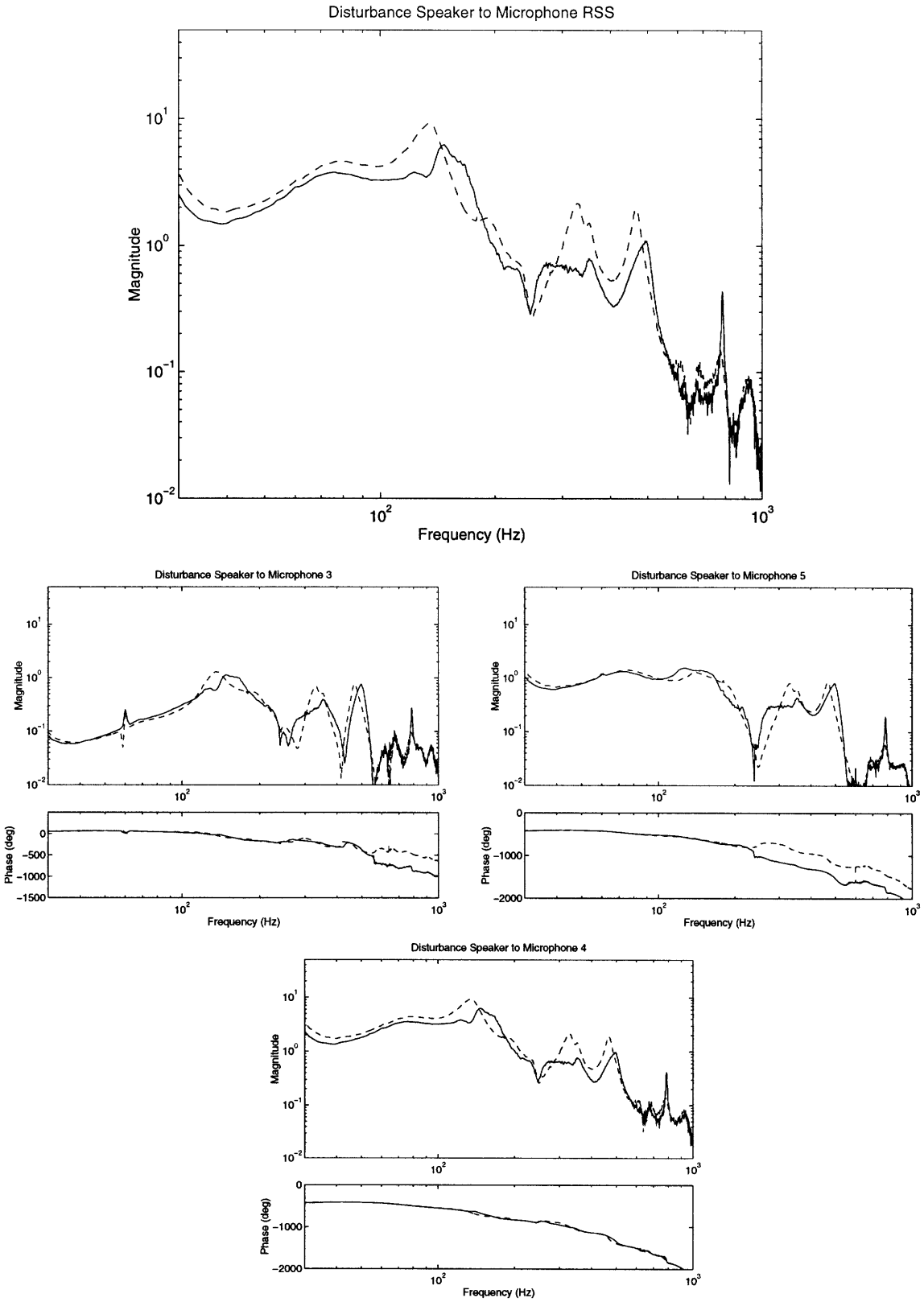

Figure 6.18: Disturbance to performance microphone transfer functions for the 22 state SWLQG reflection control with transmission control (—) compared with transmission control only (--)

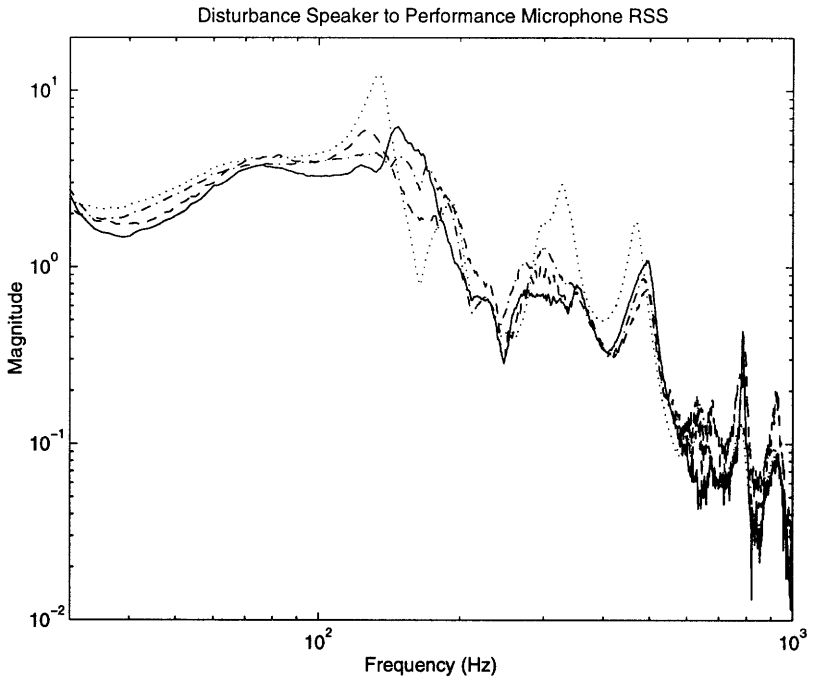

Figure 6.19: Disturbance speaker to performance microphone RSS transfer functions -- experimental data for 22 state reflection controller (—), experimental data for 16 state reflection controller (--), predicted performance for 42 state reflection controller(-·), and experimental data with no reflection control implemented (···)

the full compensator since the reduction to 22 states caused a slight increase in the amplitude of the compensator near 200 Hz. Clearly there is a trade-off between achieved closed loop performance at the fundamental acoustic mode and amplification just above that mode. The performance improvements from implementing the 22 state reflection control are 8.31 dB, 10.28 dB, 7.58 dB at the first three acoustic modes.

Figure 6.20 shows the disturbance speaker to performance microphone transfer function for the system with both the 22 state reflection control and the transmission control implemented, compared to the open loop data. Again, the first three acoustic cavity modes as well as the acoustics associated with the first two symmetric plate modes are very well damped. There is amplification in the region near 200 Hz, but the achieved attenuation is observed at all three performance microphones. The combined transmission and reflection

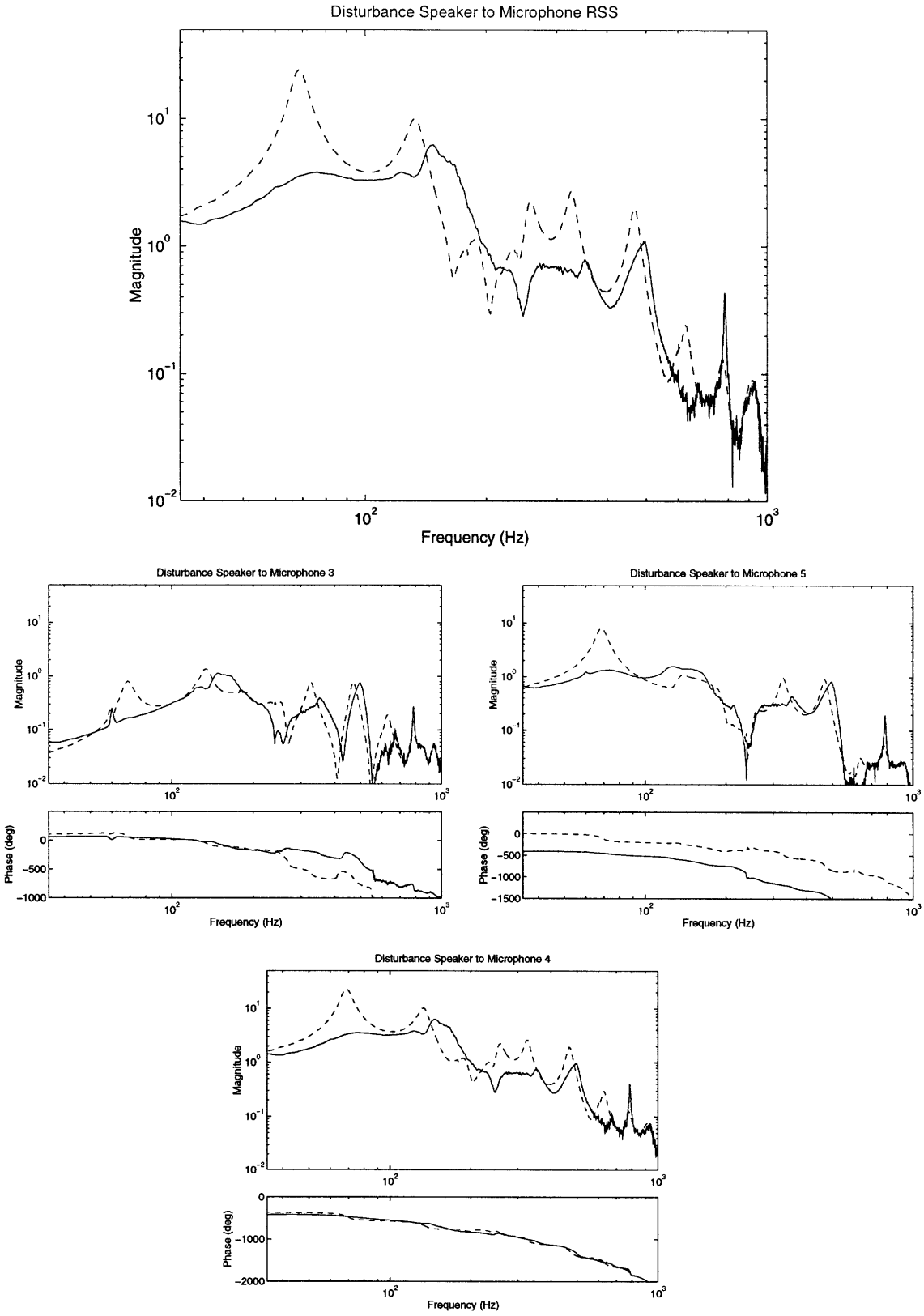

Figure 6.20: Disturbance to performance microphone transfer functions for 22 state SWLQG reflection control with transmission control (—) compared with open loop (--)

control results in a broadband performance improvement of 5.61 dB. The performance gains at the first three acoustic modes are 9.23 dB, 12.59 dB, and 8.02 dB respectively, while the gains at the two plate modes are 11.81 dB and 16.82 dB. Notice that the performance at the first acoustic mode is significantly better with the 22 state controller.

6.4 Summary

The experimental results of both the transmission control and the combined transmission and reflection control have been presented. The performance improvements are summarized in tables 6.1 and 6.2. Table 6.1 shows the results of the transmission control and the impedance matching reflection control and table 6.2 shows the results of the transmission control and the SWLQG reflection control for both the 16 state compensator and the 22 state compensator. One important point to note is the difference in performance of the transmission control for the impedance matching and the SWLQG reflection compensators. The reason for this is that between the implementation of the impedance match and the SWLQG controllers, the acoustic chamber was disassembled to fix a faulty performance microphone and subsequently reassembled. This altered the dynamic properties of the chamber, which is evidenced by the shifting of the modal frequencies. This variation in the modes was large enough to warrant a redesign of the transmission controller. Due to limitations on time, the second transmission controller was not able to be designed to meet the performance achieved by the first transmission controller which was used for the impedance match. However, the important point here is that it is possible to achieve a broadband performance improvement of 4.56 dB with the transmission control and an additional 2.29 dB with the 22 state SWLQG reflection control. Although this combination was not implemented experimentally due to the limitations on time, a potential broadband performance gain of 6.85 dB is possible.

Table 6.1: Closed loop performance for impedance matching reflection control

Mode	Freq (Hz)	Transmission Control	Impedance Match Reflection & Transmission
Broadband	10Hz - 1kHz	4.56 dB	4.92 dB
1st Structural	73 Hz	17.37 dB	17.76 dB
2nd Structural	276 Hz	16.15 dB	17.32 dB
1st Acoustic	134 Hz	2.16 dB	3.27 dB
2nd Acoustic	325 Hz	3.62 dB	6.70 dB
3rd Acoustic	464 Hz	-1.12 dB	0.80 dB

Table 6.2: Closed loop performance for SWLQG reflection control

Mode	Freq (Hz)	Transmission Control	16 state Reflection & Transmission	22 state Reflection & Transmission
Broadband	10Hz - 1kHz	3.32 dB	5.47 dB	5.61 dB
1st Structural	69 Hz	15.43 dB	16.03 dB	16.82 dB
2nd Structural	260 Hz	16.03 dB	14.17 dB	11.81 dB
1st Acoustic	133 Hz	0.92 dB	5.37 dB	9.23 dB
2nd Acoustic	326 Hz	2.31 dB	11.88 dB	12.59 dB
3rd Acoustic	466 Hz	0.44 dB	11.32 dB	8.02 dB

Chapter 7

Conclusions

7.1 Summary

The problem of vibro-acoustic control for application in acoustic attenuation of launch vehicle shrouds was investigated. The complex problem which involves the curvilinear two dimensional structure of the fairing shell enclosing a three dimensional acoustic field was simplified into a two dimensional structure and one dimensional acoustics in a waveguide. The simplification of the problem led to the elimination of many of the difficulties posed by a large order, multi-dimensional setup while preserving the relevant physics of the problem.

Since most of the acoustic disturbances originate from outside the payload fairing, it is reasonable to think that reducing the transmission of sound through the shroud will lead to significant attenuation of the interior acoustics. The addition of structural damping to the fairing did in fact reduce the transmission of sound into the enclosure, but due to the weak coupling between the structural modes and the acoustic cavity modes, it was not possible to attenuate the acoustic reverberation with structural damping alone. It was necessary to supplement the transmission control with another controller in which a second actuator

was used to alter the acoustic reflection coefficient at one end of the waveguide. Using the method of successive loop closure, both the transmission control and the reflection control were implemented and it was possible to achieve significant reductions in the interior acoustics at the first three acoustic cavity modes as well as at frequencies corresponding to the first two symmetric structural modes.

The transmission control utilized only structural sensors and actuators employing a PVDF strain sensor and a piezoceramic actuator. A sensitivity weighted LQG control targeting the first and second symmetric modes of the plate was used, achieving significant damping of those modes as well as small performance improvements in the first, second, and fourth acoustic modes. The closed loop system achieved a broadband performance improvement of 4.56 dB with improvements of 17.37 dB and 16.15 dB at the two structural modes.

The reflection control, using a speaker actuator and a microphone sensor, attenuated the reverberation of sound within the enclosure by reducing the reflection coefficient at one end of the waveguide. Two different types of controllers were implemented: a sensitivity weighted LQG design and an acoustic impedance matching design, both targeting the first three acoustic modes. The reflection control provided additional damping to the first, second, and third acoustic modes. The SWLQG reflection control achieved an additional 2.29 dB broadband, with 8.31 dB, 10.28 dB, and 7.58 dB improvements at the first three acoustic modes, respectively. The impedance match was only able to achieve an additional 0.36 dB broadband with 1.11 dB, 3.08 dB, and 1.92 dB at the first three acoustic modes, but previous results using the acoustic impedance match with a very similar setup [17] show that better results are possible.

In achieving this final result, numerous difficulties were encountered. The use of various structural sensors for the transmission control were investigated with problems arising

from each choice. In the end, the PVDF strain sensor was specially designed for the plate, leading to good closed loop results. However, the transmission control failed to add any significant damping to the acoustic cavity modes, forcing the need for a supplementary reflection control. A multi-input, multi-output control design seemed the most natural choice, but it quickly became clear that the modeling problems caused by the large number of inputs and outputs would eliminate this as a potential solution. Therefore the method of successive loop closure was used in which two single-input, single-output controllers were implemented.

7.2 Recommendations for Further Work

In the implementation of active control for attenuation of acoustic levels inside a rocket payload fairing, it is desirable to use as little additional mass as possible. In that respect, a control design which only requires actuators and sensors on the structure of the fairing which can simultaneously control the transmission and reflection of acoustics is better than a design which uses two sets of actuators and sensors. The reduction of acoustic transmission is accomplished by damping the dynamic vibrations of the plate so that incoming acoustic disturbances reflect back into the outside environment. However, by simply damping the structural vibrations of the fairing the acoustic reverberation within the enclosure cannot be controlled due to the weak coupling between the structural modes and the acoustic cavity modes. Also, if the structure is controlled to minimize the acoustic reflection coefficient in order to attenuate the reverberation within the enclosure, it is difficult to control the transmission of sound into the enclosure from the outside environment.

Also, the actual launch vehicle shroud encloses a three dimensional acoustic environment with a structure that is significantly more complex than the circular plate used in this experiment. The increased complexity of the problem raises the issue of the selection and

placement of the sensors and actuators to effectively control the structural modes responsible for the transmission of sound as well as the acoustic cavity modes which contribute the most to the performance. An analysis to determine these modes must be done and the proper actuators and sensors selected.

The impedance matching technique should be capable of achieving significantly better results than was shown in this experiment. This is evident in the past implementation of the technique on structural systems [31,32]. The problem may lie in the choice of sensors and actuators, or more fundamentally in the formulation of the power flow control problem. The main advantage provided by the impedance matching method is the need for only a low order model which includes the dynamics of the structure and its local acoustic coupling. This allows for reconfiguration of the payload without having to remodel the system, whereas with the SWLQG approach, every reconfiguration of the payload requires a model update and a control redesign. Therefore, an impedance matching controller which can achieve performance comparable to the SWLQG controller would be a significant improvement.

References

[1] Eldred, K., "Acoustic Loads Generated by the Propulsion System," Tech. Rep. NASA SP-8072, NASA, 1971

[2] Weissman, K., M. E. McNelis, and W. D. Pordan, "Implementation of Acoustic Blankets in Energy Analysis Methods with Application to the Atlas Payload Fairing," *Journal of the IES*, July/August 1994, pp. 32-39.

[3] Lee, Y. A., "Study of Helium Effect on Spacecraft Random Vibration with VAPEPS Program," *Proceedings, 59th Shock and Vibration Symposium*, Albuquerque, NM, Oct. 1998, pp. 119-135.

[4] Lee, Y. A. and W. Henricks, "High Level Acoustic Noise Reduction with Helium in Shroud," *Journal of the IES*, 1990, pp. 539-543.

[5] Nelson, P., A. Curtis, S. Elliott, and A. Bullmore, "The Minimum Power Output of Free Field Point Sources and the Active Control of Sound," *Journal of Sound and Vibration*, Vol. 116, No. 3, 1987, pp. 397-414.

[6] Nelson, P., A. Curtis, S. Elliott, and A. Bullmore, "The Active Minimization of Harmonic Enclosed Sound Fields, Part II: A Computer Simulation,' *Journal of Sound and Vibration*, Vol. 117, No. 1, 1987, pp. 15-33.

[7] Nelson, P., A. Curtis, S. Elliott, and A. Bullmore, "The Active Minimization of Harmonic Enclosed Sound Fields, Part I: Theory,' Journal of Sound and Vibration, Vol. 117, No. 1, 1987, pp. 1-13.

[8] Elliot, S. J., I. Stothers, P. A. Nelson, A. M. McDonald, D. C. Quinn, and T. Saunders, "The Active Control of Engine Noise Inside Cars," *Proceedings, Inter-Noise 88*, 1988, pp. 971-974

[9] Elliot, S. J., P. A. Nelson, I. Stothers, and C. C. Boucher, "In-flight Experiments on the Active Control of Propeller-induced Cabin Noise," *Journal of Sound and Vibration*, Vol. 140, No. 2, 1990, pp. 219-238.

[10] Fuller, C. R. and J. D. Jones, "Experiments on Reduction of Propeller Induced Interior Noise by Active Control of Cylinder Vibration," *Journal of Sound and Vibration*, Vol. 112, No. 2, 1987, pp. 389-395.

[11] Fuller, C. and C. Hansen, "Active Control of Interior Noise in Model Aircraft Fuselages Using Piezoceramic Actuators," Proceedings, *13th AIAA Aeroacoustics Conference*, 90. AIAA 90-3922

[12] Baumann, W. T., F.-S. Ho, and H. H. Robertshaw, "Active Structural Acoustic Control of Broadband Disturbances," *The Journal of the Acoustical Society of America*, Vol. 92, No. 4, 1992, pp. 1998-2005.

[13] Koshigoe, S., J. Gillis, and E. Falangas, "A New Approach for Active Control of Sound Transmission Through an Elastic Plate Backed by a Rectangular Cavity," *The Journal of the Acoustical Society of America*, Vol. 94, No. 2, Aug. 1993, pp. 900-907.

[14] Fuller, C. R. and G. P. Gibbs, "Active Control of Interior Noise in a Business Jet Using Piezoceramic Actuators," *Proceedings, Noise-Con 94*, Ft. Lauderdale, FL, May 1994, pp. 389-394.

[15] Koshigoe, S., A. Teagle, and A. Gordon, "A time domain study of active control of sound transmission due to acoustic pulse excitation," *Journal of Sound and Vibration*, Vol. 97, No. 1, Jan. 1995, pp. 313-323.

[16] Guicking, D., K. Karcher, and M. Rollwage, "Active Control of the Acoustic Reflection Coefficient at Low Frequencies," *Proceedings, Inter-Noise*, 1983, pp. 419-422

[17] Glaese, R. M., *Impedance Matching for Structural-Acoustic Control*, PhD thesis, Department of Aeronautics and Astronautics, M.I.T., Cambridge, MA, April 1997.

[18] Balachandran, B., A. Sampath, and J. Park, "Active control of interior noise in a three-dimensional enclosure," *Smart Materials and Structures*, Vol. 5, 1996, pp. 89-97.

[19] Denoyer, K. K., S. F. Griffin, and D. Sciulli, *Hybrid structural/acoustic control of a sub-scale payload fairing*, Air Force Research Laboratory, 1998

[20] Jacques, R. N. and D. W. Miller, "Multivariable Model Identification from Frequency Domain Data," *IEEE Conference on Decision and Control*, 1994.

[21] Liu, K., "Identification of Multi-Input and Multi-Output Systems by Observability Range Space Extraction," *Proceedings, 31st IEEE Conference on Decision and Control*, Tucson, AZ, Dec. 1992.

[22] Moré, J., "The Levenberg-Marquardt Algorithm: Implementation and Theory," in *Lecture Notes in Mathematics 630: Numerical Analysis* (Watson, G., ed.), Springer-Verlag, 1977.

[23] Grocott, S., *Comparison of Control Techniques for Robust Performance on Uncertain Structural Systems*, MS thesis, Department of Aeronautics and Astronautics, M.I.T., Cambridge, MA, Jan. 1994.

[24] Gupta, N. K., "Frequency-Shaped Cost Functionals: Extension of Linear-Quadratic-Gaussian Design Methods," *Journal of Guidance and Control*, Vol. 3, No. 6, Nov. - Dec. 1980, pp. 529-535.

[25] Currey, M. N. and K. A. Cunefare, "The radiation modes of baffled finite plates," *Journal of the Acoustical Society of America*, Vol. 98, No. 3, 1995, pp. 1570-1580.

[26] Elliott, S. J. and M. E. Johnson, "Radiation modes and the active control of sound power," *Journal of the Acoustical Society of America*, Vol. 94, No. 4, Oct. 1993, pp. 2194-2204.

[27] Lee, M. R. and R. Singh, "Analytical formulations for annular disk sound radiation using structural modes," *Journal of the Acoustical Society of America*, Vol. 95, No. 6, 1994, pp. 3311-3323.

[28] Hansen, C. H. and D. A. Bies, "Near Field Determination of the Complex Radiation Efficiency and Acoustic Intensity Distribution for a Resonantly Vibrating Surface,"

Journal of Sound and Vibration, Vol. 62, No. 1, Jan. 1979, pp. 93-110.

[29] Krishnappa, G. and J. M. McDougall, "Sound Intensity Distribution and Energy Flow in the Nearfield of a Clamped Circular Plate," *Transactions of the ASME, Journal of Vibration, Acoustics, Stress, and Reliability in Design*, Vol. 111, No. 4, Oct. 1989, pp. 465-471.

[30] Blaurock, C. "PVDF Modal Accentuation Sensor," 1998

[31] Miller, D. W., S. R. Hall, and A. H. von Flotow, "Optimal Control of Power Flow at Structural Junctions," *Journal of Sound and Vibration*, Vol 140, No. 3, 1990, pp. 475-497

[32] Miller, D. W. and S. R. Hall, "Experimental Results Using Active Control of Traveling Wave Power Flow," *Journal of Guidance, Control, and Dynamics*, Vol. 14, No. 2, Mar.-Apr. 1991, pp. 350-359.

Appendix A

MATLAB Code for Design of SWLQG Compensators

```
% SWLQG control of acoustic transmission through a plate using
% strain (inner PVDF) feedback
% Design of SWLQG controller for reflection control is similar

clear

PTH=path;
path('/mace/roger/Typsec/Acoustic/1D',PTH);
path('/mace/mace/matlab',PTH);

i=sqrt(-1);
rate=8600;  %sampling rate of stealth (Hz)

% load data (y/u) -- data does not include time delay
load ../042898d
f=FreqV; w=f*2*pi;
Datayu=Xfer34;    %piezo to Inner PVDF
Datayu=Datayu.*exp(-i*w*1.5/rate);

% load data (z/w)
load ../042898b
Datazw=Xfer34;    %speaker to Inner PVDF
Datazw=Datazw.*exp(-i*w*1.5/rate);

% load acoustic performance data
load ../042898a
DataRSS=sqrt(Xfer14.^2 + Xfer24.^2 + Xfer34.^2);
DataRSS=DataRSS.*exp(-i*w*1.5/rate);

% load model (y/w,u) -- u=piezo, w=speaker, y=accel
```

```
load pmodelbfca40
sys=com2real(sys);
[A,B,C,D]=unpck(sys);
A=full(A); B=full(B); C=full(C); D=full(D);
[At,Bt,Ct,Dt]=pade(1.5/rate,2);
[A,B,C,D]=seriesa(At,Bt,Ct,Dt,A,B,C,D,1);
states=length(A);

Sc=[A B; C D]; Nc=[length(A) 1 1];
[Sc,Nc]=balred(2,Sc,Nc);
[A,B,C,D]=split(Sc,Nc);
[A,B,C]=ss2mod6(A,B,C);
Bu=B(:,1); Du=D(:,1);
Bw=B(:,2); Dw=D(:,2);

rho=8e-7;
th=1e-2;

Cz=zeros(1,length(C));
Cz(6)=1.2;
Cz(18)=.3;

% Find frequencies of all modes
modes=length(A)/2;
for i=1:modes
 A1=A(i*2-1,i*2-1); A2=A(i*2-1,i*2);
 omw(i)=sqrt(A1^2+A2^2);   % in rad/sec
 zt(i)=-A1/sqrt(A1^2+A2^2);
end
om=omw/2/pi;   % in Hz

% transforms the Cz matrix to real modal coordinates
T=zeros(modes*2,modes*2);
for i=1:modes
  wd=omw(i)*sqrt(1-zt(i)^2);
  if i==modes
    wd=0.5;
  end
  Tb=[1/wd 0; -zt(i)*omw(i)/wd 1];
  T(2*i-1:2*i,2*i-1:2*i)=Tb;
end
Cz=Cz*T;

Ainv=inv(A);
AinvT=Ainv';

% Construct the SWLQG state weighting matrix
Rxx=Cz'*Cz;
Vxx=Bw*Bw';
```

```
% Sensitivity weighting ---------------------------------------
% index of desired modes into om and zt vectors
ind=[10 11 12 13 14 15 16 17 18 19];
% Zeta (0) or omega (1) uncertainty?
%
typ=[0 0 0 0 0 0 0 0 0 0];
% Sensitivity state weighting matrix
%
Raa=[10 10 10 10 10 10 20 20 10 10];
nparam=length(ind);

for i=1:nparam
 fr(i)=om(ind(i));% freq of uncertain modes
 z(i)=zt(ind(i));% damping ratios of uncertain modes
end

for i=1:nparam
 Ab=A(ind(i)*2-1:ind(i)*2, ind(i)*2-1:ind(i)*2);% Block of A matrix
 Ainvb=inv(Ab);
 AinvTb=Ainvb';
 if typ(i)==0
  dAdz=[-fr(i) z(i)*fr(i)/sqrt(1-z(i)^2); -z(i)*fr(i)/sqrt(1-z(i)^2) -fr(i)];
  dRxxb=Raa(i)*dAdz'*AinvTb*Ainvb*dAdz;
 elseif typ(i)==1
  dAdw=[-z(i) sqrt(1-z(i)^2); -sqrt(1-z(i)^2) -z(i)];
  dRxxb=Raa(i)*dAdw'*AinvTb*Ainvb*dAdw;
 end
 dRxx=zeros(2*modes,2*modes);
 dRxx(ind(i)*2-1:ind(i)*2, ind(i)*2-1:ind(i)*2)=dRxxb;

 Rxx=Rxx+dRxx;
end

% end sensitivity weighting -----------------------------------

[ke,se,ee]=lqe(A,Bw,C,1,th);
[kr,sr,er]=lqr(A,Bu,Rxx,rho);

Ac=A-Bu*kr-ke*C+ke*Du*kr;
Bc=ke;
Cc=kr;
Dc=0;

% 2nd order hp filter to get rid of high magnitude comp dynamics at low freq
whp=5*2*pi; zhp=.707;
nhp=[1 0 0]; dhp=[1 2*zhp*whp whp^2];
[ahp bhp chp dhp]=tf2ss(nhp,dhp);
[Ac,Bc,Cc,Dc]=series(Ac,Bc,Cc,Dc,ahp,bhp,chp,dhp);
```

```
Acomp=Ac; Bcomp=Bc; Ccomp=Cc; Dcomp=Dc;

[mc,pc]=bode(Acomp,Bcomp,Ccomp,Dcomp,1,w);
figure(1)
subplot(211), loglog(f,mc), Mlabel, grid, axis([10 2000 1e-3 1e2])
title('Compensator TF')
subplot(212), semilogx(f,pc), Plabel, grid, axis([10 2000 -500 500])

% Check for compensator stability
meig=max(real(eig(Acomp)));
disp(['Maximum real part of compensator e-vals = ',num2str(meig)]);

% Loop transfer function using model
[Al,Bl,Cl,Dl]=series(A,B,C,D,Ac,Bc,Cc,Dc);
[mlp,plp]=bode(Al,Bl,Cl,Dl,1,w);

% Check closed loop stability (model -- eigenvalues)
Acl=[A -Bu*kr; ke*C A-Bu*kr-ke*C];
Bcl=[Bw zeros(length(Bw),1); zeros(length(Bw),1) ke];
Ccl=[C -Du*kr];
Dcl=[0 0];
[mcl,pcl]=bode(Acl,Bcl,Ccl,Dcl,1,w);
cleig=max(real(eig(Acl)));
disp(['Maximum real part of closed loop e-vals = ',num2str(cleig)]);

% Check closed loop stability (data -- nichols plot)
[re,im]=nyquist(Acomp,Bcomp,Ccomp,Dcomp,1,w); i=sqrt(-1); K=re+i*im;
Loop=K.*Datayu;
mL=abs(Loop); pL=uang(Loop)+360;
figure(2)
subplot(111),  semilogy(pL,mL,plp,mlp,'--',-180*[-1  1  3  5],ones(1,4),'x',[pL(30)
pL(232)],[mL(30) mL(232)],'o')
grid
axis([-1500 1000 1e-3 100])
title('Nichols Plot -- data (solid), model (dash)')

figure(3)
subplot(211), loglog(f,mlp,'--',f,abs(Loop)), Mlabel, grid, axis([10 2000 1e-2 10])
title('Loop Transfer Function -- using ol data (solid), model (dash)')
subplot(212), semilogx(f,plp,'--',f,uang(Loop)), Plabel, grid, axis([10 2000 -500 500])

% Check closed loop performance (z/w)
CLoop=Datazw./(1+Loop);
figure(4)
subplot(211), loglog(f,abs(CLoop),f,abs(Datazw),'--'), Mlabel, grid
axis([10 2000 1e-3 1e3])
title('CL w/ OL data (solid), OL (dash) Dist to Perf TF (full comp)')
subplot(212), semilogx(f,uang(CLoop),f,uang(Datazw),'--'), Plabel, grid
axis([10 2000 -2000 500])
```

```
figure(5)
subplot(211), loglog(f,abs(CLoop),f,mcl,'--');
axis([10 2000 1e-3 1e3])
title('CL w/OL data (solid), CL model (dash) Dist to Perf TF (full comp)')
subplot(212), semilogx(f,uang(CLoop),f,pcl,'--');
axis([10 2000 -2000 500])

fprintf('\nPerf improvement from 10Hz - 1kHz is:\n')
dperfbb=perfcal(9,801,Datazw,CLoop,w);
fprintf('\nPerf improvement near 90Hz is:\n')
dperf1=perfcal(50,80,Datazw,CLoop,w);
fprintf('\nPerf improvement near 300Hz is:\n');
dperf2=perfcal(160,220,Datazw,CLoop,w);

% Check closed loop acoustic performance
CLoopa=DataRSS./(1+Loop);
figure(6)
subplot(211), loglog(f,abs(CLoopa),f,abs(DataRSS),'--'), Mlabel, grid
axis([10 2000 1e-2 1e2])
title('CL(solid) and OL(dash) Disturbance to Microphone RSS')
subplot(212), semilogx(f,uang(CLoopa),f,uang(DataRSS),'--'), Plabel, grid
axis([10 2000 -200 200])

fprintf('\nAcoustic perf from 10Hz - 1kHz is:\n')
aperfbb=perfcal(9,801,DataRSS,CLoopa,w);
fprintf('\nAcoustic perf near 90Hz is:\n')
aperfbb=perfcal(50,80,DataRSS,CLoopa,w);
fprintf('\nAcoustic perf from 300Hz is:\n')
aperfbb=perfcal(160,220,DataRSS,CLoopa,w);

Sens=1./(1+Loop);
[Acl,Bcl,Ccl,Dcl]=cloop(Al,Bl,Cl,Dl,1,-1);
[ncl,dcl]=ss2tf(Acl,Bcl,Ccl,Dcl,1);
[nl,dl]=ss2tf(Al,Bl,Cl,Dl,1);
ns=conv(ncl,dl); ds=conv(dcl,nl);
[ms,ps]=bode(ns,ds,w);
figure(7)
subplot(211), loglog(f,abs(Sens),f,ms,'--'), Mlabel, grid
axis([10 2000 1e-1 1e3])
title('Sensitivity TF -- data(solid), model(dash)')
subplot(212), semilogx(f,uang(Sens),f,ps,'--'), Plabel, grid
axis([10 2000 -500 200])

[Acomp,Bcomp,Ccomp]=ss2mod6(Acomp,Bcomp,Ccomp);
Sc=[Acomp Bcomp; Ccomp Dcomp]; Nc=[length(Acomp) 1 1];

repeat=1;
while repeat==1,
```

```
[Scr,Ncr]=balred(2,Sc,Nc); [Acompr,Bcompr,Ccompr,Dcompr]=split(Scr,Ncr);

[mcr,pcr]=bode(Acompr,Bcompr,Ccompr,Dcompr,1,w);
figure(1)
subplot(211), loglog(f,mcr,f,mc,'--'),Mlabel, grid, axis([10 2000 1e-3 1e2])
title('Full (dash) and reduced (solid) compensator')
subplot(212), semilogx(f,pcr,f,pc,'--'), Plabel, grid, axis([10 2000 -500 500])

% Recheck closed loop stability with reduced compensator
i=sqrt(-1);
[re,im]=nyquist(Acompr,Bcompr,Ccompr,Dcompr,1,w); Kr=re+i*im;
Loopr=Kr.*Datayu;
mLr=abs(Loopr); pLr=uang(Loopr);
figure(2)
 subplot(111), semilogy(pLr,mLr,plp,mlp,'--',-180*[-1 1 3 5], ones(1,4),'x',[pLr(67)],
[mLr(67)],'o')
grid
axis([-1500 1000 1e-3 100])
title('Nichols Plot -- data(solid) model(dash) -- (reduced comp)')

figure(3)
 subplot(211), loglog(f,abs(Loopr),f,abs(Loop),'--'), Mlabel, grid, axis([10 2000 1e-2
10])
title('Loop TF -- solid (reduced comp), dash (full comp)')
 subplot(212), semilogx(f,uang(Loopr),f,uang(Loop),'--'), Plabel, grid, axis([10 2000 -
500 500])

% Recheck closed loop performance with reduced compensator
CLoopr=Datazw./(1+Loopr);
figure(4)
subplot(211), loglog(f,abs(CLoopr),f,abs(Datazw),'--',f,abs(CLoop),'-.'), Mlabel, grid
axis([10 2000 1e-3 1e3])
 title('CL red (solid), OL (dash) CL full (d-d) Disturbance to Performance TF (red
comp)')
 subplot(212), semilogx(f,uang(CLoopr),f,uang(Datazw),'--',f,uang(CLoop),'-.'), Plabel,
grid
axis([10 2000 -2000 500])

figure(5)
subplot(211), loglog(f,abs(CLoopr),f,mcl,'--');
axis([10 2000 1e-3 1e3])
title('CL w/OL data (solid), CL model (dash) Dist to Perf TF (red comp)')
subplot(212), semilogx(f,uang(CLoop),f,pcl,'--');
axis([10 2000 -2000 500])

fprintf('\nPerf improvement from 10Hz - 1kHz is (reduced comp):\n')
dperfbb=perfcal(9,801,Datazw,CLoop,w);
fprintf('\nPerf improvement near 90Hz is (reduced comp):\n')
dperf1=perfcal(50,80,Datazw,CLoop,w);
```

```
 fprintf('\nPerf improvement near 300Hz is (reduced comp):\n');
 dperf2=perfcal(160,220,Datazw,CLoop,w);

 CLoopar=DataRSS./(1+Loopr);
 figure(6)
 subplot(211), loglog(f,abs(CLoopar),f,abs(DataRSS),'--'), Mlabel, grid
 axis([10 2000 1e-2 1e2])
 title('CL(solid) and OL(dash) Disturbance to Microphone RSS')
 subplot(212), semilogx(f,uang(CLoopar),f,uang(DataRSS),'--'), Plabel, grid
 axis([10 2000 -200 200])

 fprintf('\nAcoustic perf from 10Hz - 1kHz is:\n')
 aperfbb=perfcal(9,801,DataRSS,CLoopar,w);
 fprintf('\nAcoustic perf near 90Hz is:\n')
 aperfbb=perfcal(50,80,DataRSS,CLoopar,w);
 fprintf('\nAcoustic perf from 300Hz is:\n')
 aperfbb=perfcal(160,220,DataRSS,CLoopar,w);

 Sensr=1./(1+Loopr);
 figure(7)
 subplot(211), loglog(f,abs(Sensr),f,abs(Sens),'--'), Mlabel, grid
 axis([10 2000 1e-1 1e3])
 title('Sensitivity TF -- reduced comp(solid), full comp(dash)')
 subplot(212), semilogx(f,uang(Sensr),f,uang(Sens),'--'), Plabel, grid
 axis([10 2000 -500 200])

 repeat=input('Redo compensator reduction? (1=yes, 0=no)');

end

Sc=Scr; Nc=Ncr;
sav=input('Save the compensator to transcomp.mat now (1)=yes ');
if sav==1
 save transcomp Sc Nc
end
```

Appendix B

Narrowband Impedance Match

The acoustic impedance matching method controls a structural actuator to match the impedance of the acoustic cavity, thereby absorbing all of the impinging acoustic energy. The narrowband impedance match attempts to do this only at a specific frequency, while maintaining closed loop stability and avoiding amplification elsewhere. Therefore, this method would be extremely useful when the incoming disturbance is tonal in nature.

Assuming a single degree of freedom structure with a uniform pressure across the area, the coupled equation of motion is given by

$$(ms^2 + cs + k)u = f - AP \tag{B.1}$$

where m, c, and k are the structural mass, damping, and stiffness, respectively, u is the position of the structure, f is the actuator force, A is the area, and P is the pressure at the surface of the actuator. The impedance matching result derived by Glaese gives the required force as

$$f = \frac{ms^2 + (c - \rho_0 c_0 A)s + k}{-2\rho_0 c_0 As}(P - \rho_0 c_0 su) \tag{B.2}$$

where ρ_0 is the ambient density of air and c_0 is the speed of sound in air. Substituting equation B.2 into B.1 and solving for u gives

$$u = \frac{-1}{\rho_0 c_0 s} P \tag{B.3}$$

so that

$$\frac{du}{dt} = \frac{-1}{\rho_0 c_0} P \tag{B.4}$$

Thus, the narrowband impedance matching compensator must actuate the structure to force the structural velocity to satisfy equation B.4. This requirement can be rewritten as

$$\frac{\dot{u}}{P} = \frac{-1}{\rho_0 c_0} \tag{B.5}$$

Therefore, a method to derive such a compensator using the available measurements must be developed. An accelerometer is placed on the speaker cone and the open loop transfer function, $\frac{\ddot{u}}{f}$, is taken from the control speaker to the collocated accelerometer. The feedback sensor is a collocated microphone, so the transfer function for the compensator can be written as $\frac{f}{P}$. Notice that the product of the two transfer functions gives $\frac{\ddot{u}}{P}$ and an integration of this provides $\frac{\dot{u}}{P}$. Therefore the compensator must satisfy

$$\frac{\dot{u}}{P} = \frac{1}{s}\frac{\ddot{u}}{f}\frac{f}{P} = \frac{-1}{\rho_0 c_0} \tag{B.6}$$

at the specific frequency of interest. However, since the transfer function magnitudes are in Volts/Volt, conversion factors must be included. Let a_0 be the accelerometer constant with units of $\frac{V}{m/s^2}$, and m_0 be the microphone constant with units of $\frac{V}{N/m^2}$. Then the magnitude and phase of the narrowband impedance matching compensator at the frequency of interest is given by

$$X_{comp} = \frac{-1}{\rho_0 c_0}\frac{a_0}{m_0}\frac{s}{X_{acc}} \tag{B.7}$$

where X_{acc} and X_{comp} are the transfer functions of the accelerometer and compensator, respectively.

To maintain closed loop stability, the compensator was designed to have a roll up at low frequencies and a roll off at high frequencies, with the highest gain near the frequency of interest. The idea behind this design is that the loop will have high gain where attenuation is desired and quickly roll off in either direction leading to gain stability. Differentiators were placed at DC causing the roll up, and complex poles were placed near the frequency in which attenuation was desired leading to a roll off at high frequency. The parameters such as the frequency and damping of the poles, and the gain were manually tuned until an impedance match was achieved. First, the damping ratio of the compensator poles is chosen. Lightly damped poles are generally advantageous since it allows the loop to have high gain for a very small frequency range reducing the chances for instability. However, lightly damped poles have a very rapid drop in phase leading to a lack of robustness in the design. Once the damping has been chosen, the frequency of the poles is adjusted to match the phase to the impedance matching solution. The gain is then varied to match the amplitude, completing the impedance match.

The experimental setup consisted of a five foot long, one-dimensional acoustic waveguide with a circular cross section. One dual voice subwoofer speaker was mounted at each end of the waveguide. The bottom speaker was used as the disturbance speaker and the top speaker was used as the control speaker. A microphone and an accelerometer were mounted on the control speaker.

A compensator with a first order roll up and a second order pole at 375.2 Hz with a damping ratio of 0.03 was designed to achieve an impedance match at the acoustic mode at 387.5 Hz. Figure B.1 shows the compensator transfer function and the $\frac{\dot{u}}{P}$ transfer function, showing the impedance match at 387.5 Hz marked by an 'x'. Also shown is the Nichols plot based on wrapping the compensator around the open loop control speaker to microphone data as well as the predicted closed loop transfer function from the distur-

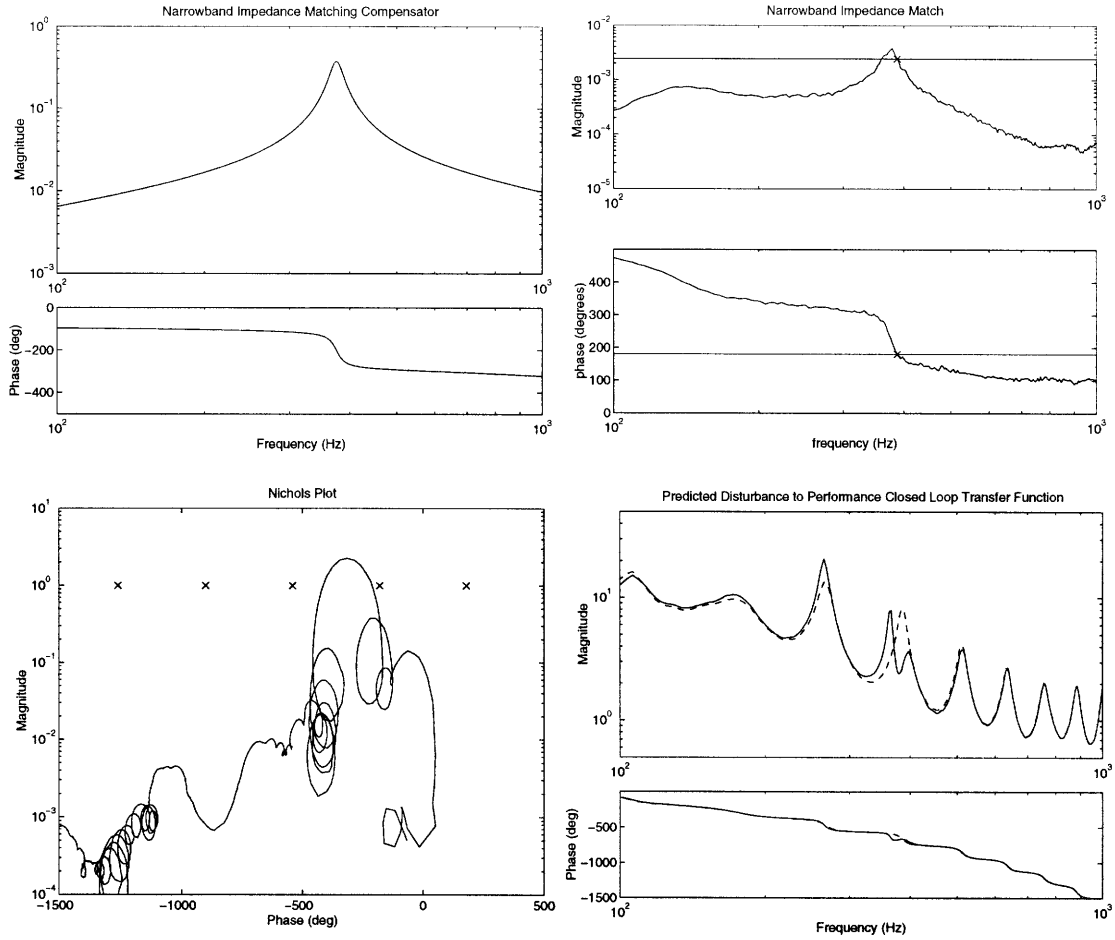

Figure B.1: Narrowband impedance matching compensator transfer function, $\dot{u}/f$ transfer function showing the impedance match, Nichols plot using open loop data, and predicted closed loop transfer function

bance speaker to the feedback microphone. Note that there is significant attenuation at the frequency of the impedance match with only minor amplification at other frequencies. The performance improvement at 387.5 Hz is 9.9 dB.

The narrowband acoustic impedance matching method was presented with simulated closed loop results. Significant reduction in the acoustic reflection was achieved at a specific frequency while maintaining overall closed loop stability and minor amplification at other frequencies. However, this approach does not allow for broadband control and is therefore only useful if the disturbance has a strong tonal component.

Appendix C

Discrete Area Averaging Acoustic Sensor

C.1 Introduction

The behavior of an acoustic field can be measured with a pressure sensor such as a microphone. Microphones use a diaphragm which deflects in response to changes in pressure, and these deflections are converted into a voltage which can be sensed and recorded. Many electret condenser microphones are small enough that they can be suspended in the acoustic field without significantly altering the acoustics. Also, these microphones are small enough to be considered omni-directional, meaning they sense pressure equally well in all directions.

In the development of the one-dimensional acoustic impedance matching controller, a sensor with high observability of only the one-dimensional acoustic modes of the waveguide is desired. The problem with a point sensor such as a single microphone is that it measures total pressure at a point, which has contributions from one-dimensional acoustic modes as well as three-dimensional acoustic modes. The advantage provided by an area averaging sensor is that incoming waves travelling perpendicular to the face of the sensor will provide signals across the area of the sensor that are in phase, since one wavefront will arrive at all points on the sensor simultaneously. On the other hand, incoming

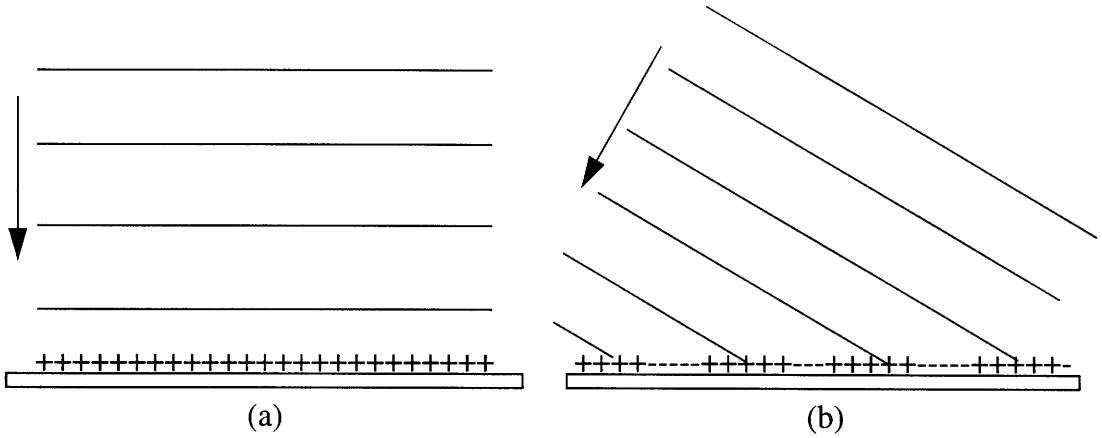

Figure C.1: Resulting signals on an area averaging sensor due to incoming waves travelling perpendicular (a) and obliquely (b) to the face of the sensor

waves impinging obliquely onto the sensor will provide signals across the area of the sensor which are not in phase with each other. This is shown in Figure C.1. The lines indicate the wavefronts where the amplitudes are constant, and the arrows indicate the direction of wave propagation. The figure on the left shows incoming waves travelling perpendicular to the face of the sensor resulting in a signal across the sensor which is in phase since the entire wavefront impinges upon it simultaneously. The figure on the right shows incoming waves travelling obliquely to the face of the sensor resulting in a sinusoidal pattern in the resulting signal across the face of the sensor. Therefore, if the area averaging was done in a continuous manner across the face of the sensor, a zero net signal would result from waves which hit the sensor obliquely since all of the positive contributions provided by the areas in which a wavefront is impinging would be canceled out by the negative contributions provided by the areas in which a trough is impinging. However, a continuous sensor is not possible, so a discrete microphone array was developed to be used as an area averaging acoustic sensor.

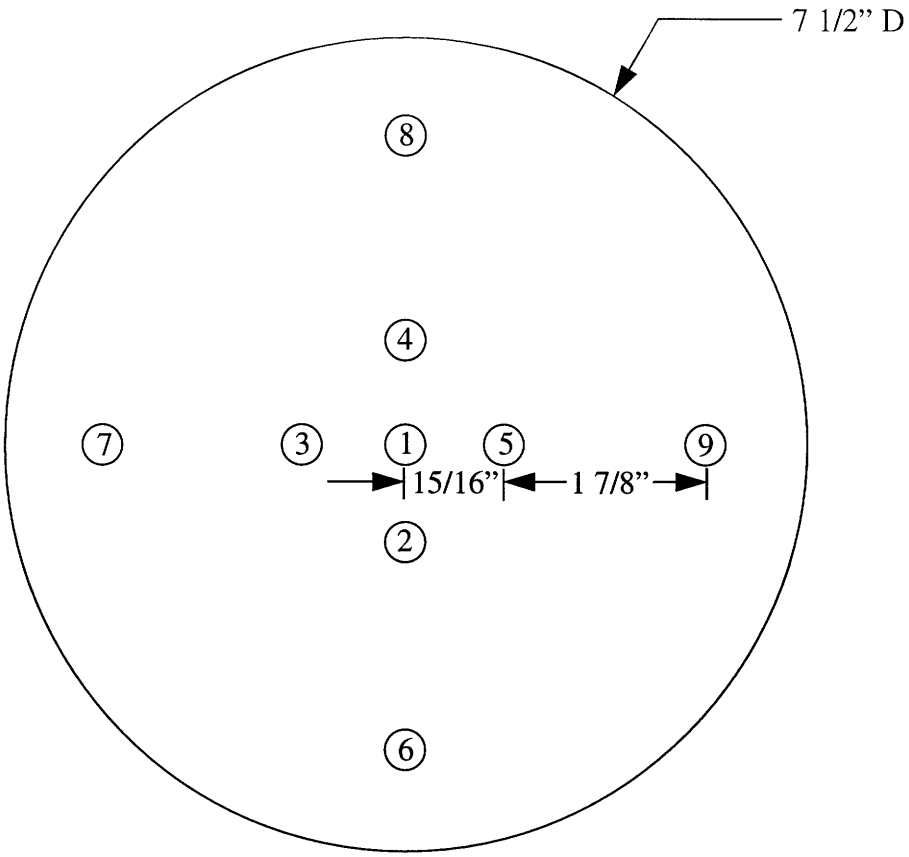

Figure C.2: Layout of discrete microphone array

C.2 Sensor Design and Signal Analysis

The feedback sensor in the acoustic impedance matching control needs to be collocated with the actuator. Therefore, the area averaging acoustic sensor needs to be placed as close to the control speaker cone as possible. An aluminum plate with 0.032 inch thickness was cut into a circle with a 7.5 inch diameter, so that it fits flush with the speaker cone. A set of nine electret condenser microphones were bonded to this plate using epoxy in the configuration shown in figure C.1. The signals from these microphones can be measured individually or in any combination. The plate was then attached to the speaker cone using silicone RTV.

One problem with the electret condenser microphones is that the diaphragm is sensitive to acceleration, so that it measures a combination of the acoustic pressure and the structural motion of the plate. Therefore, a method in which the acoustic signal can be separated from the acceleration signal needs to be derived.

The transfer function from the speaker to the microphone taken at atmospheric conditions can be expressed as

$$\left.\frac{mic}{spkr}\right|_{1atm} = G\left.\frac{\ddot{x}}{spkr}\right|_{1atm} + K\frac{acoustic}{spkr} \tag{C.1}$$

where G and K are some gains of the microphone, $\frac{\ddot{x}}{spkr}$ is the transfer function from the speaker to the structural acceleration of the plate in 1 atm and $\frac{acoustic}{spkr}$ is the transfer function from the speaker to the acoustic pressure at the location of the sensor. Also, the transfer function from the speaker to the accelerometer can be expressed as

$$\left.\frac{accel}{spkr}\right|_{1atm} = A\left.\frac{\ddot{x}}{spkr}\right|_{1atm} \tag{C.2}$$

where A is some gain of the accelerometer.

If the same transfer functions are taken in a vacuum, the acoustics will no longer be present in the microphone transfer function, leaving the signal due to the structural acceleration only. The transfer functions from the speaker to the microphone and the accelerometer in 0 atm are given by

$$\left.\frac{mic}{spkr}\right|_{0atm} = G\left.\frac{\ddot{x}}{spkr}\right|_{0atm} \tag{C.3}$$

$$\left.\frac{accel}{spkr}\right|_{0atm} = A\left.\frac{\ddot{x}}{spkr}\right|_{0atm}. \tag{C.4}$$

Then, the transfer function from the speaker to the acoustic signal at the sensor location can be derived as

$$\frac{acoustic}{spkr} = \frac{1}{K}\left(\frac{mic}{spkr}\bigg|_{1atm} - \frac{G}{A}\frac{accel}{spkr}\bigg|_{1atm}\right) \tag{C.5}$$

where

$$\frac{G}{A} = \frac{\left.\frac{mic}{spkr}\right|_{0atm}}{\left.\frac{accel}{spkr}\right|_{0atm}}. \tag{C.6}$$

This relation can be used to combine the microphone and accelerometer signals to obtain the measurement of the acoustic pressure. One point to note is that the accelerometer is a point sensor located at the center of the plate. The assumption made here is that the acceleration of the plate is dominated by the rigid body motion of the entire plate resulting from the actuation of the speaker cone. This being the case, the acceleration at the center of the plate is a good representation of the acceleration at all microphone locations.

C.3 Experimental Results

The experimental setup consisted of a 22.5 inch long one-dimensional waveguide with a circular cross section. The wave guide was capped on both ends by a steel plate, and the speaker with discrete area averaging sensor was mounted at one end of the waveguide. A vacuum pump was attached to a port on the top plate to allow for the evacuation of the chamber.

A band limited white noise signal was used to excite the speaker and measurements from the microphones and accelerometer were taken using a Tektronix Fourier Analyzer. Figure C.3 shows the transfer function from the speaker to the acoustic signal calculated at

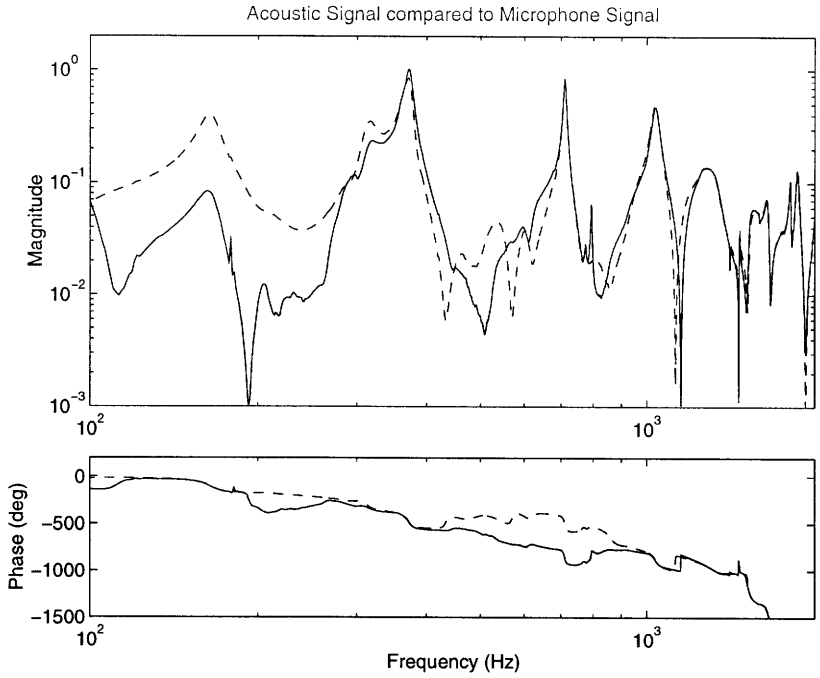

Figure C.3: Derived acoustic signal at microphone 1 (—) compared to the signal of microphone 1 (--)

microphone 1 compared to the signal of microphone 1. Notice that the transfer function of the acoustic signal is missing some of the dynamics which are present in the microphone signal, while maintaining the same observability of other modes. These high observability modes are the acoustic cavity modes of which the first three are at 359 Hz, 719 Hz, and 1078 Hz. Also note, however, that the acoustic signal transfer function does not eliminate all of the remaining dynamics. One reason for this is that the derivation of the acoustic signal only attempted to eliminate the contributions from structural acceleration. Therefore, three dimensional acoustic modes will still be observed by the acoustic signal.

Figure C.4 shows the average acoustic signal provided by five of the microphones in the array (microphones 1,6,7,8,9) compared to the acoustic signal of microphone 1. Notice that the observabilities of the one dimensional acoustic modes are not changed by the area averaging, which is expected. Also, some of the low observability modes of the acoustic

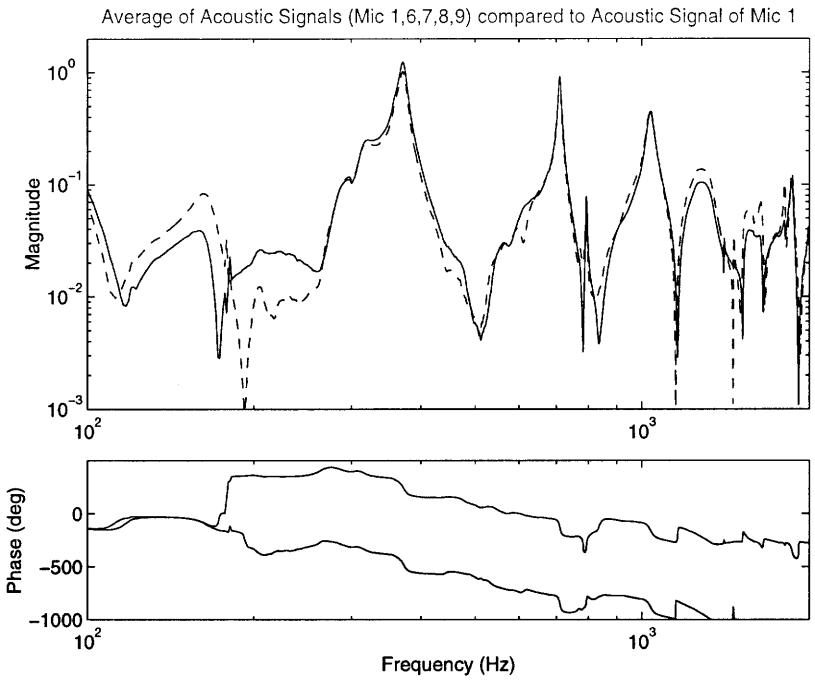

Figure C.4: Average acoustic signal of microphones 1, 6, 7, 8, 9 (—), compared to the acoustic signal of microphone 1 (--)

signal of microphone 1 have been eliminated due to the averaging. Although the sensor still retains observability of many of the unnecessary modes, keep in mind that this is only the average of five microphones. Unfortunately, the data for the average of all nine microphones was lost.

C.4 Conclusions

A discrete microphone array was developed to investigate the use of an area averaging sensor for use in the acoustic impedance matching control method. The averaging of the acoustic signals at discrete points allowed for the elimination of some three-dimensional acoustic modes while maintaining high observability of the one-dimensional acoustic modes. The performance of the discrete microphone array can be greatly increased with

the addition of more microphones to better simulate a continuous area averaging sensor. Also, an in-depth analysis of the three-dimensional acoustic modes of the chamber can lead to a more systematic approach to the placement of the microphones on the plate. The addition of weights on each of the microphones, as opposed to an unweighted average, will also lead to better results.